Understanding offshore flood basalt sequences using onshore analogues with application to permanent CO_2 storage: Examples from the Faroe Islands

Max Meakins

Master Thesis in Geoscience

Mineralogy, Petrology, and Geochemistry

60 credits

The Njord Centre

Department of Geoscience

The Faculty of Mathematics and Natural Sciences

UNIVERSITY OF OSLO

September 2021

[This page is intentionally left blank]

© Max William John Meakins, 2021

Supervisors: Bjørn Jamtveit (Njord, UIO), Sverre Planke (VBPR, UIO), John Millett (VBPR, University of Aberdeen), and Hans Jørgen Kjøll (UIO).

This thesis is published digitally via DUO: https://www.duo.uio.no/

Abstract

Reducing our CO_2 emissions is of utmost importance to mitigating climate change. Mineral trapping in reactive reservoirs is a successful means of sequestering CO_2 compared with the more conventional injection of CO_2 into sandstone reservoirs. Studies have shown the potential for intra-volcanic sites to be effective oil reservoirs, and so may also provide adequate reservoirs for the storage of CO_2. Furthermore, pilot studies such as CarbFix Iceland show complete and fast mineral trapping of CO_2 in basaltic reservoirs within 2 years. However, studies investigating specific sites for CO_2 mineral trapping are rare. This study uses the Faroe Islands as an analogue to study the feasibility of injecting CO_2 into potential offshore reactive reservoirs. A field reconnaissance to the Faroe Islands was used to gather photogrammetric data to understand the lateral and vertical extents and thicknesses of lava flows and inter-lava beds. Samples were taken from fieldwork and cores Glyvursnes-1, Grønadalsnøva-1, and Tjørnunes-2 , and were used to understand the petrological and geochemical distributions. The same samples were also used to investigate the ability for fluids to migrate away from main fluid pathways using micro-focus X-ray tomography. Finally, the solubility of lava flow tops, cores, and an inter-lava bed were used to investigate the steady-state element release rates under conditions of 25°C and pH 4. Photogrammetric data showed that simple lava flows are significantly more laterally limited than compound lava flows, allowing for increased connectivity between inter-lava beds. This study therefore found the thinning of simple lava flows to be the most significant form of communication between porous units, inter-lava beds, and intra-lava units lava flow tops and bases. The intra-lava architectures, flow tops, and cores will aid capacities, but be more prone to clogging due to channel like networks providing their permeability. The porosity of lava flow bases is increased when overlaying inter-lava beds, especially above domed sections. With the familiar presence of the inter-lava beds splitting successive lava flows, the flow bases commonly show significant porosity from vesiculation and pipe vesicle structures. CT scans showed micro-fractures spanning areas of porosity and influencing higher effective porosities. These microfractures are likely to be significant for the slow movement of fluids during the evolution of a reservoir and allowing CO_2 enriched fluids to reach reactive grains and pore spaces. Solubilities of rocks showed values comparable to areas associated with successful CO_2 mineral trapping pilot studies; however, the rates of offshore rocks are expected to be faster due to the greater abundance of low-Ti flows containing olivine. In addition, this study notes that the natural surface areas of inter-lava beds and lava flows will likely lead to the inter-lava beds being the most prosperous sources of divalent metal cations. These findings support the potential of offshore sites within the FIBG to provide reactive reservoirs for the injection of CO_2 and allow for CO_2 from the UK, Norway, and mainland Europe to be injected in a site several hundred miles closer than Iceland.

Preface

This thesis is submitted as an integral part of the two year MSc programme of Geosciences at the Department of Geosciences at the University of Oslo, Norway. This thesis was carried out under the supervision of Bjørn Jamtveit, Sverre Planke, John Millett, and Hans Jørgen Kjøll. Extra photogrammetric data was provided by GEUS.

This thesis was severely affected by the Covid-19 pandemic delaying a significant portions of this thesis. The Fieldwork component was delayed from March 2020 to June with the sampling portion of the project intended for August 2020 cancelled. Jarðfeingi, the geological survey of the Faroe Islands sampled on behalf of this thesis using sample plans. This had significant delays to when samples colud be prepared with them arriving in Early January, four months after initially planned. Another significant affect of the pandemic was the reactivity testing. Experiments were initially was scheduled to be carried out at the University of Iceland between September-December 2020; travel restrictions did not permit this, and the trip was significantly shortened and delayed until 13th May -22nd June

Acknowledgements

I would like to thank Bjørn Jamtveit, Sverre Planke, John Millett, and Hans Jørgen Kjøll on their supervision and support throughout this thesis. Thanks must be given to Martin Voigt from the University of Iceland, who has been instrumental in my understanding of the solubility experiments, and I thank him for the number of discussions that fuelled my work. In addition, I would like to thank Cassandra who has helped get through some of the more challenging moments of this thesis and provided optimism and support, particularly towards the end. I would also like to thank my friends (especially Marija) for being part of the process. This thesis has allowed me to explore an area of interest that grew from my time at the University of St Andrews, and I am grateful for the opportunity this has provided me. Finally, I would like to mention my Grandmother, Celia, who unfortunately passed away this year. I would always talk about my interest in carbon capture and we would discuss the awful trend we see with climate change. I believe she would be over the moon to know I have managed to complete the project and bring me a step closer to pursuing a climate science career.

Contents

Introduction

Climate change has become one of the greatest challenges we currently face, causing more extreme weather and vast ecological disturbances, putting ~1/3 of Earth's species at risk (Wake and Vredenburg, 2009; Snæbjörnsdóttir et al., 2017). Carbon capture and storage (CCS) has become an increasingly used technology to combat climate change, with the IPCC considering CCS to play a vital role in its mitigation (Wigley, Jones and Kelly, 2019. One of the controlling influences on Earth's climate is atmospheric CO_2, which has shown cyclical variations through Earth's history (Figure 1; Hövelmann, 2012). The control CO_2 has on Earth's climate results from it being a greenhouse gas (GHG), acting as an insulation blanket retaining heat (Hövelmann, 2012).

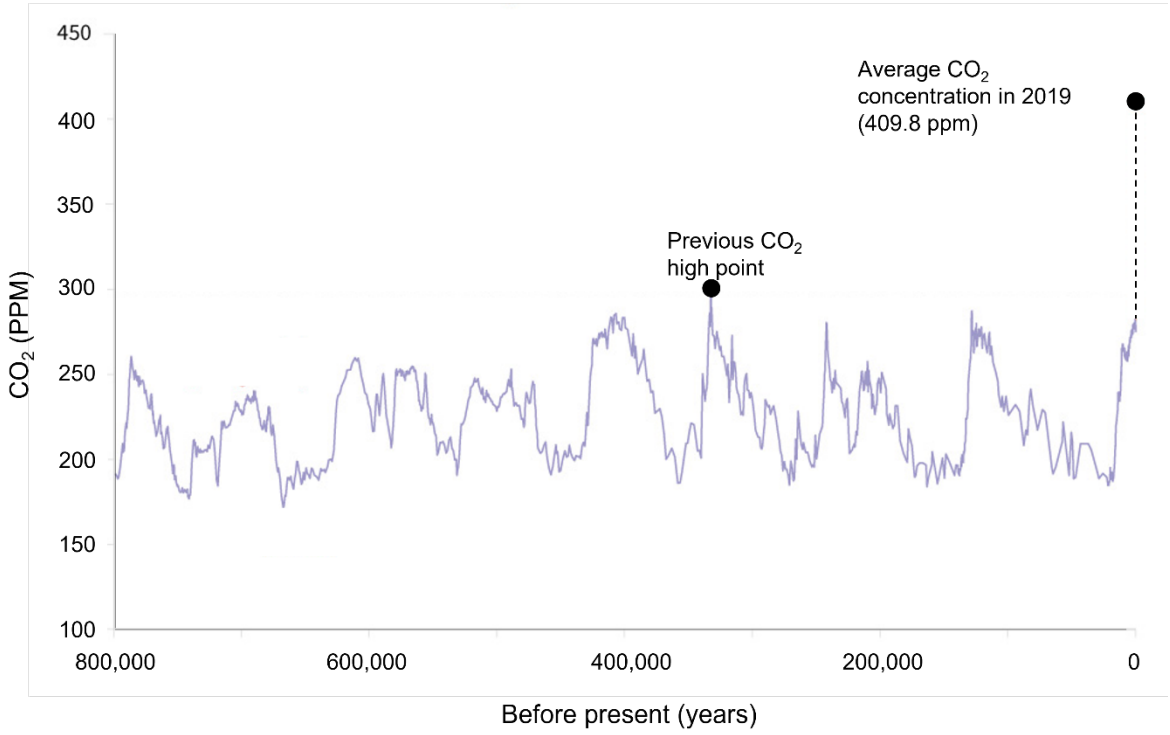

Figure 1 CO_2 reconstructions over the past 800,000 years. *The profile shows a peak and trough profile for CO_2 with current CO_2 level the highest over the shown period. Adapted from www.climate.gov*

Natural CO_2 variations through time balance outlets like volcanism and sinks such as silicate weathering (Mackenzie and Lerman, 2006; Hövelmann, 2012). When there is an unbalance between outlets and sinks, it may take thousands of years to counter the change. However, since the onset of this Industrial Era, the concentration of atmospheric CO_2 has risen by over 40%, a rise attributed to anthropogenic sources, such as the burning of fossil fuels, land-use changes, and industrial processes resulting in the most significant CO_2 concentrations over the past few hundred thousand years (Ussiri

and Lal, 2017; Williams et al. 2019). Analysis of ice cores such as Vostok Antarctic shows the recent acceleration in CO_2 concentration to be much steeper than past rises (Hövelmann, 2012; Williams, Katavouta and Goodwin, 2019). Furthermore, an observatory at Mauna Loa, Hawaii, measured CO_2 increases of 0.7 ppm yr^{-1} in the 1960s compared to 2.1 ppm yr^{-1} in the last decade, displaying a significant acceleration in atmospheric CO_2, even on the decade scale (Ussiri and Lal, 2017).

To combat the warming, a transition into renewable energy will play a significant role to decarbonize our energy mix, a key player driving CO_2 (Wigley et al., 2019). However, renewable energy is not yet numerous enough to stop our dependency on fossil fuels. With the transition slow, it is paramount to reduce global CO_2 emissions in a shorter timeframe. CCS may provide the missing link, allowing time to transition to renewable energy while still using fossil fuels (Wigley et al., 2019).

Carbon storage is the process of injecting CO_2 as a gas, liquid, or solution into a reservoir for long term removal. Historically, large scale carbon storage is implemented in sedimentary reservoirs with extensive capacities (Ussiri and Lal, 2017). Sedimentary reservoirs can be active or inactive oil fields that have the advantage of having the necessary infrastructure and geological knowledge to implement a storage site (Edwards and Celia, 2018). Active fields may also use CO_2 to pressurized the reservoir, enhancing oil recovery in a process termed Enhanced Oil Recovery (EOR), thus providing further incentive to carbon capture and storage (Dai *et al.*, 2017). Recent projects such as the Northern Lights Project, a European initiative to decarbonize European industry, is being developed South of the Troll field off the West coast of Norway to sequester 1.5 million tonnes per year. However, sedimentary storage sites require long-term monitoring due to potential leakages from the CO_2 remaining as a mobile phase for extensive time. Alternatively, achieving fast permanent storage via mineral trapping is attained from the injection of CO_2 into reactive rocks, such as basalt, where carbonate minerals form from fluid-rock interactions (Seifritz, 1990; Snæbjörnsdóttir et al., 2017). In essence, they are enhanced versions of silicate weathering reactions that are significant components in the global carbon cycle (Hövelmann, 2012).

The driving force behind the success of reactive rocks is the centration of divalent cations (Ca^{2+}, Mg^{2+}, and Fe^{2+}) within their mineralogy. Sedimentary rocks like sandstone are low in divalent cations slowing carbonate formation (Matter, 2007). This low divalent cation concentration in sedimentary rocks lead several studies (Gilfillan *et al.*, 2009; Kelemen *et al.*, 2011; Snæbjörnsdóttir *et al.*, 2017) to suggest mineral trapping in sedimentary reservoirs to occur on ≥10,000 year scale (Figure 2). These longtime scales provide little reason to explore sedimentary basins for mineral trapping, as McGrail *et al.* (2006) expressed that the long timescales could easily allow for CO_2 leakage.

Trapping mechanisms within reservoirs have differing levels of security. These trapping mechanisms with increasing security are: 1) structural and stratigraphic, 2) residual solubility, and 3) mineral trapping (Figure 2). The unreactive nature of sedimentary reservoirs limits their storage to residual trapping, a not a secure solution as mineral trapping that can be attained in reactive rocks (Figure 2).

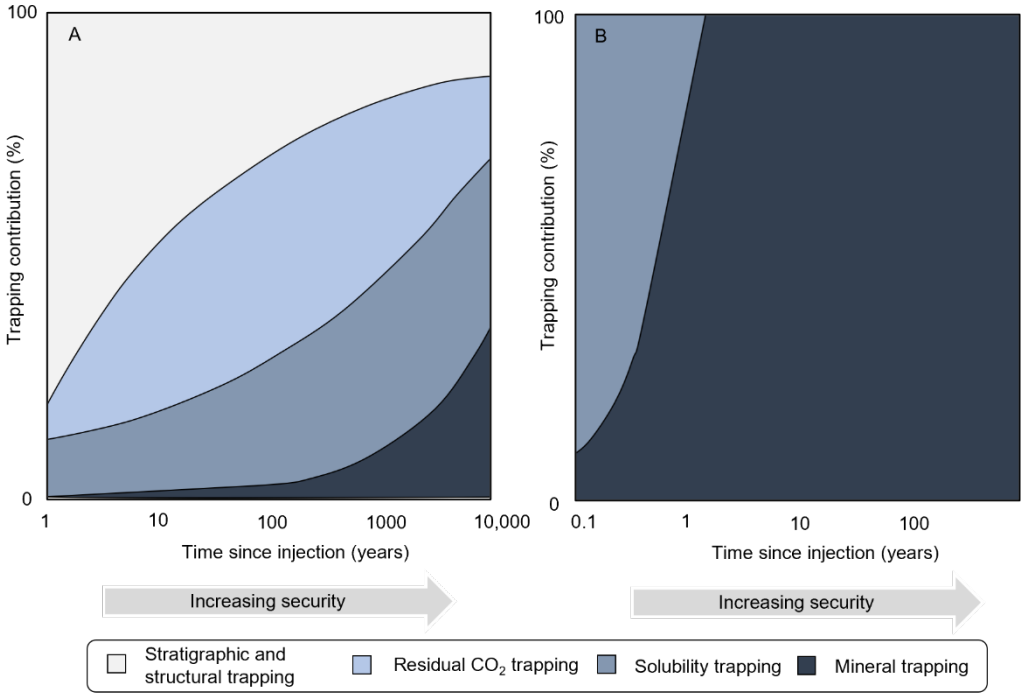

Figure 2 ***Storage differences between sandstones and reactive counterparts' (basalt).*** *A) The sedimentary type goes through several phases; firstly, the injected CO_2 gas is more buoyant than the formation fluids and rises, requiring structural and stratigraphic traps. Over time the CO_2 gas becomes distributed into the pore space of the rock, known as residual trapping, followed by the dissolution of CO_2 into formation waters producing solubility trapping. The last step, mineral trapping, is the formation of carbonates from fluid-rock interactions. B) Reactive rocks like basalt require much less time to form carbonates attributed to permanent storage, and thus mineral trapping dominates within a short time frame. Note the order of magnitude difference between the two x-axes' of A and B. Adapted from Snæbjörnsdóttir et al. (2017).*

The higher divalent cation concentrations within reactive rocks significantly reduce the time needed for carbonate formation. Gislason and Oelkers (2014) and Snæbjörnsdóttir et al. (2017) indicate the process of mineral trapping to be 95% complete within 2 years at 20-50°C (Figure 2) (Snæbjörnsdóttir et al., 2017; Pogge von Strandmann *et al.*, 2019), over three orders of magnitude faster than sedimentary counterparts, significantly cutting the probability of leakage and minimizing the need for monitoring.

Large igneous provinces are distributed over most contents. These formations represent significant accumulations of volcanic material such as lava flows, dykes and sills, and volcanogenic inter-lava beds (Bryan and Ernst, 2008). These formations therefore represent large volumes of reactive rock that could be used to store CO_2. One study by McGrail et al. (2006) stated that the Columbia River Basalt Group, could store >100 Gt of CO_2, a total that would hold over 15 years worth of current USA CO_2

emissions (Inventory of U.S. Greenhouse Gas Emissions and Sinks | US EPA, 2021). Further studies by Slagle et al. (2008) looked at conservative capacities of deep-sea basalt aquifers, calculating a minimum cumulative estimate of 8,238 Gt of CO_2, enough to store 223 years' worth of global emissions of CO_2 at 2019 levels showing the sizable potential of carbonate mineralization within basalts.

This study uses basalt sequences from the Faroe Islands Basalt Group (FIBG) of the Faroe Islands to represent onshore analogue exposures of extensive offshore reservoirs. This study aims to provide essential information on reservoir potential and rock reactivities of these offshore counterparts. A combination of detailed macro and micro scale reservoir properties are tied with laboratory experiments to explore the nature and rate of potential basaltic CO_2 storage sites'. For this aim to be studied, a series of objectives were constructed.

The objectives of this thesis:

1. Use photogrammetry to investigate the vertical, lateral, and thickness variabilities of lava flows and inter-lava beds.
2. Combine field observations with photogrammetry to define reservoir characteristics.
3. Characterize the mineralogy and chemical variability of both lava flows and inter lava beds.
4. Investigate fluid flow possibilities away from main fluid pathways.
5. Carry out solubility testing of lava flows and inter lava beds to determine the ability of the rocks to provide the necessary cations for carbonate mineralization.

1.1 Thesis complications

The global pandemic delayed a significant portion of this thesis. Fieldwork and sampling were meant to be carried out in two separate field trips. The first field trip in March and the sampling in June; however, the Covid-19 pandemic delayed both aspects, with the first field trip delayed until June and July 2020 and the sampling until August; although, due to travel restrictions, the sampling was cancelled and carried out by Jarðfeingi, the geological survey in the Faroe Islands, in December 2020 with the samples being received in January 2021, 6 months later than planned. Furthermore, reactivity testing was scheduled to be carried out at the University of Iceland between September-December 2020; travel restrictions did not permit this, and the trip was significantly shortened and delayed until 13th May -22nd June 2021. Analysis of the BET specific surface areas was also not carried out until August due to the holiday period during July, providing 3 weeks to review the new data.

1.2 Background

1.2.1 Rock types

The most common reactive rocks are ultramafic and mafic lithologies (Hansen *et al.*, 2005; Kelemen *et al.*, 2011, 2018; Gysi and Stefánsson, 2012; Hövelmann, 2012; Real and Vishal, 2016). These rock types have an abundance of minerals such as olivine, pyroxene, and plagioclase, containing the necessary divalent cations (Table 1).

Table 1 ***Table of common rock-forming minerals***

Group	Mineral name	Formula
	Quartz	$SiO2$
	Orthoclase, Microcline, Sanadine	$KAlSi_3O_6$
	Ca-Plagioclase (endmember anorthite)	$CaAl_2Si_2O_8$
	Na-Plagioclase (endmember albite)	$NaAlSi_3O_8$
Silicates	*Muscovite*	$KAl_3Si_3O_{10}(OH)_2$
	Biotite	$K(Mg,Fe)_3AlSi_3O_{10}(OH)_2$
	Kaolinite	$Al_2Si_2O_5(OH)_4$
	Pyroxene	$Ca(Mg,Fe)Si_2O_6$
	Amphibole (Hornblende)	$(Ca,Na)_{2\text{-}3}(Mg,Fe)_5Si_8O_{22}(OH)$
	Chlorite	$(Mg,Fe)_6(Al,Si)_4O_{10}(OH)_8$
	Olivine	$(Mg,Fe)_2SiO_4$
	Kyanite, Andalusite, Sillimanite	Al_2SiO_5
	Garnet	$(Ca,Mg,Fe,Mn)_3Al_2Si_3O_{12}$
	Staurolite	$Fe_2Al_9Si_4O_{22}(OH)_2$
Sulfates	*Gypsum*	$CaSO_4 \cdot 2H_2O$
	Anhydrite	$CaSO_4$
Sulfides	*Pyrite*	FeS_2
	Chalcopyrite	$CuFeS_2$
	Galena	PbS
	Sphalerite	ZnS
Carbonates	*Calcite, Aragonite*	$CaCO_3$
	Dolomite	$CaMg(CO_3)_2$
Phosphates	*Apatite*	$Ca_5(F,Cl)(PO_4)_3$

Common ultra-mafic rocks, peridotite and serpentinite, make up only 1% of Earth's crust. Although ultramafic rocks are present on most continents, they do not provide widespread potential due to their rarity (Kelemen and Matter, 2008; Hövelmann, 2012; Real and Vishal, 2016). Mafic rocks are more prevalent. Basalt, the most common form of mafic rock, covers nearly 10% of Earth's Surface (Real and Vishal, 2016), including voluminous arrays in the form of flood basalts, Large igneous provinces (LIP's) and ocean ridges. Just one oceanic ridge, Ontong Java Plateau, has an appropriate reservoir volume of 2,616,646 $Km^{3,}$ a significant quantity (Goldberg and Slagle, 2009; Tomsich *et al.*, 2015). Furthermore, magma rich rifted margins represent areas of significant interest to potential reservoirs. These flood basalt sequences form large expanses of volcanic and magmatic material, which can be several kilometres thick and spanning hundreds of kilometres (Harkin *et al.*, 2020). The

extrusive lava flows from wedge-shaped seaward dipping reflectors (SDRs) thickening along dip composed of subaerial and submarine lava flows with minor accumulations of tuffs and volcaniclastic material that can represent intra-volcanic prospects (Harkin *et al.*, 2020). However, due to most SDR's being offshore and buried under sediments, analysis is confined to seismic reflection data and onshore analogues (Harkin *et al.*, 2020).

1.3 Reservoir characteristics of flood basalt sequences

The reservoir capabilities of intra-volcanic rocks have been researched in studies such as Vosgerau *et al.* (2011, 2016), Couves (2015), and Ólavsdóttir et al. (2015). These studies are partly due to the discoveries of reservoirs within the Faro-Shetland Basin, showing the possibility for intra-volcanic reservoirs in this region, e.g. the Rosebank intra-volcanic reservoir (Vosgerau *et al.*, 2011, 2016). According to Vosgerau *et al.* (2016), these discoveries provided the necessity to search for analogues to classify reservoir styles, connectivity, and compartmentalization within intra-volcanic units.

Lava flows have also been exploited in the oil and gas industry for the reservoir quality expressed in their flow tops (Slagle et al., 2008; Ólavsdóttir, Andersen and Boldreel, 2015; Wang *et al.*, 2015). Although flow tops display limited capacity due to being confined to the flow's upper proportions, the combination of laterally extensive intra-volcanic units and lava flow tops could provide large reservoir capacities.

Four stratigraphic units of differing petrophysical properties are present in flood basalt sequences; these include flow tops, flow cores, flow bases (comprising the intra-volcanic architectures), and inter-lava beds (

Figure 3). The presence of brecciation, vesiculation, and weathered bole horizons define flow-tops and may comprise up to 40% of the flow volume with connectivity provided by coalescing vesicles and joining fracture networks (Couves, 2015). Flow cores are massive units, often with rare vesiculation and tend to show very low permeabilities, consequently acting as seals (Couves, 2015). The lowermost section of a lava flow is termed as the flow base, showing numerous brecciation and amalgamations of pipe vesicles with localized prosperity (Couves, 2015). Inter lava flow beds are accumulations of sediment of pyroclastic and epiclastic origins of variable porosities, and permeabilities determining their petrophysical properties (Mathisen and McPherson, 1991; McGrail *et al.*, 2006; Ólavsdóttir, Andersen and Boldreel, 2015). These inter lava beds may split lava flows and provide additional capacity to a reservoir.

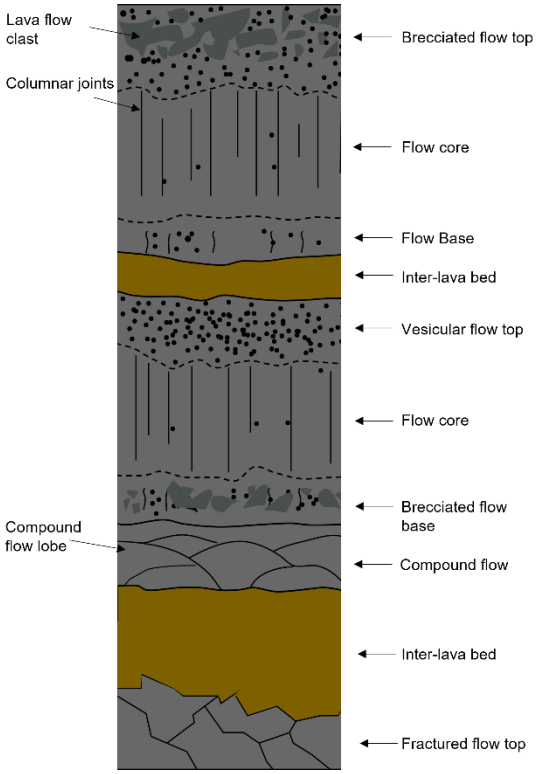

Figure 3 ***Inter and intra-volcanic reservoir properties.*** *The flow tops can be characterised as vesicular, brecciated, or fractured, showing elevated porosity, although the effective porosity may be limited, especially in vesicular types. The flow cores show limited vesiculation representing low porosities and permeabilities; however, fractures and joints may cross-cut the core. The flow bases have some accumulations of vesicles and may show pipe vesicles, they may also be brecciated. Compound lava flows are comprised of numerous overlapping lava flow lobes that show limited flow tops, cores, and bases. Inter-lava beds are comprised of sedimentary material with variable porosities and permeabilities and split successive lava flows.*

The literature (Japsen *et al.*, 2004; Couves, 2015; Ólavsdóttir, Andersen and Boldreel, 2015; Vosgerau *et al.*, 2016; Ólavsdóttir, Eidesgaard and Stoker, 2017) show flow tops to be the most effective fluid pathways; however, flow bases and even flow cores do show some potential especially at a microscale that may be useful in understanding the evolution of a reservoir. Additional reservoir capacity can be found adjacent to fault zones, artificially improved via hydraulic fracturing, and a process known as reaction-induced cracking (Morrow and Lockner, 2001; McGrail et al., 2006; Kelemen et al., 2011; Røyne et al., 2011; Kelemen and Hirth, 2012).

Connectivity of individual porous units may be essential to providing a large network of porous units comprising a sufficient reservoir. Couves (2015) states the presence of columnar jointing and fractures found within flows to cross-cut flow cores joining adjacent flow tops and inter-lava beds. Similar joining can occur when faults cross-cut lava flows and inter-lava beds, providing migration pathways for fluids that would otherwise be blocked. However, faulting may also disconnect inter-lava beds and intra-lava zones, causing compartmentalization (Passey and Bell, 2007; Vosgerau et al., 2011, 2016; Couves, 2015; Millett et al., 2017).

Reservoirs within intra-volcanic units can be found within the lava flows or inter-lava beds, although much of the research has focused on the latter (Vosgerau *et al.*, 2011, 2016; Ólavsdóttir et al., 2017). In essence, the combination of flow architectures and inter-lava beds provide reservoir capacity and seals to trap fluids. Understanding the continuity and thicknesses of these volcanic units is imperative to classifying reservoir characteristics.

1.4 Pilot studies

Several pilot studies have explored mineral trapping in basalt. These include CarbFix, Iceland and the Big Sky Carbon Sequestration in Wallula, USA. CarbFix uses the combination of CO_2 and H_2S dissolved in water, whereas the Big Sky Sequestration Project (BSSP) differs using pure supercritical CO_2. Both types of injection fluids form liquids denser than formation waters, reducing the need for structural and lithological caps. The CarbFix method is significantly more water-intensive, with only 5% of the injection fluid being CO_2, putting pressure on water resources and filling the reservoir's capacity. These may be alleviated by using seawater to reduce freshwater demand and pumping water out of the reservoir to redeem its capacity once sufficient carbonization has taken place (Gislason and Oelkers, 2014). Further to the use of seawater it has recently been proven in Voigt *et al.* (2021) that fast carbonation within basalt occurs with CO_2 charged seawater.

The use of supercritical CO_2 in the BSSP has shown promising results. The process of injecting supercritical CO_2 is fundamentally the same as CarbFix, though the supercritical CO_2 dissolves into the formation waters rather than the injected fluid, allowing for the in-situ reactions to occur. McGrail *et al.,* (2011) noted that 18% of the CO_2 injected was dissolved in formation waters within one year, slow compared to the dissolution of CO_2 being five minutes in the CarbFix project and indicating the injected phase is essential to the carbonatization process.

1.5 Carbonatization reactions

Carbonate formation in natural and engineered carbonization is a thermodynamically favourable process in reactions involving silicate minerals (Hövelmann, 2012). The carbonatization process involves a series of simple reactions. The resulting carbonization derives from the dissolution of CO_2 with water producing carbonic acid:

$$CO_{2(g)} + H_2O_{(l)} = H_2CO_{3(aq)} \quad (1)$$

Carbonic acid subsequently becomes dissociated, releasing protons that lower the pH of the solution. The resulting pH being reliant on the partial pressure of CO_2.

$$H_2CO_{3(aq)} = HCO_3^-{}_{(aq)} + H^+{}_{(aq)} \quad (2)$$

The injection of the CO_2 enriched fluid into a basaltic reservoir causes the dissolution of silicate minerals and basaltic glass releasing divalent cations at the water-rock interface. The consumption of protons during the reaction in conjunction with groundwater mixing causes the pH to rise (3-5).

Anorthite: $CaAl_2Si_2O_{8(An)} + 8H^+ = Ca^{2+} + 2Al^{2+} + 2H_4SiO_{4(aq)}$ *(3)*

Olivine: $(Mg,Fe)_2SiO_{4(Ol)} + 4H^+ = 2(Fe^{2+}, Mg^{2+})_{(aq)} + H_4SiO_{4(aq)}$ *(4)*

Pyroxene: $CaMgSi_2O_6 + 4H^+ = Ca^{2+}_{(aq)} + Mg^{2+}_{(aq)} + 2SiO_{2(aq)} + 2H2O_{(l)}$ (5)

Free divalent cations released during the dissolution reactions react with free carbonate (CO_3^{2-}) in the formation fluids and precipitate carbonate minerals once the pH rises to an appropriate level. Basalts typically contain considerable quantities of plagioclase, pyroxene, +/- olivine, +/- non-crystalline glass (Hövelmann, 2012). Consequently, basalts contain approximately 5-6 wt% Mg, and 7-10 wt% Ca and Fe (Hövelmann, 2012). The type of carbonate precipitated is dependent on the available divalent cation and subsequently depends on the mineralogy of the reservoir rock (Kelemen and Hirth, 2012).

$(Ca, Mg, Fe)_{(aq)}^{2+} + CO_{3(aq)} = (Ca, Mg)CO_{3(s)}$ (6)

Moreover, the process is not limited to carbonate formation with accessory minerals such as clay and serpentinite occurring during seritization and hydration (Gudbrandsson, 2014).

$2Mg2SiO_{4(s)} + 3H_2O_{(l)} = Mg_3Si_2O_5(OH)_{4(s)} + Mg(OH)_{2(s)}$ (7)

Matter et al. (2007) noted that carbonate precipitation is fast, and thus, the rate-limiting factor represents the dissolution rates of the silicate minerals (3-6). Each silicate mineral has an individual dissolution rate compared to another, the fastest being Mg-Olivine (forsterite), likely dominating the dissolution within a crystallin rock containing this mineral, especially with the dissolution rate being approximately one order of magnitude faster than labradorite (Ca-Na plagioclase) and diopside (Figure 4). Consequently, forsterite expresses one of the fastest reaction rates for carbonatization and hydration, connecting a particular rock's reactivity with its mineralogy (Barnes and O'Niel, 1969; Seifritz, 1990; Kelemen and Manning, 2015; Fanning *et al.*, 2017; Kelemen *et al.*, 2018). Ca-rich phases of plagioclase generally show faster dissolution rates than Na-rich counterparts, and common basalt secondary minerals, zeolites (stilbite and heulandite), show slow dissolution rates than the common primary minerals (Figure 4). The dissolution rates are generally determined by a silicate mineral or glass's ability to break the Si-O bond (Matter, Takahashi and Goldberg, 2007; Gudbrandsson, 2014). However, dissolution rates are also the function of pH, and thus, there is a positive correlation between pCO_2 and the rate constant; thus the composition of the injected fluid is vital in enhancing the process of mineral trapping the CO_2 (Appelo and Postma, 1993). Each mineral has a particular dissolution rate under specific conditions, and thus the mineralogy of the rock samples plays a vital part in their dissolution rate. As a result, minor differences within the mineralogy of the samples

causes changes to both the dissolution rate and the elemental composition, supported by Gudbrandsson *et al.* (2011).

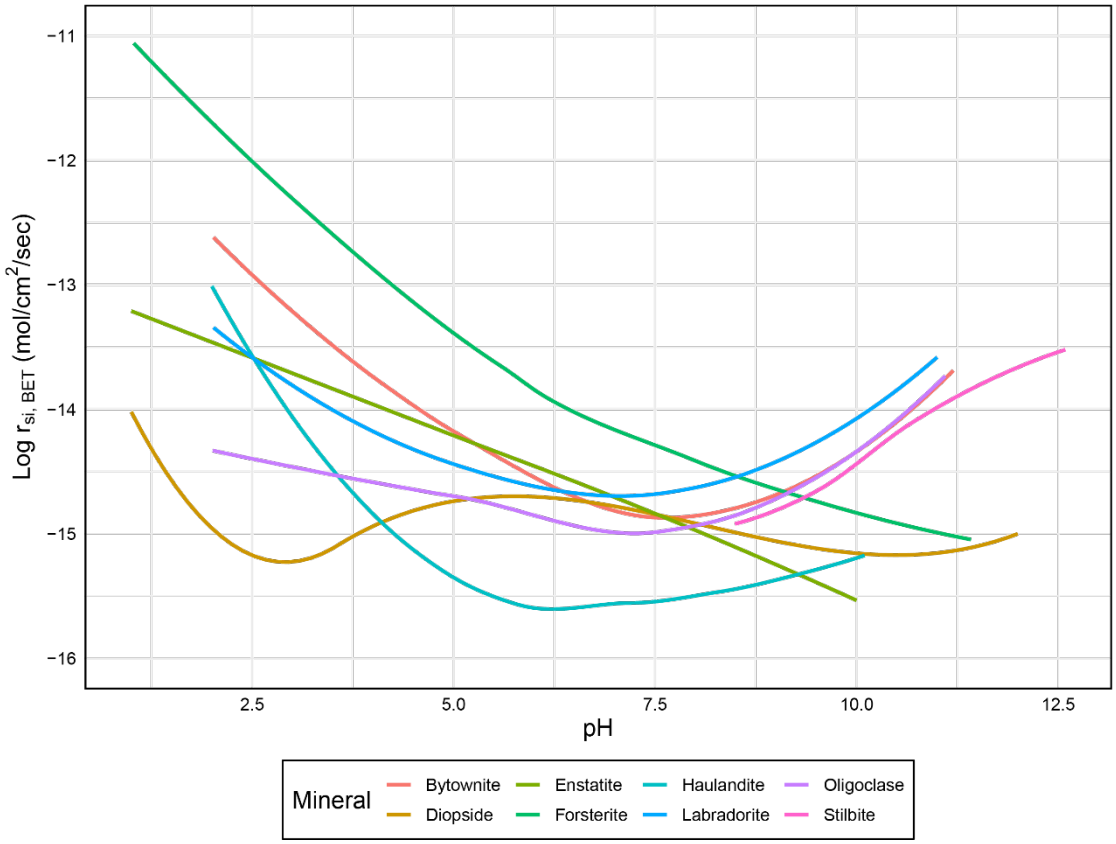

Figure 4 ***Si release rates for common minerals within the Faroe Islands with that of the dissolution samples as a function of pH. Mineral*** *dissolution rates were acquired from* (Ragnars, 1993; Chen and Brantley, 1998; Oelkers and Schott, 2000; Pokrovsky and Schott, 2000; Gudbrandsson *et al.*, 2014).

Studies have researched the success of co-injecting CO_2 and other compounds to enhance the carbonatization process. Randolph and Saar (2011) noted that adding H_2S, like the CarbFix method, does not reduce the pH enough for a notable effect due to buffering. However, Xiao et al. (2009) showed that SO_2 lowered the pH at the injection site to near-zero, aiding mineral dissolution. Although, Xiao et al. (2009) added that the low pH could cause the corrosion of pipes and caps as well as causing clogging of pore space with minerals anhydrite and albite. The findings by Xiao et al. (2009) and Randolph and Saar (2011) further stresses the importance of the injective fluid composition.

Conditions such as temperature may also be used to improve reaction rates. Kelemen and Hirth (2012) state that olivine hydration and carbonatization increase with temperature, though the chemical potential at a given fluid pressure decreases, providing maximum reaction rates in the region of ~260°C for serpentinization and ~185°C for carbonization. Combining ideal temperatures and sufficient permeability creates the possibility of positive feedback cycles from reaction induced

fracturing that contribute to new reactive surfaces and illustrate the importance of the reactions' conditions.

1.6 Reaction induced fracturing

During the carbonatization process, there tends to be a substantial volume increase causing the reactions to become self-limiting, producing blockages, reducing porosity, permeability, and the plating of reactive surfaces (Rudge et al., 2010). Nevertheless, an adversary process known as reaction driven cracking has been observed by several studies (Kelemen *et al.*, 2011; Røyne *et al.*, 2011; Kelemen and Hirth, 2012; Plümper *et al.*, 2012; Lacinska *et al.*, 2017). The fracturing stems from the positive volume change during the growth of secondary crystals in place of primary minerals (Kelemen and Hirth, 2012) and is conjectured to lead to self-maintaining processes. This volume change inflicts a confining pressure, causing an accumulation of local differential stress, fracturing the surrounding groundmass, resulting in connectivity between reactive grains (Figure 5 (Jamtveit, Malthe-Sørenssen and Kostenko, 2007; Kelemen and Hirth, 2012). Kelemen and Hirth (2012) calculated that serpentinization of olivine creates up to 300 MPa of stress, with carbonization at low temperatures, forming crystallization pressures over 1 GPa, enough to overcome the frictional stress associated at any depth serpentine and Mg-carbonate are stable. However, Kelemen and Hirth (2012) did note limitations to the process in the form of frictional sliding along preexisting fractures and increases in rock volume.

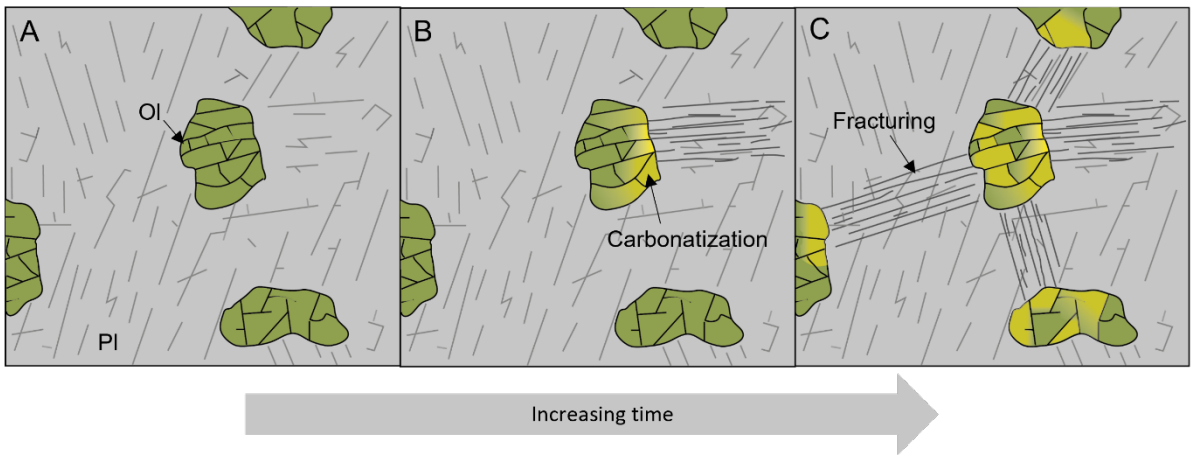

Figure 5 ***Schematic showing the process of reaction driven cracking.*** *A) Olivine (Ol) phenocrysts surrounded by a microcrystalline plagioclase (Pl) groundmass. B) A series of thin microfractures reach the middle olivine crystal carrying with them fluids that begin to react with the olivine crystal to form a carbonate, C) over time, the olivine phenocryst swells as it is replaced by carbonate, increasing the confining pressure. As the phenocryst is not perfectly round, differential stress builds until fractures propagate perpendicular to the crystal boundary, reaching more olivine phenocrysts and the process repeats.*

The cracking process is often studied in rocks high in olivine, a mineral noted for its fast reactivity with CO_2 and subsequent large volume change of 44%. Martin and Fyfe (1970) and O'Connor et al. (2004) noted rates associated with carbonization reduced by ~3× at 26-93% of olivine carbonation from the plating of reactive surfaces. However, rocks representing complete replacement, such as listvenite and serpentinite, provide evidence for complete replacement in natural settings (Kelemen and Hirth, 2012). Nevertheless, it is relatively unknown how this process manifests in olivine poor rocks, and thus the application to carbon storage may depend on specific mineral volume changes and enhanced reaction rates.

Geological setting

This study focuses on the Faroe Islands, an archipelago of 18 mountainous islands with long narrow, steep-sided fjords stretching in an NW-SE direction (Passey and Bell, 2007). The Faroe Islands are situated within the North Atlantic Ocean and located ~320 km from the UK and ~430 km from Iceland (Figure 6). Wave action significantly affects the Faroe Islands, with strong North Atlantic currents undercutting the coastlines, particularly on the Islands western extent. This undercutting has formed extensive steep sea cliffs compared to the relatively poorly exposed Easterly extent with grass-covered cliffs.

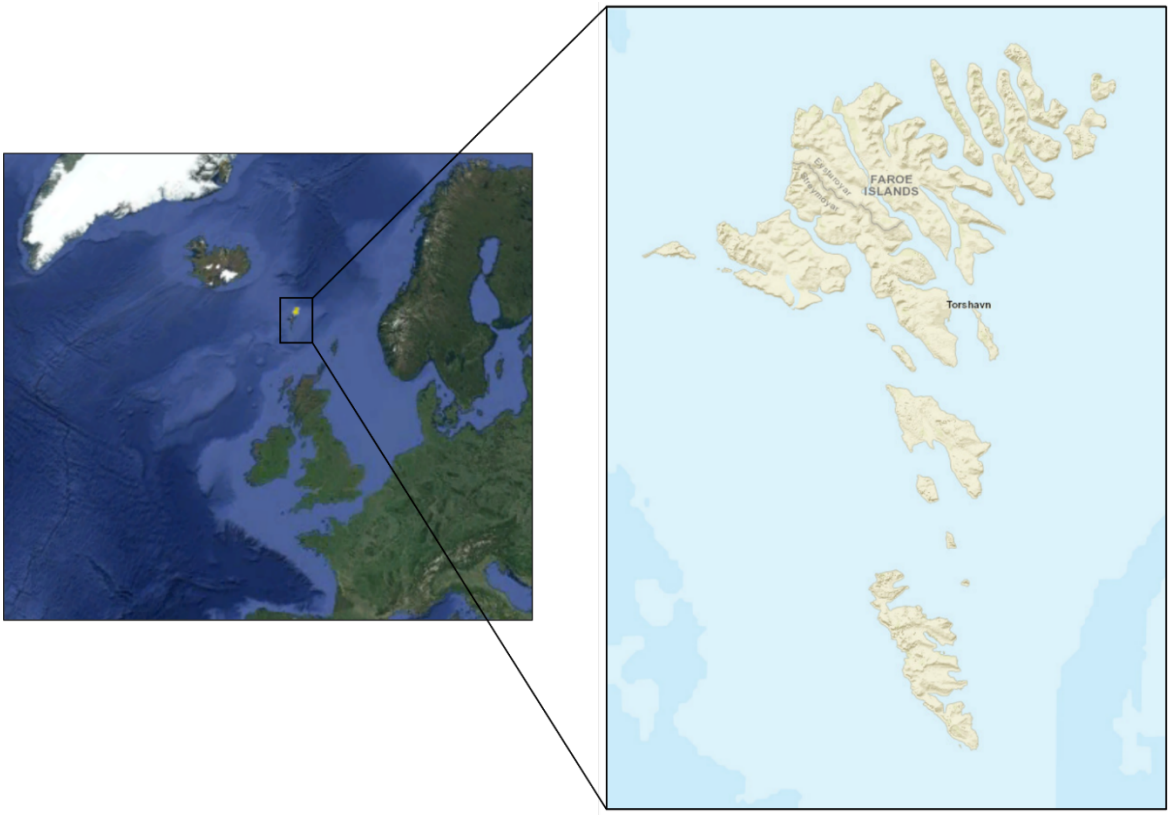

Figure 6 ***Location and map of the Faroe Islands****. The Faroe Islands comprise of 18 islands within the North Atlantic Ocean located ~430 km from Iceland and the ~320 km of mainland UK. Maps are taken from Google Earth, earth.google.com/web/ and ggmap package v3.0.0.*

The islands comprise basalt sequences with subsidiary volcaniclastic beds representing the only surface exposures of the Faroe Islands Basalt Group (FIBG), part of the more extensive North Atlantic Igneous Province (NAIP; Passey and Jolley, 2008; Millett *et al.*, 2017). The FIBG is located towards the western extent of the NW European passive continental margin, forming an area of 120,000 km^2 (Passey and Bell, 2007).

The FIBG formed from volcanic activity in the Palaeocene and Eocene between 62 and 54 Ma from rifting between the North American and Eurasian plates, which formed the North Atlantic Ocean (Passey and Bell, 2007). The rifting onset was initiated by the proto-Iceland plume situated to the West of the Faroe Islands below Greenland, forming extensive volcanism and yielding a series of lava flows of compound (irregular bundle of flows overlapping one another, indicative of multiple source volcanism), simple (massive structures with defined flow tops, cores, and bases), and hyaloclastite forms. However, times of less intensive volcanic activity allowed for the deposition of sedimentary units of mostly volcaniclastic origin by fluvial and mass flow events (Passey and Bell, 2007; Ólavsdóttir, Andersen and Boldreel, 2015).

Towards the end of volcanic activity, faulting and fracturing increased and late-stage magmatic activity propagated through the stratigraphy to form basaltic dykes (Jørgen *et al.*, 2019). Final magmatic emplacement formed sills in the stratigraphy resulting from doming and reverse faulting following a compressional event (Hansen et al., 2011). Figure 7 shows a broad overview of the FIBG.

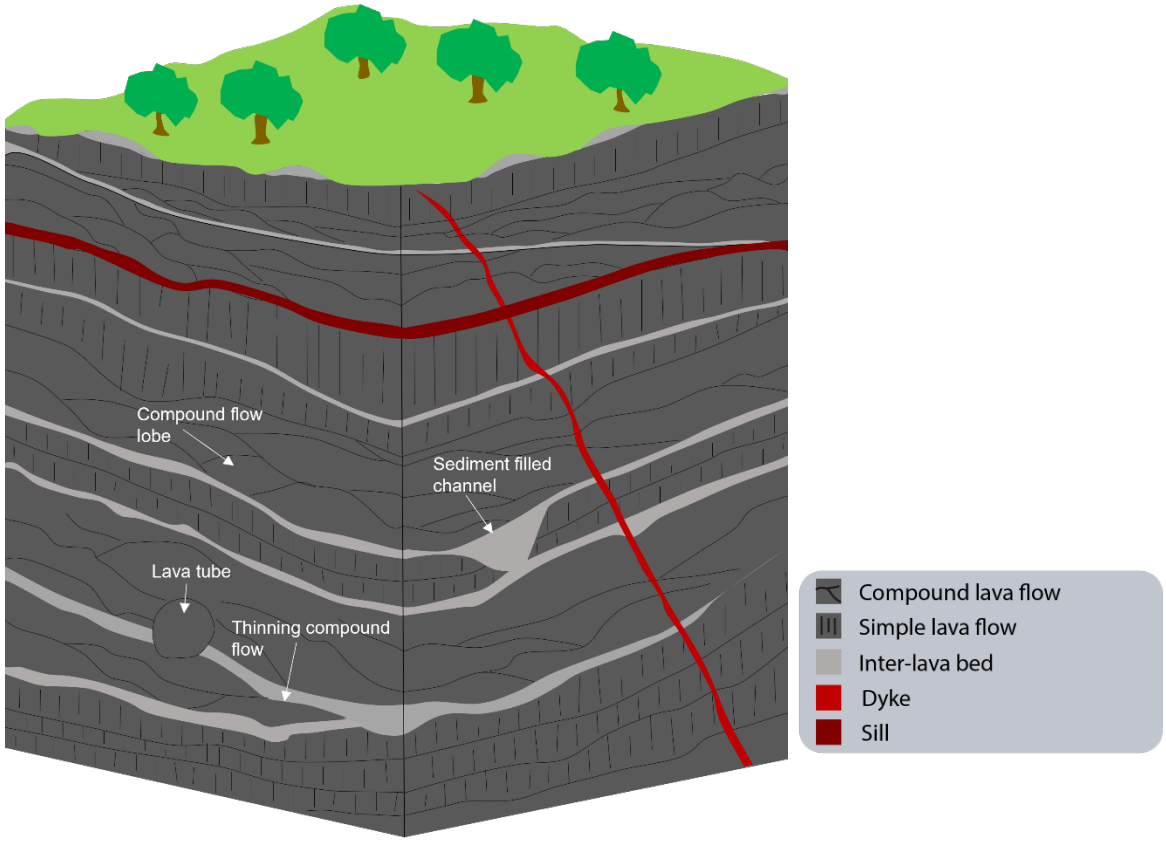

Figure 7 ***Schematic of a generalized volcanic sequence of the FIBG.*** *It is observed to show both compound and simple flow types, with the latter being composed of a single flow lobe. Compound flows can be seen to be composed of an irregular bundle of flows overlapping one another, whereas simple types display more massive structures with defined flow tops, cores, and bases. Above some of the lava units, volcaniclastic beds lie on top of the topography of the underlying flow unit. Lava tubes that fed volcanism can be seen crosscutting the flows and inter-lava beds compartmentalising them. Later stage volcanisms can be seen in the form of dykes and sills crosscutting the stratigraphy and forming areas of further compartmentalization.*

2.1 Onshore stratigraphy of the FIBG

2.1.1 Introduction

The onshore stratigraphy of the FIBG consists of seven lithologically distinct formations of volcanic and sedimentary origin (Figure 8). The formations are classified as the Beinisvørð, Prestfjell, Havannghi, Malinstindur, Sneis, and Enni formations (Passey and Jolley, 2009; Petersen, 2014; Millett *et al.*, 2017). Together these formations are ~ 7 km thick, with ~ 3 km exposed on the Faroe Islands (Petersen, 2014), most of which are the Malinstindur and Enni formations (>2.5 km). This chapter provides an overview of this stratigraphy and provides the reader with an understanding of the associated geology.

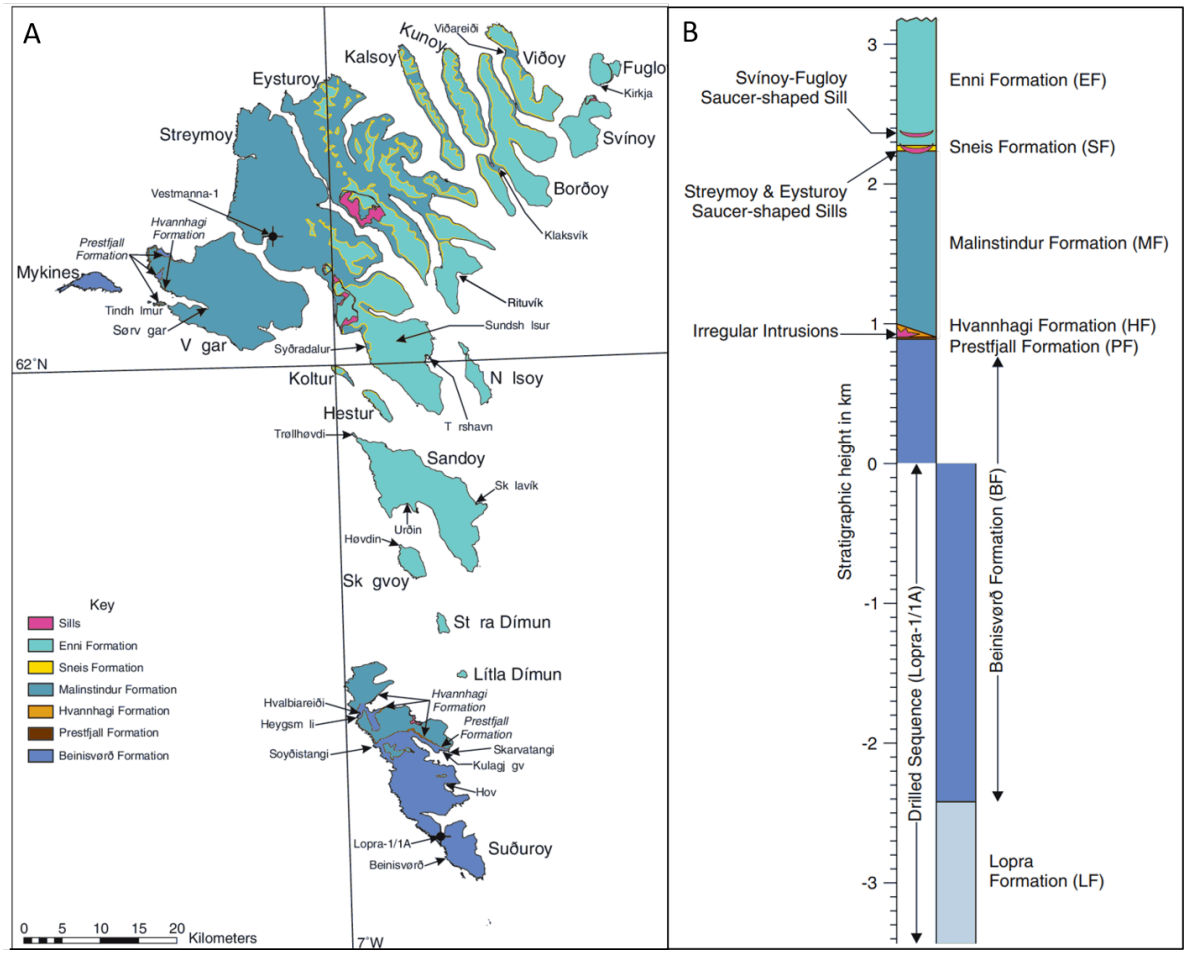

Figure 8 **Geological map of the Faroe Islands with a stratigraphic log.** A) Stratigraphic map of the Faroe Islands and B) a stratigraphic log of the onshore FIBG, including key horizons. Adapted from Passey and Bell, (2007).

2.1.2 Beinisvørð Formation

Volcanic eruptions of NW-SE striking rifts led to some of the thickest lava flows in the FIBG with simple flows up to 70 m thick, creating the Beinisvørð Formation (BF; Rasmussen, 1968 1970; Waagstein et

al. 1984; Waagstein 1988; Ellis et al. 2002; Passey & Bell 2007). The Beinisvørð Formation is ~3km thick, with the final 900 m exposed on the Faroe Islands (Petersen, 2014). The majority of the lava flows are of simple type with wire-line logs form the Lopra-1/1A well showing the formation to be composed of 88% simple and 12% compound flows (Petersen, 2014). This formation consists primarily of aphyric lava-flows dominated by plagioclase and clinopyroxene with less numerous volcaniclastic beds up to one metre thick separating some of the flows, rising in number towards the top of the formation (Petersen, 2014).

2.1.3 Prestfjall and Hvannhagi Formations

A hiatus in volcanic activity followed the emplacement of the BF. Wetland basins developed, and the subaerial lavas became forested (Passey and Jolley, 2009). These basins were subsequently submerged, creating the Prestfjall Formation (PF), a coal-bearing unit containing two 1.5 m and 30 cm thick beds of volcanogenic mudstones and sandstones (Ellis *et al.*, 2002; Passey and Jolley, 2009).

The Hvannhagi Formation (HF) lies directly above the Prestfjall coal-bearing formation and is located on Suduroy and Vagar (Figure 6). The formation is discontinuous and variable in thickness ranging between 0-50 m, comprising channel type clastic and volcaniclastic material deposited towards the end of the volcanic hiatus (Ellis *et al.*, 2002; Passey and Bell, 2007; Petersen, 2014).

2.1.4 The Malinstindur Formation

Volcanic activity became more frequent, lower in volume, and more continuous at the end of the hiatus, which resulted in the preceding PF and HF (Rasmussen and Noe-Nygaard, 1970; Passey and Bell, 2007; Passey and Jolley, 2009). These eruptions reflect the Malinstindur Formation (MF), a congregation of compound lava flows with little interruption of volcaniclastic beds. The formation is thickest in the North and thinnest in the South. Generally, the lava flows are up to 20 m thick, consisting of 1-2 m accumulations of pahoehoe flow lobes indicative of high-frequency eruptions (Passey and Bell, 2007; Petersen, 2014).

Mineralogically the MF consists of two zones, a lower ~450 m thick section of mostly olivine-phyric basalt, followed by a dominance of plagioclase-phyric basalts and separated by a 100 m thick olivine-phyric flow (Rasmussen and Noe-Nygaard, 1970; Waagstein, 1988; Passey and Bell, 2007). Inter lava beds showing a composition of reworked palagonitised basaltic glass increase in abundance towards the top of the formation due to growing time between volcanic activity (Passey and Jolley, 2009). A distinctive laterally persistent inter-lava bed, known as the Kvivik beds are located ~780 m from the base of the formation. The beds comprise a distinctive reddish coloured basal sandstone beneath a volcaniclastic conglomerate intruded with brown aphyric basalt further overlain by a green-red volcaniclastic sandstone (Passey and Jolley, 2009).

2.1.5 The Sneis Formation

After the MF, the Sund Beds were deposited, marking the Malinstindur–Sneis Unconformity and the onset of a major hiatus in volcanic activity (Petersen, 2014). The beds comprise a poorly sorted coarse-volcaniclastic sandstone-conglomerate forming a <1 m thick layer overlain by a thick green-grey coloured conglomerate, both deposited from mass flow events and intruded with olivine-phyric basalt (Rasmussen, 1968; Passey and Jolley, 2009). The Sneis Fm (SF) rises to 30 m thick and is highly variable. The contact between the MF and the SF is described by Passey and Jolley (2009) as being relatively continuous across the Islands.

2.1.6 The Enni Formation

The final formation within the FIBG is the Enni Formation (EF), a 900 m thick succession of compound and sheet flows consisting of plagioclase and olivine phyric basalt with numerous volcaniclastic inter-lava beds. The formation is bound on its lowest extent by a topographically variable disconformity known as the Sneis-Enni Unconformity before progressing into olivine phyric flows (Rasmussen, 1968; Passey and Jolley, 2009). The flows show an average thickness of ~15 m, although they may be up to ~30 m (Passey and Jolley, 2009). The lower section of the formation contains more numerous compound flow lobes of plagioclase-phyric basalt, filling topographic lows in the Sneis formation and causing thicknesses up to 78 m.

Zeolite studies have shown that ~1 km of the EF is missing from erosion experienced on the Faroe Islands (Passey and Jolley, 2009). The ~1 km of missing material means the exposed formation today underwent burial metamorphism forming significant secondary mineralization, mostly in zeolites filling porosity. This secondary mineralization is less extensive in higher stratigraphic levels of the Enni Formation found in offshore reservoirs where this erosion has not occurred and underwent less burial metamorphism (Chalmers and Waagstein, 2006; Passey and Jolley, 2009).

There are two distinctive horizons within the EF: the laterally extensive 10-15 m plagioclase-phyric flow known as the Høvdhamarin Flow at ~125-175 m from the base of the formation and the 1-13 m thick volcaniclastic unit known as the Argir beds located at ~250 m from the formation base (Passey and Jolley, 2009; Petersen, 2014). The Argir beds comprise of upward coarsening sediment from fine-claystone and mudstone through to very coarse sandstone of eroded palagonitised basaltic glass (Passey and Jolley, 2009; Pokorný, Krmíček and Árting, 2015). Simple flow types dominate above the Argir beds in the central part of the formation, forming flows between 5-10 m thick (Petersen, 2014).

2.2 Lava flow groups

The lava flows of the Faroe Islands contain two main groups, ones containing olivine and those devoid of olivine. These lava flow types may be grouped to indicate the classification of low and high-Ti flows,

where low-Ti flows express TiO_2 values <1.5 wt% and high-Ti flows >1.5 wt% (Waagstein, 1988; Millett *et al.*, 2017). These groups' significance comes from the presence of olivine, a mineral noted for its fast carbonization rates (Matter, Takahashi and Goldberg, 2007). Millett *et al.* (2017) state that low-Ti flows are more commonly associated with higher stratigraphic levels and more primitive or larger melt fractions, causing depleted LREE signatures with La/Sm ratios of <1, whereas High-Ti flows show LREE enrichment (Millett *et al.,* 2017). These olivine bearing low-Ti flows are expected to be more abundant in the higher stratigraphic levels achieved in offshore settings.

Further evidence for the presence of lava groups is provided by Dahren *et al.* (2015). The Faroe Islands lava flows show plagioclase as two groups based on their composition being within An60-80 or An80-90. Dahren *et al.* (2015) states these two groups represent two individual reservoirs at different depths, a result of temperatures and lithostatic pressures influencing the composition of the plagioclase. The plagioclase crystals also show homogeneous cores and a thin rim of more Na-rich plagioclase. Dahren *et al.* (2015) notes that the homogeneous core represents stable conditions during growth, whereas the thin sodic rim represents the small amount of time of changing temperature and lithostatic pressure during the ascent of the magma emplacement and solidification. This may have significance for the amount of available Ca^{2+}, which is greater in the An60-80 group, to be consumed to form carbonates.

2.3 Reservoir characteristics

Several studies have investigated properties of the FIBG which can be applied to reservoir characteristics (Passey and Bell, 2007; Vosgerau *et al.*, 2011, 2016; Ólavsdóttir, Andersen and Boldreel, 2015; Ólavsdóttir, Eidesgaard and Stoker, 2017). Vosgerau *et al*, (2011, 2016) found inter-lava beds to be laterally extensive, providing ranges between 2.7 – 7 km. Vosgerau *et al*. (2011) attribute this consistency to overlying flows being emplaced in a non-erosive nature. Thickness variations within inter-lava beds range between 1-6 m with erosional features like conglomeratic filled channels cutting through flow units connecting inter-lava beds on a scale large enough to connect several layers (Vosgerau *et al*., 2016). It is also noted that an underlying flow's topography may also cause lateral limitations to inter-lava beds due to onlapping against a rising relief and compartmentalization from cross-cutting structures such as lava tubes, lava-filled channels, and dykes (Vosgerau *et al.*, 2011).

Lava flows are generally much thicker than inter-lava beds and show more variable lateral extents (Vosgerau *et al.*, 2011). This continuity is presented in Vosgerau *et al.* (2016), where flow thicknesses of up to 20 m thinned out over 1-3 km. This thinning results in the convergence of successive inter-lava beds contributing to the connectivity of reservoirs (Vosgerau *et al.*, 2016). Conversely, Passey and Bell (2007) acknowledged the presence of laterally continuous sheet lobes of ~10 km; although

compound flows displayed more local extents, a result of magma surges from point-sourced low shield volcanoes with steady magma supply of fissure type systems forming simple flows. These suggest lateral flow extents are influenced by flow type.

2.4 The relationship to offshore areas

The Faroe Islands have previously been used as an analogue to understand the offshore flood basalt sequence within the NAIP, such as within the Faroe Shetland Basin (Jerram *et al.*, 2009; Vosgerau *et al.,* 2016). Drilling investigations as part of the Ocean Drilling Project, or more recently termed International Ocean Discovery Project (IODP) recovered cores from the Vøring Plateau Margin (VPM) one of which was the 642E core (Eldholm, Thiede and Taylor, 1989; Planke, 1994, 2021). The VPM is part of the greater NAIP, much like the FIBG and share similarities. The upper series of the VPM contains subaerial lava flows, interbedded with thin volcaniclastic beds, split by dykes and sills, similar to those seen within the onshore FIBG. The onshore FIBG stratigraphy on the Faroe Islands is expected to act as an analogue to the offshore FIBG, herein referred to as offshore settings, and parallels may be drawn to areas further afield within the NAIP such as the VPM. Therefore, the Faroe Islands may provide important information of the internal facies relationships seen within lava flows that may be applied to these offshore areas and aid to the understanding of the buildup of volcanic passive margins. These offshore areas are expected to be more suited to an injection scenario than the Faroe Islands itself due to the findings of open porosity and could act as areas of interest for CO_2 injection. with the 642E well showing significant open porosity within the upper formation (Planke, 1994)

Methods

This thesis combines observations on reservoir characteristics with new laboratory experiments to explore the nature and rates of potential basaltic CO_2 storage injection within an offshore reservoir within the FIBG. Furthermore, petrographic and petrophysical analyses, including micro-CT investigations, are carried out to understand the geochemical distributions and fluid migration pathways within lava flows and inter-lava beds. These were investigated using samples obtained from a field trip between 25th June and 8th July and by Jarðfeingi in December 2020. Furthermore, dissolution experiments were carried out at Reykjavik University between 13th May – 27th June 2021. Table 2 shows the workflow untaken in this study, with each step further developed in the following sections.

Table 2 ***Workflow of methodology****.*

Method	Description	Reasoning
Fieldwork	Dates: 25th June - 8th July	To collect images for photogrammetry, provide an overview of the geology and stratigraphy, and outline a sampling trip.
Photogrammetry	Creation of 3D photorealistic models	For general descriptive purposes, visual aids to sampling rational and lateral, vertical, and thickness measurements of the stratigraphy.
Sampling	Collection of 43 samples	To build a greater understanding of how CO_2 enriched fluids may interact in offshore reservoirs using the Faroe Islands as an analogue.
Mineralogy	Analysis of the mineralogy of the sample using a combination of petrographic microscopy and SEM. Particular emphasis was put on five samples used for dissolution tests.	Primarily to understand the ability of Faroese rocks to undergo carbonate mineralization and explain their influence on the rocks dissolution rates.
CT scans	Three cores each representing a lava flow top, core, and base.	Understand how fluids may migrate away from main fluid pathways.
Surface areas	Surface areas were cauculated vai geometric princliple but also measured using BET surface area analysis.	Geomentric surface area was used to compare the dissolution rates with literature with not BET surface are analysis BET surface areas were measured as they are a more accutate representation of the true surface area.
Dissolution rates	Batch reactive testing using 5 reactor cells containing 4 g of volcanic or volcaniclastic material, where a pH 4 solution was continuously run into the cells until steady states were obtained. Carried out between 13th May – 27th June.	The dissolution of silicate minerals is the rate limiting step to mineral trapping reactions. These experiments provide information between different flow zone and sedimentary units that too can be compared to similar research from Iceland and the CRBG.

3.1 Fieldwork and sampling

Fieldwork on the Faroe Islands was conducted during summer 2020 with the main objectives to carry out photogrammetry, a limited sampling reconnaissance, and a reference for future work, including viewing core sections to be used in this project. Fieldwork focused on the MF and EF, with particular emphasis on the latter.

A second field trip for sampling was planned for August 2020; however, it was cancelled due to the Covid-19 pandemic. Therefore, Jarðfeingi, the Faroe Islands geological survey, undertook the necessary sampling on our behalf, with samples arriving in early January 2021. The objective of sampling was to focus on the EF and Upper MF. Compared to lower equivalents, these stratigraphic levels have lavas and inter-lava beds with less secondary mineralization due to younger ages and lower burial loads, the latter correlating with potential offshore reservoirs. Furthermore, sampling focused on the cores: Glyvursnes-1, Grønadalsnøva-1, and Tjørnunes-2 and Five ~1kg samples for dissolution testing sampled at Glyvursnes Quarry. The locations of samples used in this thesis can be found in Figure 9.

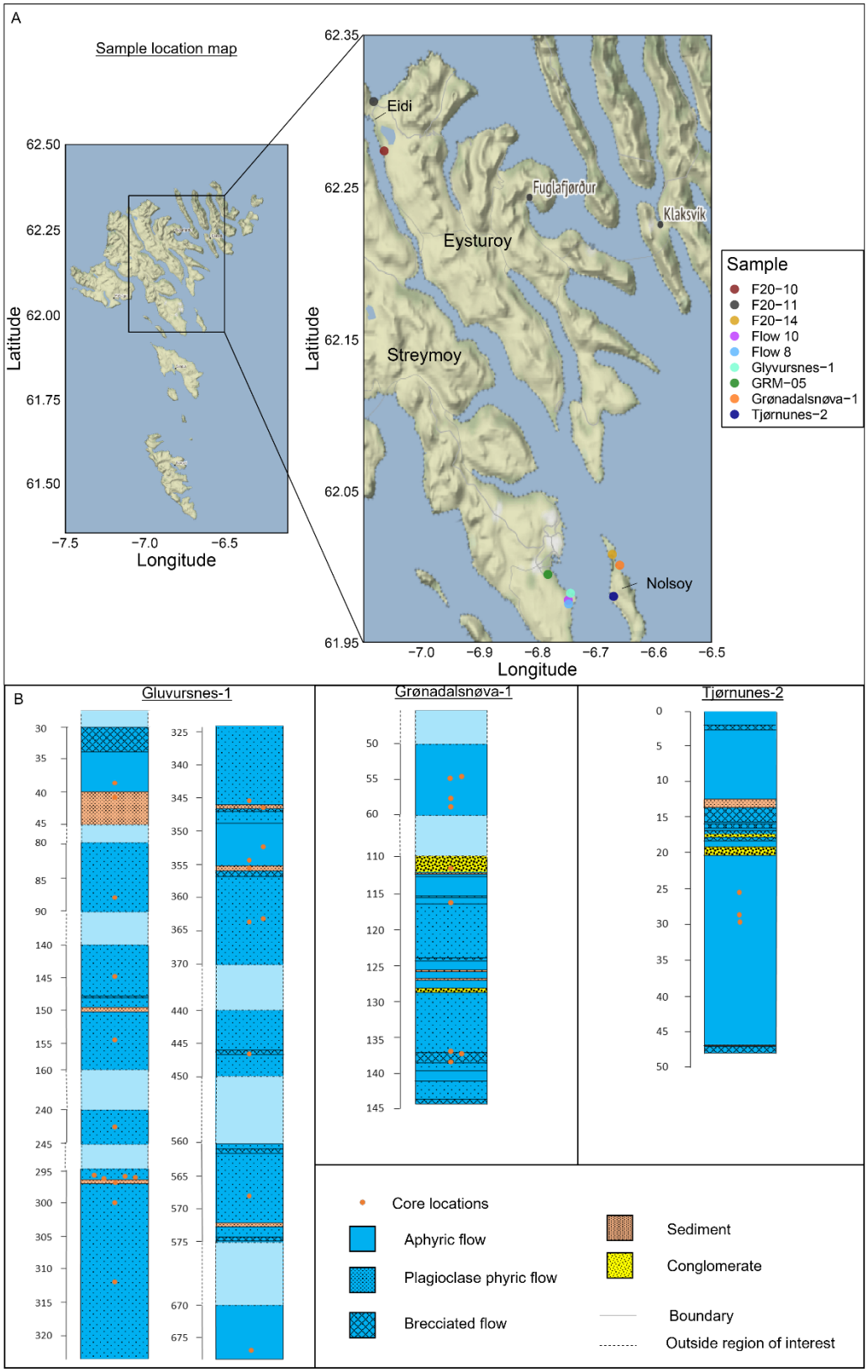

Figure 9 ***Sample localities.*** *A) The Sample location map shows the cores' locations, solubility samples, and samples for CT analysis. F20 samples were used for CT analysis, whereas flow 8, flow 10. And GRM-05 are the locations of the samples for the solubility analysis. B)The cores show the depths and lithology the samples were taken. Maps were created from: ggmap package v3.0.0.*

The majority of these samples came from the cores and were selected using core images provided by Jarðfeingi; however, some images were low-quality, making it hard to identify areas of interest. A full sample list can be found in the Appendicies (Table A. 1).

3.2 Photogrammetry

This study uses Structure from Motion (SfM) photorealistic software, Agisoft, to build 3D VOM's to be interpreted using the software package LIME (Agisoft Metashape version 1.5, 2019; Buckley *et al.*, 2019). The workflow behind the photogrammetry can be seen in Table 3. In conjunction with the creation of photogrammetric models, two completed models were provided by GEUS (the Danish Geological Survey), displaying extensive sea cliffs at Sandoy and Svinoy; the methodology for the development of the GEUS models may be found in Vosgerau *et al.* (2016).

Photogrammetry produces a model accurately representing the environment or physical object composed of oblique and vertical images. The photogrammetry process comprises data acquisition, photo-editing, image alignment, density cloud formation, and mesh and texture building. The technique to build 3D photorealistic models follows the SfM format instead of other techniques that require accurately measured locations and camera locations or control points. SfM software only requires more than two overlapping images of the feature in question (Westoby *et al.*, 2012; Agisoft Metashape version 1.5, 2019). The SfM software builds the 3D model based on algorithms that measure the camera positions during image acquisition by using common features within images (keypoints) to build a density cloud comprising of points that are not scaled or orientated (Westoby *et al.*, 2012; Agisoft Metashape version 1.5, 2019). The software is limited by image resolution, the density of images, image sharpness, and object texture. These must be considered while deciding the resolution of the output model (Westoby *et al.*, 2012; Agisoft Metashape version 1.5, 2019). Once the density cloud is computed, a mesh may be applied and overlaid with a textured surface to produce a Virtual Outcrop Models (VOM) for interpretation.

Image acquisition for photogrammetry focused on the Faroe Islands' north-eastern extent due to better exposure and higher stratigraphic level. All 450 images were taken at Vidoy, Vidareidi, and Eidi over three days to produce five panoramas (Figure 10). In general, two photogrammetry types were collected: 1) large landscape scenes to help show lava flow and volcaniclastic bed continuity, connectivity, and compartmentalization requiring long and high exposed cliff faces; and 2) detailed virtual outcrops to aid more in-depth petrographic analysis. Figure 10 shows the localities of all models used within this thesis.

Table 3 ***Photogrammetry workflow***

Source	Action	Method	Reasoning
Nikon 7100 and DJI mavic 2 pro drone	*Photo acquisition*	*Nikon: Shot in RAW* *Drone: Shot in RAW and HDR*	*Provide high-quality photos in a range of scales, from close-ups to landscapes.*
Photoshop	*Photo editing*	*Adjust brightness, contrast, and saturation of photos and perform sharpening and batch automotive processing.*	*The software package allows the editing of photographs using an automotive process of repetitive tasks.*
Agisoft	*Photo stitching and 3D imaging*	*Uses a series of tasks to produce a model: Align photos, build density cloud, build mesh, and build texture.*	*The software provides a realistic 3D model.*
LIME	*Visualization and interpretation of outputs from Agisoft*	*Line interpretation for both lava flows and inter lava beds where an interpreted overlay was then applied on the finished product. Unit extents were subsequently measured using the line tool.*	*Allows for the straightforward interpretation of photorealistic textured models to understand layer variability in lateral and vertical extents.*

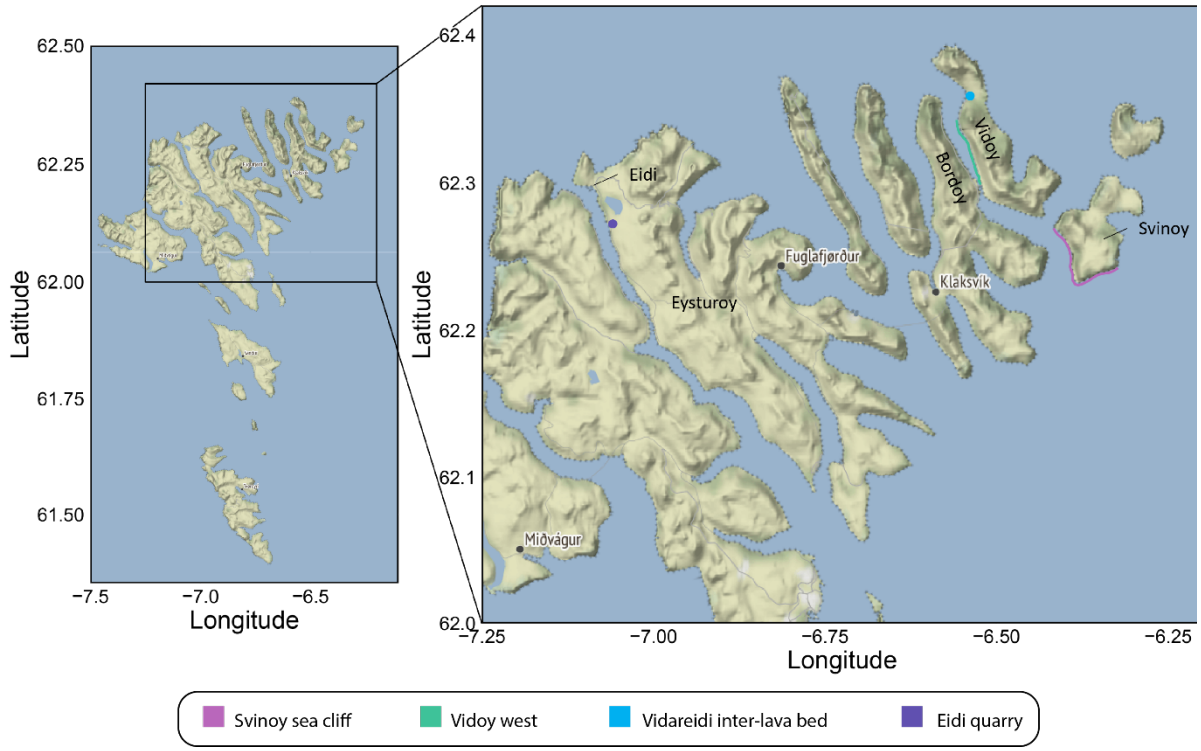

Figure 10 ***Map showing the locations of the photogrammetric sections.*** *Dots represent the small scale VOM's and the lines the large landscape VOM's. Map created from: ggmap package v3.0.0.*

3.2.1 *Image acquisition*

Images were acquired using one of two methods, a handheld Nikon 7100 camera and a DJI Mavic 2 Pro drone with a hasselblad lens. The drone reached inaccessible areas, although its usage time was limited, therefore which method used depended on the accessibility of an area and time needed for data acquisition. The drone displayed vertical and horizontal distance to surfaces in conjunction with the camera angle, allowing for consistent image acquisition. Both cameras were set to their respective raw formats for maximum image editability, and an overlap of 50-70% was implemented to provide the best chance of image alignment.

3.2.2 *Editing*

The images were uploaded to Photoshop CS6, where basic edits were made to individual photographs such as brightness, contrast, and saturation. Shadows were also removed by selecting the area and brightening to look the same as the rese of th image. Following the the brightening the edges need to be blured using a gaussian filter and subsequently gone over using the smudge tool to remove any remaing shadow.

3.2.3 *Stitching*

Panorama stitching was performed using Agisoft, a standalone program designed explicitly for photogrammetric processing producing 3D models (Agisoft Metashape version 1.5, 2019). Agisoft requires a series of processes to generate the model, these being 1) image alignment, 2) density cloud creation, 3) mesh building, and 4) texture. Each procedure can be adjusted to provide a specific quality where each elevated step in quality increases running time (Agisoft Metashape version 1.5, 2019).

Photos taken at a distance (>1 km) struggled to align, so common markers were placed on overlapping photos to aid the alignment process. The specific parameters used for each model can be seen in Table 4. The Svinoy sea cliff was not included as GEUS produced this.

Table 4 ***The quality of each photogrammetric model***

Model	Quality	Reason
Eidi Quarry	*High*	*A small number of photos with good overlap, thus not time demanding.*
Vidoy West	*Medium*	*The number of photos was large and computer processing speeds limited the quality.*
Vidareidi Inter-lava bed	*High*	*Small number of photos with good overlap, thus not time demanding.*

3.2.4 *Interpretation*

The use of the photogrammetric models helps classify the lateral continuity, thickness variations, stratigraphy, and structural relationships of any potential reservoir units. The methodology used in interpreting the models was developed by the Virtual Outcrop Geology Group, Norwegian Research Centre (NORCE), Bergen, Norway. The method creates a simplified rendered 3D image for visualisation purposes. Interpretations such as measuring extents and thicknesses were performed in LIME, a software package that allows viewing and interpreting 3D models (Buckley et al., 2019). LIME allows the user to interpret linear and planar features on a VOM, with the addition of exporting panels to Illustrator to create colour filled overlays to be draped over the 3D model.

3.3 Sample Analysis

The analysis focused on petrographic and petrophysical techniques to better understand the reactive mineralogy, fluid migrations away from major pathways, and dissolution rates of both the lava flows and inter-lava beds. The following subsections explain each technique and the reasons for being used.

3.3.1 *Petrographic Thin Sections*

23 thin sections have been studied to constrain sample mineralogy, alteration, and associated microstructures. Selected rock samples were cut with a diamond-edged saw to the correct size for a thin section plate. The samples were then impregnated with epoxy, glued to thin section plates, and cut and polished to approximately 35 μm. The thin section workshop prepared all thin sections at the Geoscience Department, University of Oslo. Of the thin sections, 8 could not be completed because they would lift from the glass during polishing, losing significant material. Thin sections were prepared in two batches, the first in October 2020 from the fieldwork sample set and the second in February 2021 from the samples collected by Jarðfeingi.

3.3.2 *Optical mineralogy*

The study used a standard optical transmitting light microscope with options for both plane-polarized light (PPL) and cross-polarized light (XPL) microscopy to identify mineralogy, textures, and structural features within the thin sections.

3.3.3 *Scanning Electron Microscope (SEM)*

The analysis was undertaken using a Hitachi SU5000 FE-SEM Scanning Electron Microscope (SEM). 8 polished sections were interpreted. SEM analysis aimed at imaging polished sections to produce Back Scatter Images (BSE) images of areas of interest observed within optical microscopy. The polished sections needed to be carbon-coated to provide a conductive layer before analysis. Further analysis was carried out using an Energy Dispersive X-Ray Spectroscopy (EDS) with a Dual Briker Quantax Xflash 30 EDS to examine semi-quantitative chemical compositions aiding mineral identification and EDS

element maps to provide element distributions within minerals, with a minimum running time of 30 minutes.

3.4 Computed X-ray tomography (CT)

CT scanning with micrometre resolution (μCT) was done to characterize the internal pore structure of the analysed samples. The goal is to constrain possible paleo-fluid migration pathways in lava flows away from the main fluid pathways. The application of which can aid in understanding how a reservoir may act and evolve in an injection scenario. Core plugs were taken from three key samples representing flow top, core, and base flow architectures. Scanning the plugs provided information on density, secondary mineralization, and micro-fractures with a resolution of up to 6 microns in a non-destructive manner (Couves, 2015).

3.4.1 *Obtaining 3D scans*

In total 3 core-plugs were produced at Njord, University of Oslo of 25 mm diameter with a thickness of ~20 mm. The samples were subsequently sent for analysis at Grenoble, France's European Synchrotron Radiation Facility (ESRF). The scanning process involves the bombardment of monochromatic x-rays passing through differing densities within the sample, creating a greyscale image of 3D pixels, known as voxels (Couves, 2015). During analysis, the samples were rotated a total of 180° in small increments while the x-ray beam was varied, producing the 2D image slices (Callow *et al.*, 2018).

Scans were performed under a 200 mA current with a 83 KeV peak X-rays spectrum. 6000 projections were acquired in local tomography over 360 degrees with an half acquisition protocol off-centered by 900 pixels. Exposure time was set at 30 ms with a PCO-edge 5 with an optical setup of 6 micrometers per pixel. The scintillator was a LuAG:Ce with a 100 micrometers thickness. Each projection was 2048 pixels wide and 640 pixels high, leading to vertical series of 7 to 8 scans for a full sample. Scans were later stitched together, finishing with final reconstructed volumes of 3861x3861x3500 voxels.

3.5 Imagej and Trainable weka segmentation

The resulting CT scans were fed into Imagej, an open-source java-based software containing various plugins to carry out statistical analysis of images (Collins, 2007). Trainable weka segmentation (TWS) is a plugin to Imagej that allows for computational learnings from simple interpretations used to segment an image or a set of images into a series of classes (Arganda-Carreras *et al.*, 2017; Pettus, Pettus and Virginia, 2021). This significantly reduces the interpretation timescales and allows for quick and simple statistical analyses, such as percentage areas. The ability to perform percentage area analysis for specific classes is of use for modal abundances on thin sections or BSE images from SEM analysis, for and classifying porosity and secondary mineralization within CT scans.

Before the classification of the images, enhancements in brightness and contrast were carried out within Fiji to improve interpretation accuracy. Furthermore, specific settings were selected to provide optimised results. These settings were decided based on findings from Lormand *et al.* (2018), and Pettus and Virginia (2021):

- Gaussian blur that combines similar pixels.
- Lipchitz to blend the background, which shows little ranges in greyscale value.
- Gabor to provinde better edge detection.
- Bilateral which blurs the edge of an object to average the pixels aiding the edge preservation of the object.
- Neighbours which shifts an image in eight orientations to generates eight feature images.

This study focused on calculating mineral abundance within the solubility samples and the proportion of pore space and secondary mineralization within the CT samples. The number of classes to be used on each sample was determined based on the objective of the analysis. The number of classes used for the BSE images was confirmed from petrological observations for the thin sections; however, only three classes were used for the CT scans: groundmass and phenocrysts, pore space, and secondary mineralization. Each object shows a particular density and thus a specific range of grey scale values. These regions of interest (ROI) can be represented by drawing over a certain area on the image to form a class. Importantly, it was found TWS can be overtrained and it must be trialled how many drawings are needed to represent a class. Once a basic interpretation is carried out, the plugin can be trained using this simple interpretation to identify the classes throughout the image.

Segmentation of the images was completed using FastRandomForest algorithm, which classifies the data using a group of decision trees based on the input of training features, whereby the algorithm builds the trees based on randomly selected training features and sorts unassigned pixels accordingly (Lormand *et al.*, 2018). The algorithm was picked for speed, accuracy, and the ability to carry out multiple segmentation (Lormand *et al.*, 2018). Once the training is complete, the result is overlain on the original image with some transparency, allowing the user to check the quality of the interpretation. If the interpretation is deemed a good representation of the desired classes, the classifier may be saved and applied to other images of stacks of images. The other images must only contain the the ROI within the classifier and have similar brightnesses/colours. Once results are created, desired statistics of each class within the image or stack of images can then be carried out using the measurement plug-in.

3.6 Whole-rock analysis

The samples for the solubility analysis were sent to Actlabs, Ontario, Canada, for analysis of whole-rock chemistry, using Inductively Coupled Plasma Mass Spectrometry (ICP-MS) in March 2021. Representative parts of each sample were collected and cut into ~30 g sections to be sent for analysis. For the raw data, refer to the Appendices (Table B. 1and Table B. 2).

3.7 Solubility analysis

Dissolution testing aimed to investigate the ability of lava flows and volcaniclastic rocks of the FIBG to release the essential divalent cations which are essential to the mineral trapping process. The experiments were based on four lava flows and one inter lava bed, sampled from Glyvursnes, Faroe Islands (Figure 9) in December 2020. Two lava flow types were used to provided altered (flow tops) and unaltered (flow cores) from plagioclase phyric and aphyric lava flows. GRM-01 (Flow core) and GRM-02 (Flow top) represent flow 10 and GRM-03 (Flow core) and GRM-04 (Flow top) represent flow 10. Originally, analysis was planned to begin in October 2020 at Reykjavik, Iceland; however, due to travel restrictions, this was delayed until 13th May – 27th June 2021.

Proceeding dissolution experiments, thin sections were cut from the samples using the method presented in section 3.3.1. Due to the wetting process during cutting, the samples were dried at room temperature for several days before being roughly pulverized using a jaw crusher. The resulting material was ground manually in an agar pestle and mortar to a finer grain size for sieving. The following material was dry sieved, collecting a grain size range of 45-125 µm until ~40 g of sample material was collected. Much focus was spent on keeping the 45-125 µm consistent between samples as the particle size is related to reaction rates due to surface area. This particular fraction was based on previous studies (Gudbrandsson *et al.*, 2011, 2014; Stockmann *et al.*, 2011) with Icelandic rocks, and consequently, the method of sample preparation and fraction size was kept consistent to allow for comparison.

The grain fractions underwent gravitational settling to remove any grain sizes <45 µm not separated during the sieving process with the time for the lightest fraction (45 µm) calculated using stokes law (1). The settling was performed in a long column filled with distilled water. The 45-125 µm fraction was added, stirred to suspend in solution, and then left for the 45 µm grains to settle and repeated until the water in the column was clear. The drag force *F*, can be calculated using stokes law:

$$F = 6\pi rnv \qquad (8)$$

where *r* is the sphere radius, *n* fluid viscosity, and *v* is the settling velocity. The velocity was then used to calculate the time for the 45 µm fraction to settle using:

$$t = \frac{d}{v} \quad (9)$$

where *t* is time (s), d is the length of the water column (*m)*, and *v* is the velocity (m/s). The calculated time was ~120 seconds when the sample was suspended in a 30 cm column. Once the time was finished, the water was carefully syphoned off, leaving the settled material, and the process was repeated until the water was clear.

The samples were transferred to a 500 ml beaker and filled with deionised water following the settling process. The beaker was then placed into an ultrasonic bath for 15 minutes and stirred at regular intervals to stop compaction of the material before having the water syphoned and the process repeated until the water was clear, removing any fine particles that could be attached to the surface of the 45-125 µm grains. The process was then repeated once in acetone to aid the removal of the particulates and washed in deionised water. Each sample fraction was then left to air dry in the laboratory for three days.

Once in Iceland, dissolution experiments were performed at pH 4 in a series of reactors, as shown in Figure 11. The procedure consists of five polymer reactors that have an inlet and outlet and an observation port. The reactors are connected to a 25 L bucket containing the inlet solution, which passes a Masterflex L/S calibrated peristaltic pump set to a constant flow rate of 2.0 g/min. The inlet solution was comprised of deionized water and 1.0 mol/kg HCl providing a pH of 4.00. Before the experiments, all the equipment was cleaned using dilute 0.1 mol/kg HCl. The equipment was subsequently rinsed thoroughly with deionised water to remove further contamination and acid. Once the cleaning was completed, a blank was taken from each outlet.

Each reactor received 4 g of dry powder and filled with the inlet solution before being sealed, purged to remove any air, and then set to continuously stir at the desired rate being ~400 rpm to keep the gains in suspension. This stirring rate was determined by (Gudbrandsson *et al.*, 2011). During the experiments, outlet samples were retrieved regularly through a 0.2 µm cellulose acetate filter and subsequently acidified with pure HNO_3 prior to analysing Si, Na, K, Ca, Mg, and Fe using the ICP-OS at the University of Reykjavik. Directly after each sample, the pH and flow rate was taken for each reactor. The measured elemental concentrations were used to calculate the element release rate, *r*:

$$r = \frac{C_i F}{Sa} \cdot m \quad 10$$

Where C_i is the concentration of element *i* within the outlet solution, *F* the flow rate during sampling, *Sa* is the surface area and *m* the mass of sample within the reactor.

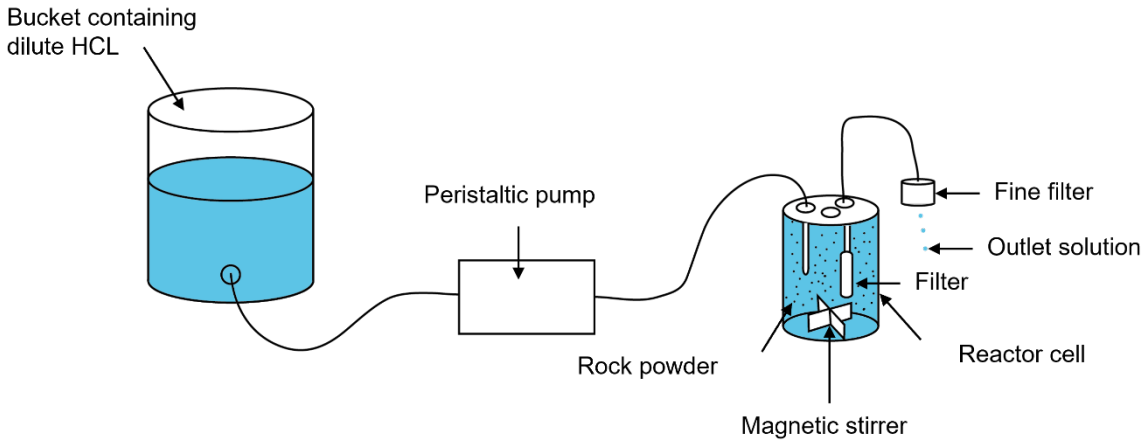

Figure 11 ***Schematic of the dissolution experiment setup.*** *A bucket filled with the pH 4 solution is connected to a peristaltic pump which draws the fluid into the reactor. The reactors are filled with the solution and 4 g of one of the samples. The continuous stirring of the magnetic stirrer keeps all the powder in suspension. The solution flows into the reactor and through the outlet passing a filter within the reactor and a finer final filter where sampling is carried out.*

The blanks taken before the experiments found Si to be present from the deionised water. Subsequent sampling found this contamination to be constant at around 0.21 ppm, and thus the experiments were continued with the Si from the blanks subtracted from the resulting Si in the outlet solutions. No other contamination was observed within the blanks. Blanks from the inlet solution were continuously taken to check that the Si contamination did not change and may be seen in the Appendicies (Table C. 1). The experiments were run until the Si release rate was constant in three samples, at least one full reactor cell volume apart. The dissolution rates in this study were only carried out once due to the limited time following delays resulting from the Covid-19 pandemic. Ideally, replicating one of the experiments could increase confidence in the results.

Elemental release rates were calculated based on the dissolution rate equation:

$$r = \frac{C_i F R}{A m} \qquad (11)$$

where C_i is the concentration of element i (mol/kg), F being the flow rate (g/min), A the surface area of the material (cm^2/g) , and m the mass of substance used (g). Desired steady state release rates defining the solubility of a rock were attained from Si concentrations based previous literature (Martin and Fyfe, 1970; Appelo and Postma, 1993; Schaef and Mcgrail, 2009; Gudbrandsson *et al.*, 2014).

3.8 Specific Surface Areas

Following the dissolution experiments both geometric surface area calculations and BET specific surface area measurements were taken for each sample. This allows the determination of the reactive surface area of each of the powders. Both sets were evaluated to compare with previous studies that use a particular surface area as BET or geometric.

3.8.1 Geometric

The calculation of the geometric surface areas was calculated using the same methodology as Gudbrandsson et al. (2011):

$$Surface\ area\ = \frac{6}{\rho \cdot deff} \quad (12)$$

with *6* used to equate fore a smooth spherical shape, ρ the density of the particles taken as the average density of basalt of 2.86 g/cm^3 from Saxov & Abrahamsen (1964), and d_{eff} being the effective particle diameter. The geometric surface area provided by this equation for all samples is 246 cm^2/g as each has the same average diameter.

3.8.2 BET

The Brunner-Emmett-Teller theory (BET; Brunauer and teller, 1938) specific surface area measurements were analysed using the Microtrac BELSORP MAX with nitrogen gas at the Catalysis section, Department of Chemistry, UIO. The method uses the gas to measure the surface area of both solid and porous materials, allowing for a more accurate determination of the grains' surface area, considering surface roughness and pores. These were measured as different samples will have different surface roughness factors that may influence the calculated dissolution rate of a sample.

The samples were added to glass vials and degassed at 150°C in a vacuum for 6 hours to remove impurities that may be physically attached to the material's surface, before being installed to the instrument for the surface area analysis. The samples surface area was established using the creation of adsorption isotherms. The BET specific surface area includes the surface roughness of the grains at an atomic level using an unreactive gas; in this case N_2, which provides a more accurate determination of the actual surface area.

During the analysis, various pressures of N_2 are injected into the vial, and thus more molecules of N_2 are adsorbed to the surface of the grains, forming a monolayer (an absorbate layer only one atom thick). By calculating the difference in pressures before and after the injection, the number of adsorbed molecules can be calculated from the volume adsorbed. Since the diameter of adsorbate is known, the surface area may thus be calculated. The quantity of adsorbed gas depends on the relative vapour pressure, which is proportional to the sample's internal and external surface, with the

connection between the quantity of adsorbed gas and relative vapour pressure providing the adsorption isotherm (Figure 12).

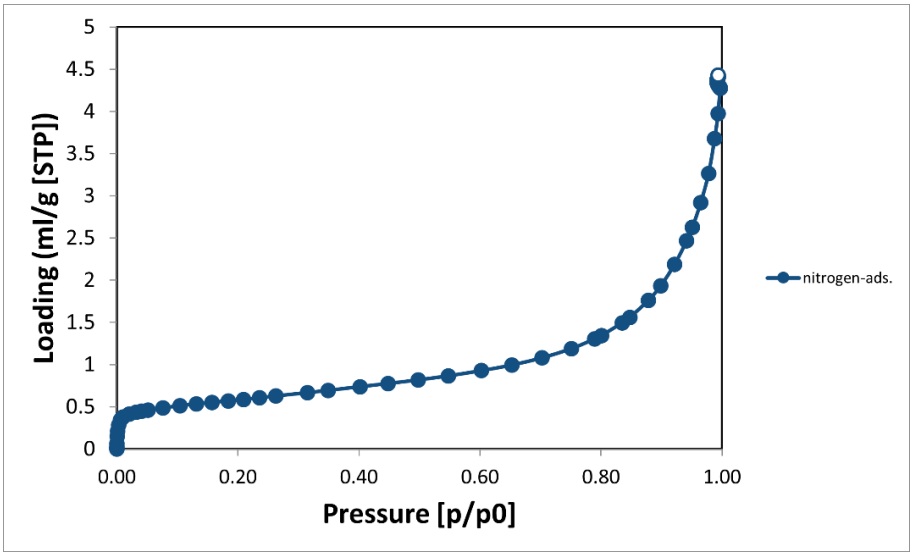

Figure 12 ***Adsorption isotherm.***

The analysis is carried out at cryogenic temperatures, achieved by liquid nitrogen and repeated at different pressures until an isotherm is created. In order to aid the calculation of low surface area samples, such as this studies samples, a glass rod was added to the vial to reduce the dead space. This reduction in dead space allows for the adsorbed portion of the nitrogen gas to be a greater proportion of the total nitrogen gas, thus allowing for smaller measurements.

Weak interactions between solids and gases represent physisorption, and the enthalpy of adsorption is very low, allowing for the gas molecule to easily become adsorbed and desorbed to the material's surface (Thomas, 2015). A dynamic equilibrium between adsorbed and free phase atoms over any adsorption pressure provides a monolayer of atoms on the material's surface. The BET equation ($\frac{1}{n\left(1-\frac{P}{P0}\right)} = \frac{1}{nm \cdot C} + C - \frac{1}{nm \cdot C} + PP0$

(*13*) is used to determine the number of molecules necessary to form a monolayer (*nm*) of the adsorbate onto the solid surface (Thomas, 2015):

$$\frac{1}{n\left(1-\frac{P}{P0}\right)} = \frac{1}{nm \cdot C} + C - \frac{1}{nm \cdot C} + \left(\frac{P}{P0}\right) \quad (13)$$

where *n* is the quantity of gas molecules adsorbed at the relative vapour pressure P/P_0, and *C* the BET constant which may only be positive as adsorption is exothermic. Thus, the equation provides a relationship between the adsorbed gas at a given relative vapour pressure.

The isotherm data from the experiments makes the BET transform plot by graphing the relative adsorption pressure against the BET function *1/[n(P0/P – 1)*. This is a linear plot limited to a certain region in the isotherm at a relative pressure (P/P_0) between 0.05-0.35.

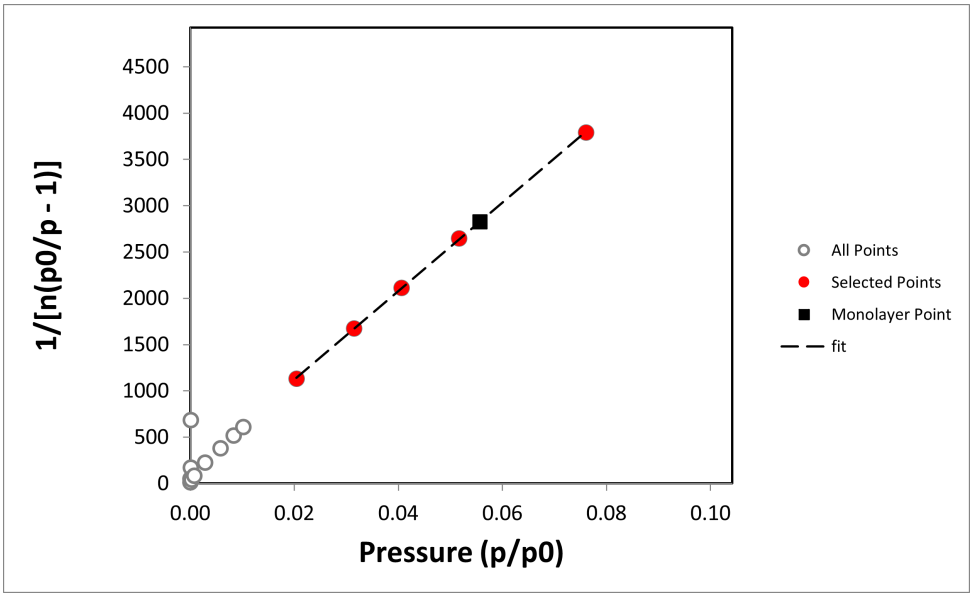

Figure 13 ***Isotherms used to define the BET specific surface area****. The white circles are the points outside the 0.05-0.35 range wich are not used in the calculation and the points deviate from the regression line due to the monolayer not being formed. This plot provides a BET constant of 287.2, positive thus correct to the BET theory and a correlation coefficient of 0.99989.*

A regression line is plotted through the points with the slope and intercept providing the monolayer capacity:

$$Nm = \frac{1}{gradient - intercept} \tag{14}$$

The intercept and gradient are also used to find the BET constant, *C*:

$$C = 1 + \frac{gradient}{intercept} \tag{15}$$

Once the monolayer adsorption volume is known, the BET surface area can be calculated per unit mass of the sample using:

$$Total\ surface\ area = \frac{Vm \cdot N \cdot S}{V} \tag{16}$$

$$BET\ surface\ area = \frac{total\ surface\ area}{m} \tag{17}$$

were *N* is the Avogrdro's number, *S* the adsorbates cross-section, and *V* the molar volume of the adsorbate gas at standard pressure and temperature, m is the mass of the sample.

Results

4.1 Photogrammetric model descriptions

4.1.1 Vidoy Fjord

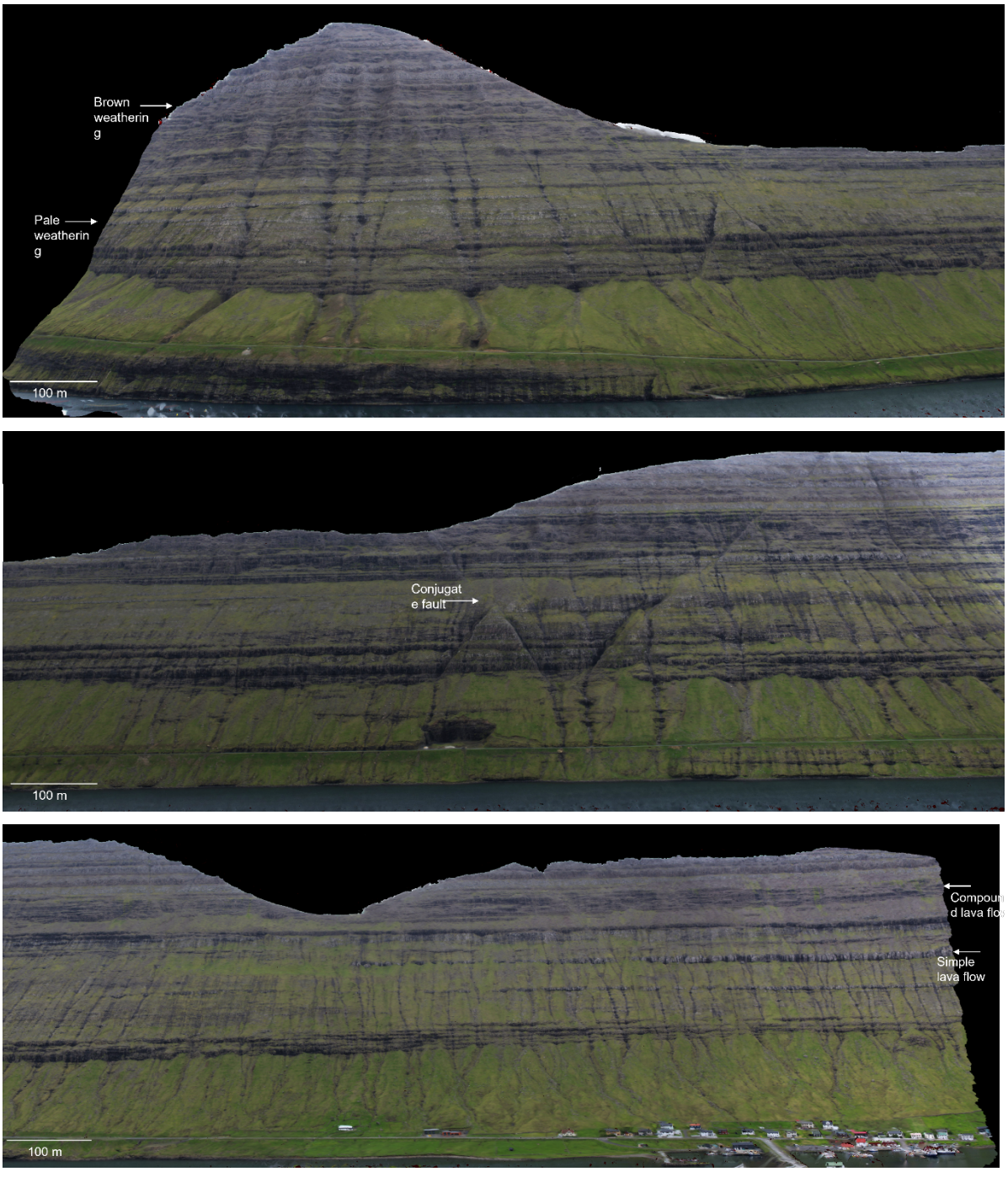

Figure 14 ***The Vidoy Fjord VOM.*** *The VOM shows a 2.5 km long sea cliff with a height of up to 600 m. The sea cliff shows limited exposure in the bottom 150 m, although the top half of the VOM shows good exposure. The VOM includes the presence of both simple and compound type flows, flow thicknesses, flow terminations, grey and brown weathering lava flows and the presence of conjugate faults.*

4.1.2 Vidoy Fjord

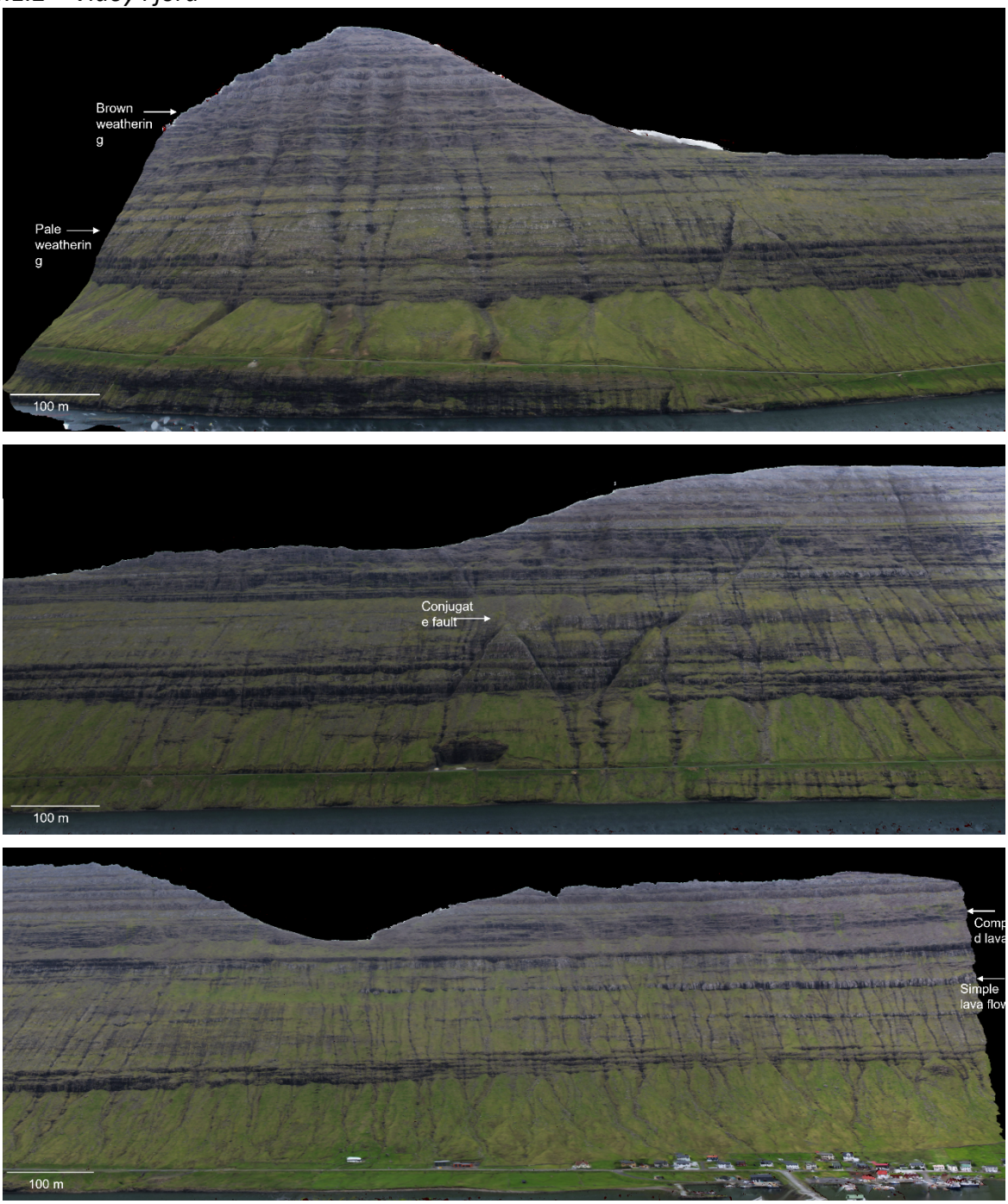

Figure 15 ***The Vidoy Fjord VOM.*** *The VOM shows a 2.5 km long sea cliff with a height of up to 600 m. The sea cliff shows limited exposure in the bottom 150 m, although the top half of the VOM shows good exposure. The VOM includes the presence of both simple and compound type flows, flow thicknesses, flow terminations, grey and brown weathering lava flows and the presence of conjugate faults.*

4.1.3 Eidi quarry

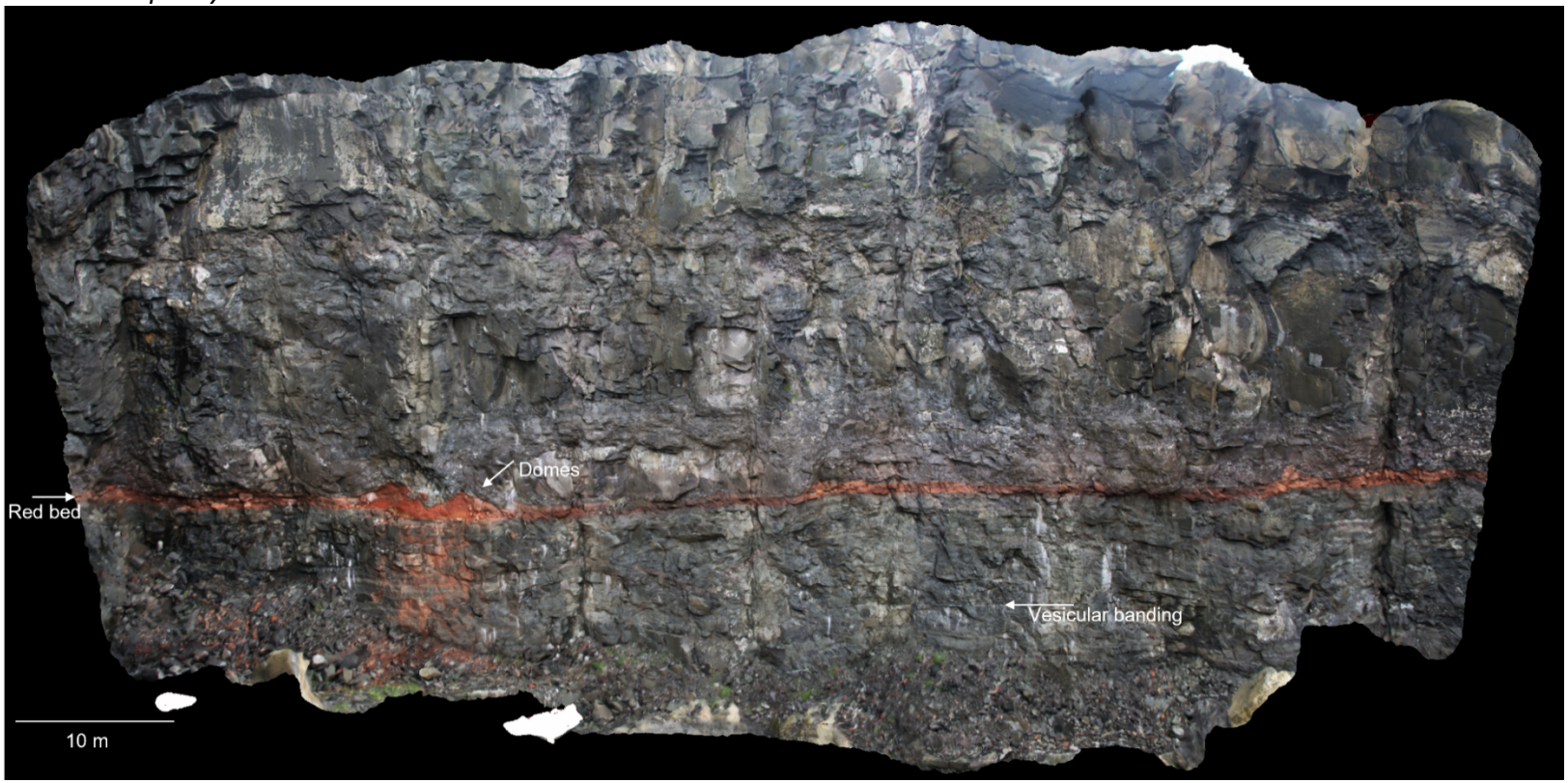

Figure 16 ***Eidi quarry. Newly excavated site with a large 100 × 50 m vertical wall.*** *Common observations include two distinct lithologies of lava flows and an inter-lava bed, vesiclular banding, zones of alteration, a lava tube, and flow terminations. The lava flows display a mostly irregular pattern of coalescing smaller flow packages indicative of compound flows. The red horizon is composed of granular material of a sedimentary bed and represents a volcaniclastic unit, displaying a relatively flat bottom that undulates slightly with the underlying lava flow whereas the top of the red beds displays a rather irregular topography with dips and domes. Above the inter-lava bed an area showing a purple hue can be seen approximately in the middle of the VOM. This area represents a flow top appearing a different colour to the surrounding flows, including a speckled pattern indicating a greater quantity of secondary mineralization to surrounding flows. Directly above the red bed, within the flow base of the overlying flow, there is an increased presence of pipe vesicles compared to other flows within the VOM but also greater concentration surrounding the domes of the red bed. Further to the pipe vesicles some of the lower flows show an accumulation of filled pores with relatively continuous bands stretching the flow unit's distance. These bands are ~ 15 cm thick and alternate between zones of more sparse vesiculation (~3-5 cm thick) and more concentrated vesiculation patterns separated by less vesicular bands.*

4.1.4 *Vidareid inter-lava bed*

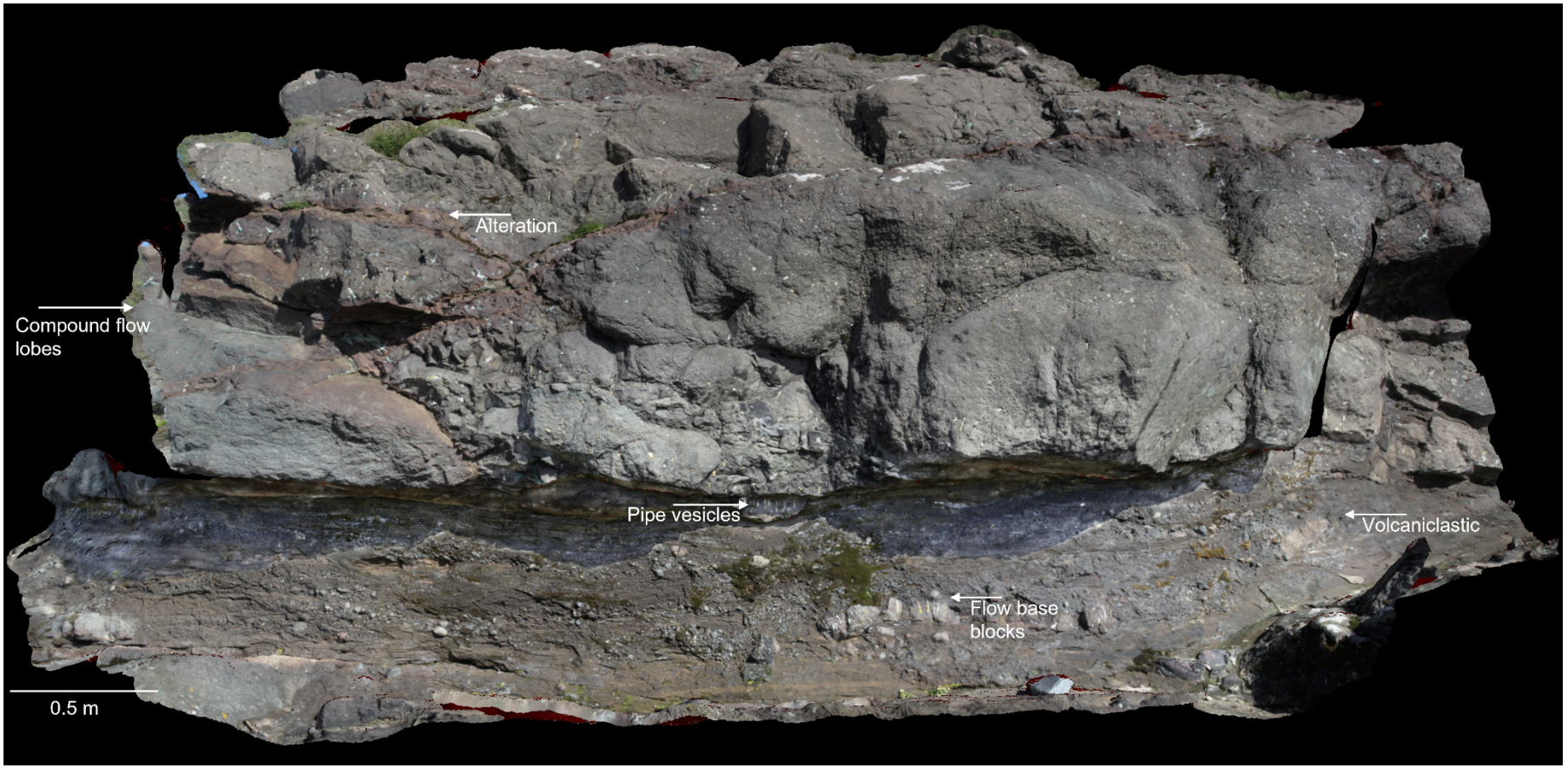

Figure 17 ***An inter-lava bed at vidareidi.*** *The model represents a 5 m by 2 m VOM displaying a 50 cm thick inter-lava bed beneath coalescing flow lobes of a compound flow. Key features show poorly sorted angular clasts representing eroded lava flows with fine parallel to sub-parallel laminations ~ 10 mm thick. The bed shows angular clasts of volcanic material up to 15 cm in size, containing filled pipe structures from their base to their top. Above the inter-lava bed, a series of flow lobs representing a compound lava flow can be seen. At the contacts between the flow lobes a 1-2 cm reddened zone extends into the reactive rock. All the lava flow lobes show filled vesiculation and pipe vesicles at their lower boundaries. The shadow seen below the lava flow edge has been reduced in this image.*

4.1.5 Svinoy sea cliff

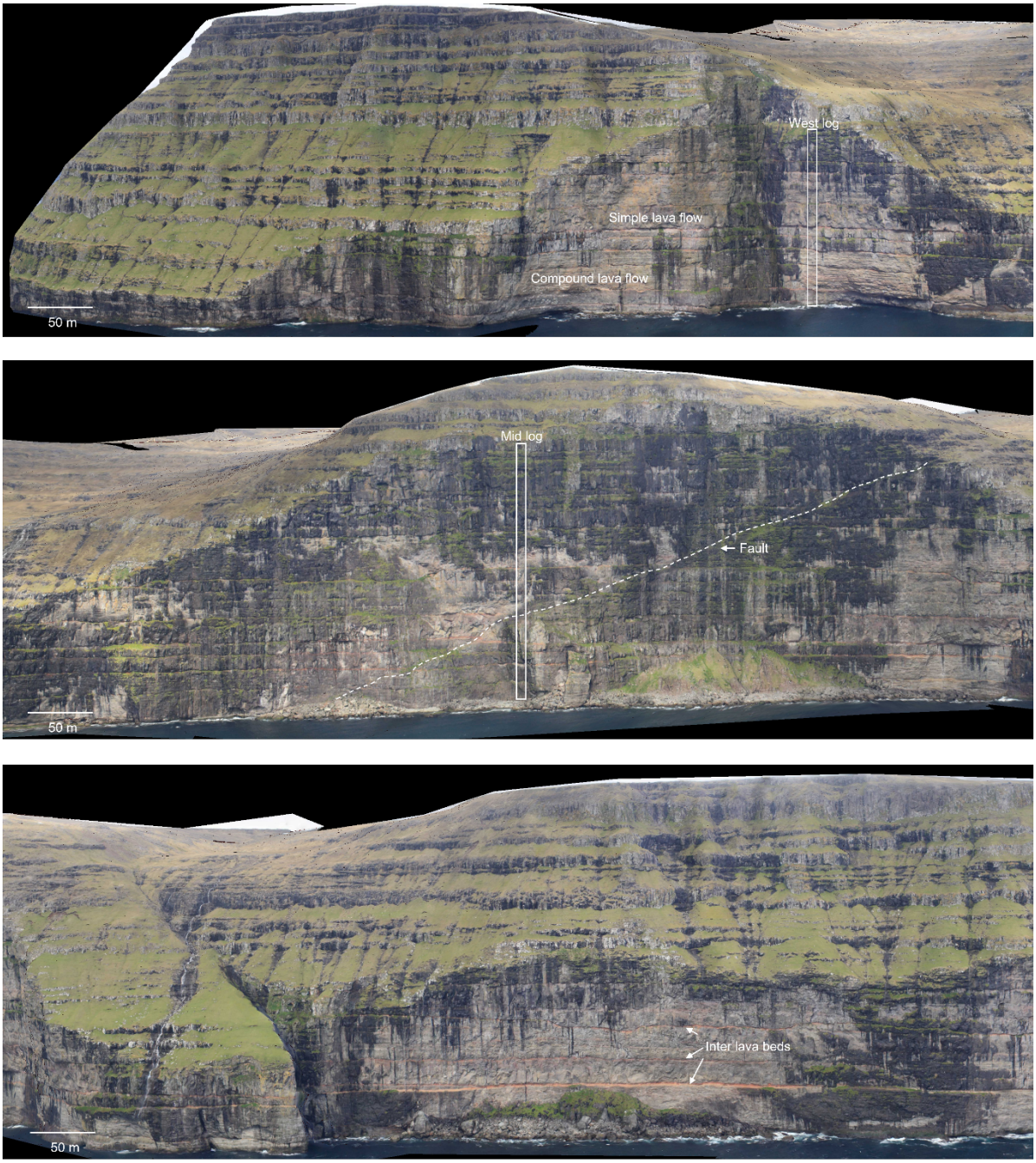

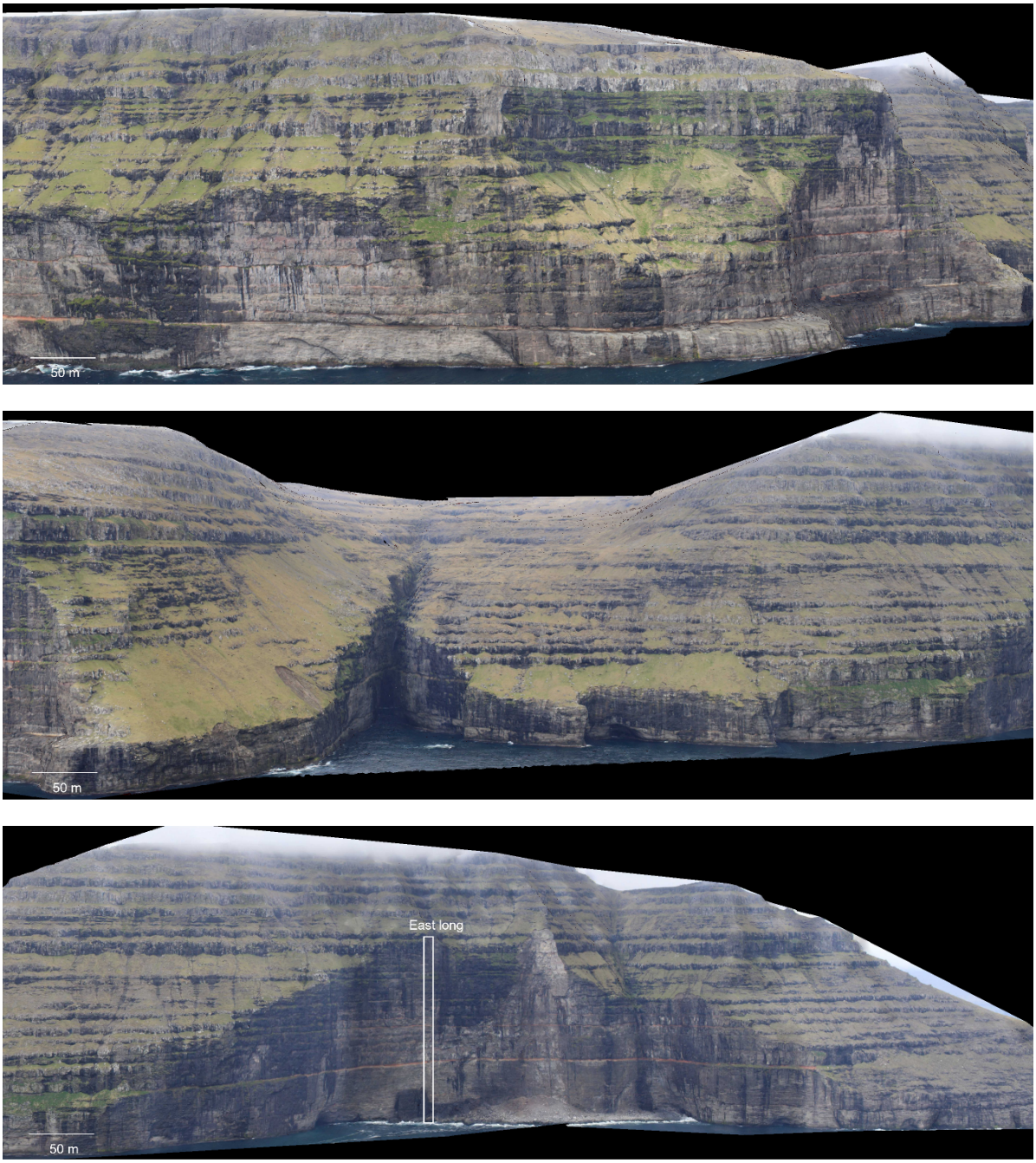

Figure 18 ***Svinoy sea cliffs.*** *The photogrammetry taken of the Svinoy sea cliff covers 600 × 4500 m, providing both laterally and vertically extensive exposure with little vegetation cover. The sea cliff contains key observations: the inclusion of both simple and compound lava flows, numerous inter-lava beds, flow terminations, joining of inter-lava beds, lava tubes, a fault, undulating tops of inter-lava beds, and erosional features such as channels. The lava flows show varying lateral and vertical extents with little columnar jointing. The lava flows show erosional features which the red horizons fill. The red horizons are inter-lava volcaniclastic beds that show a flatter bottom than an undulating top; these horizons are split by lava flows that occasionally join when the lava flows thin out.*

4.2 Field Observations and Photogrammetry

This section combines observations from the field with those from the VOM's to describe critical features of reservoir characteristics that can be translated to offshore settings.

4.2.1 *Lava flows*

Lava flows dominate the Faroe Islands, showing both simple and compound types. The simple types show greater thicknesses of inner architectures (flow crusts, cores, and bases), with flow crusts up to 11 m (Figure 19). As compound flows comprise multiple lobes in one flow, the inner architectures are significantly reduced; subsequently, their flow crusts are thinner, less than 1 m in thickness. Although the individual thickness of the inner flow architectures is smaller within flow lobes, the large quantity of these lobes produces an overall larger combined flow top thicknesses. Depressions from overlying lava flows and lobes cause a reduction in flow top thicknesses; this is especially noticeable within compound flows where depressions from the overlying flow can completely cut off the flow top of the lobe (Figure 19).

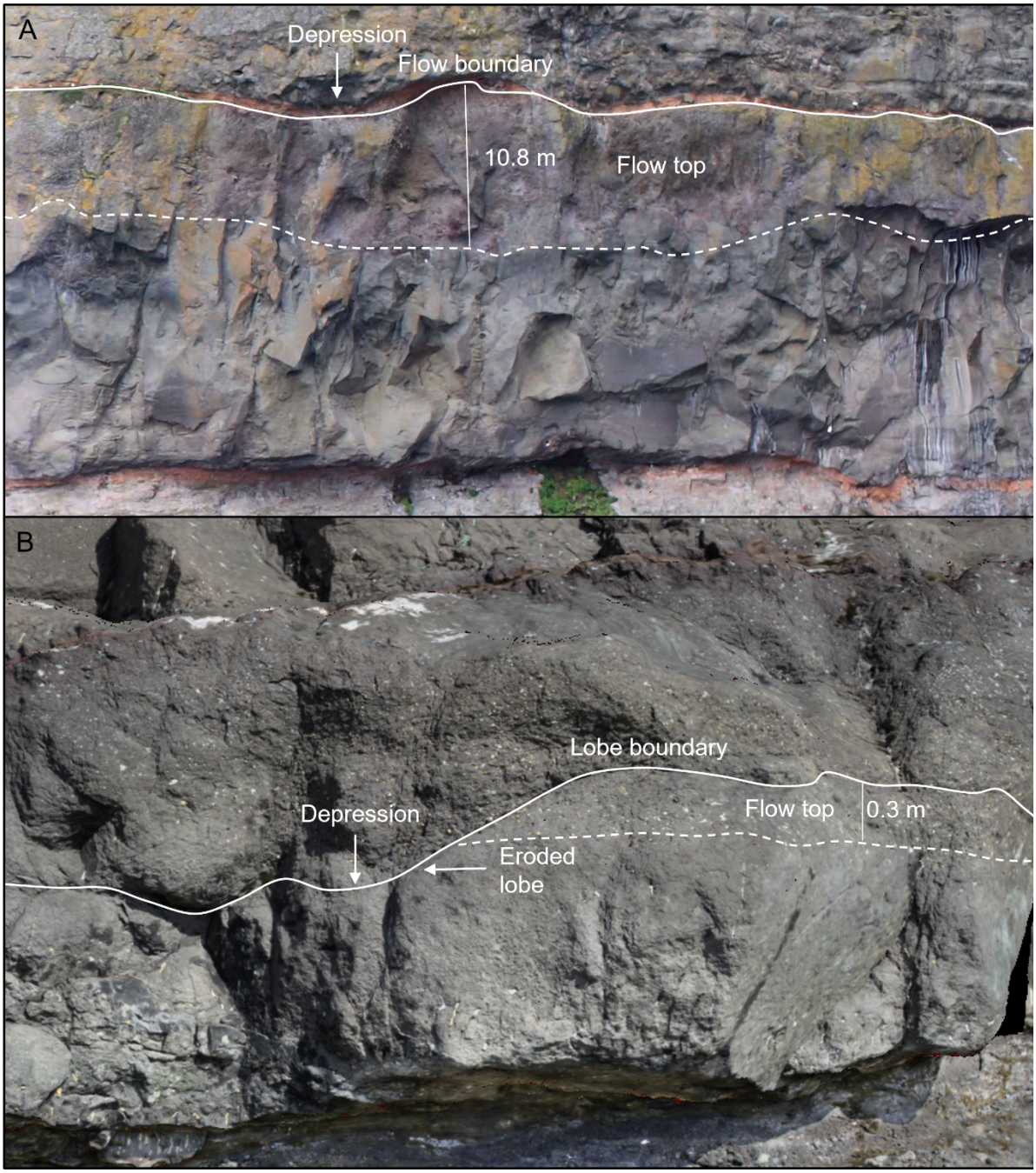

Figure 19 ***Comparison of flow top thicknesses between simple and compound flows.*** *A) Simple lava flow displaying a flow top thickness of almost 11 m with a depression seen to the left and right, reducing the flow top thickness. B) A compound flow lobe seen with a 0.3 m thick flow top. A depression into the flow lobe cuts off the entire flow top.*

The flow tops are dominated by vesicles, filled with secondary mineralization forming amygdales (Figure 20). The flow cores contain some vesicles, albeit sparse, but they too are often filled. Flow bases generally form sharp contacts to the underlying unit and show limited brecciation. Like the flow tops, the flow bases are dominated by amygdales, however, with long cylindrical structures known as pipe vesicles originating from the lower contact of the flow. These pipe vesicles are up to 100 – 150 mm long and with vesiculation increase in concentration when the flow is directly above an inter-lava

bed, especially overlying a dome structure on the upper boundary of inter-lava beds (Figure 20). The pipe structures are usually curved, showing the flow direction during emplacement. Clasts of the inter-lava bed material can be seen being incorporated into the overlying flow adjacent to these domed structures (Figure 20).

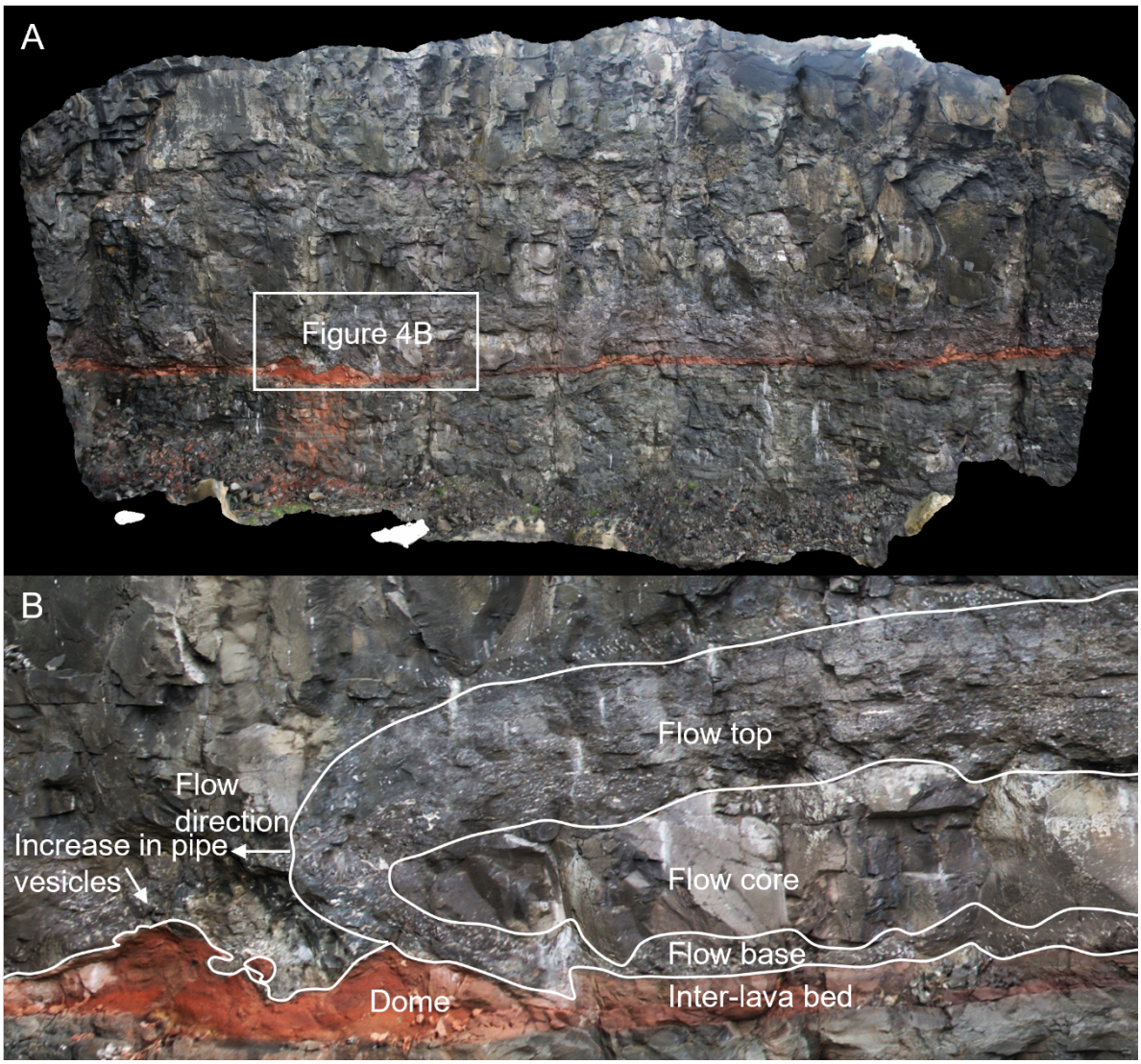

Figure 20 ***Flow architectures and relationships with underlying inter-lava beds.*** *A) Overview picture showing the location of B. B) A flow lobe within a compound lava flow. The lobe comprises a vesicular flow top, a massive core, and a flow base composed of vesicles and pipe vesicles. Adjacent to the dome within the inter-lava bed, directly before the lobe front, a clast of the inter-lava bed is incorporated into the overlying flow. Surrounding the domes, there is a greater concentration of pipe vesicles within the base of the overlying flow.*

Pore spaces within the lava flows are defined by vesicles, faults, fractures, and joints, the most widespread of which are the vesicles. As the vascularity of the flows is concentrated within the flow tops, followed by bases and then cores (Figure 20), their respective porosity is generally listed in this way. Brecciated flow crusts full of amygdales are observed; however they do not dominate like

vesicular flow tops. Faults, fractures and joints are present across the islands, though jointing is rarely seen, especially within the compound flows of the MF.

There are three categories of flows within the Faroe Islands; plagioclase phyric flows, olivine phyric flows, and aphyric flows. Within the phyric types, the phenocrysts make up at least 10 % of the flow unit. The dominating phenocrysts are plagioclase phyric types which show lath shaped plagioclase showing no particular alignment within the flows. The size of the laths range between 0.5 cm and 3 cm in length and show a heterogeneous distribution within the flows where the phenocrysts accumulate within the flow core more than the flow crust. The olivine phyric flows are rarer than the plagioclase types and show stubby phenocrysts much smaller than their plagioclase counterparts, ranging between 1-3 mm in size. The distribution of olivine phenocrysts is not determined to be heterogeneous like the plagioclase counterparts; however, due to their size and colour, they are much less obvious than plagioclase phenocrysts. The olivine phenocrysts appear fresh, especially within the cores of the flows. Aphyric flows are less common than plagioclase phyric types, but more so than olivine phyric types. Plagioclase phyric flows may be distinguished from olivine phyric and aphyric types by their colouration. Plagioclase phyric flows are pale grey, while olivine phyric and aphyric flows are brown. Consequently, it is relatively easy to interpret the basic flow types from a distance (Figure 21).

Figure 21 ***Overview of both pale and brown weathering flows****. Half of the overview is interpreted showing both pale and brown weathering flows within the EF.*

At the surface of many lava flows, ropey structures of pahoehoe are present, suggesting most of the flows represent P-type flows (Figure 22). Moving to the middle of the flows, cylindrical structures of

lava tubes showing a radial pattern of joints emanating from their centre, spanning diameters of up to 6 m and protruding out of the cliff sections more than surrounding units. These lava tubes are more commonly associated with compound flows than simple types (Figure 22). At the base of the lava flows, which overlie inter-lava beds, hollow structures can be seen extending into the flow, likely representing tree moulds. In conjunction with the moulds, an outcrop on Eysturoy's Western side ~10 km south of Eidi shows fossilized tree bark on the surface of a pahoehoe flow, directly beneath an inter-lava bed (Figure 22).

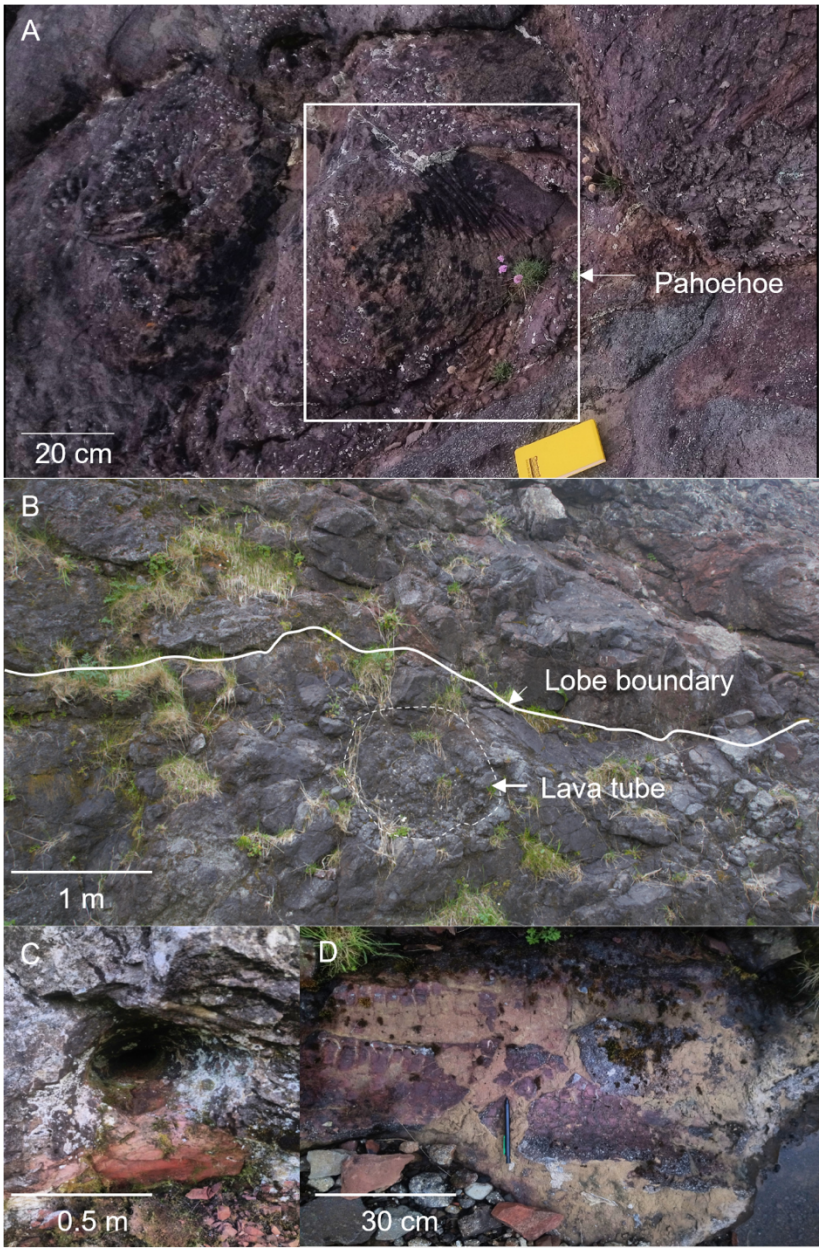

Figure 22 ***Evidence of pahoehoe structures, lava tubes, and trees.*** *A) Pahoehoe structures at Vidareidi indicative of P-type flows. B) Evidence of a lava tube within a compound flow lobe. C) A hole within a lava flow directly above an inter-lava bed is interpreted to be formed as a lava flow ran over a fallen tree. D) Fossilized tree bark on the surface of a lava flow below an inter-lava bed.*

Towards the surface of flow units overlying material can fill fractures within an underlying lava flow; this is often observed at Vidareidi and may extend up to 2.5 m and have a thickness of ~20 cm (Figure 23) likey a result of filling fractures during emplacement.

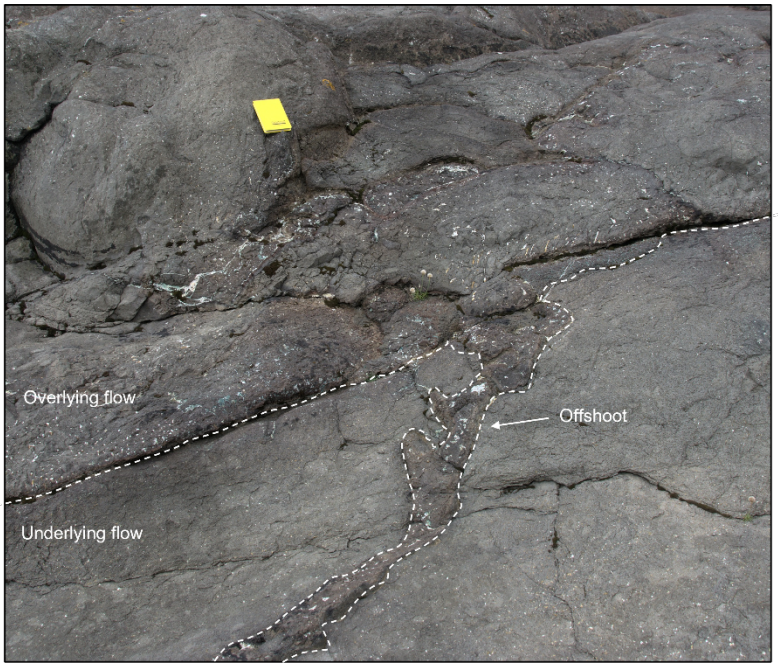

Figure 23 ***Lava flow filling a fracture of an underlying lava flow.*** *The filling originates from the overlying lava flow and contains more secondary mineralization than the surrounding lava flow. The secondary mineralization is comparable to the lava flow base of the overlying lava flow.*

Secondary mineralization is seen filling almost all the pore space throughout the Faroe Islands, with the majority of pore space provided by the vesiculation; the distribution of secondary mineralization is concentrated within lava flows flow tops (Figure 24). There is, however, some sparse vesiculation in flow cores which again are dominated by secondary mineralization. As the flow bases contain a variable amount of pore space depending on their proximity to inter-lava beds, lava flow bases may show a moderate to significant amount of filled vesiculation, including the pipe vesicles (Figure 24). Mineralized fractures and columnar joints can cross between the flow tops and bases; however, these are not common. The secondary mineralization on the Faroe Islands is dominated by cloudy white minerals displaying radiating fan-like patterns within the zeolite group.

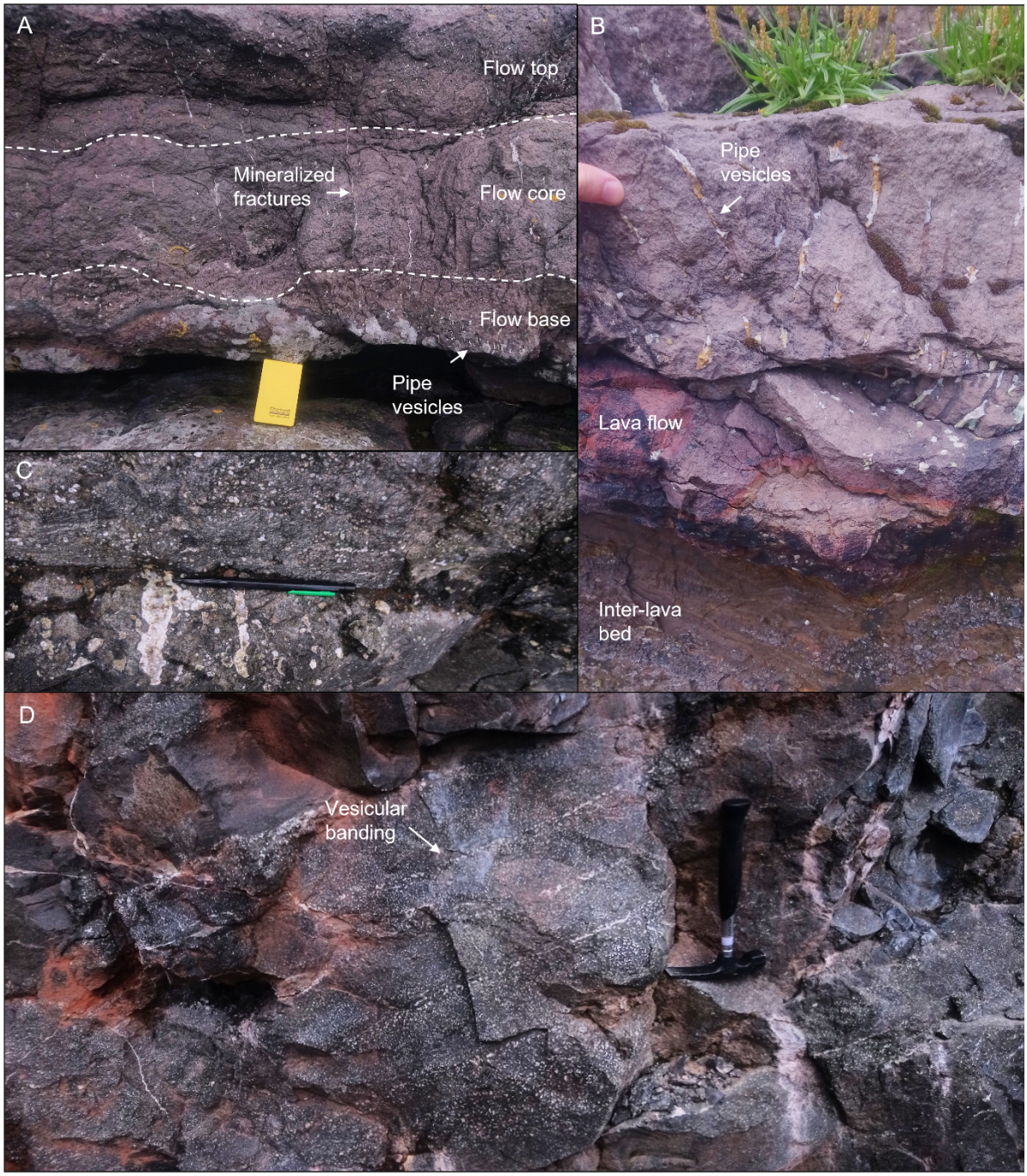

Figure 24 ***The distribution of vesicles and mineralization within lava flows.*** *A) A lava flow describing the distribution of secondary mineralization with the flow architectures. The secondary mineralization is generally confined to areas of vesiculation, and as such, the flow tops contain the most, followed by the flow bases, then cores. Some fractures can be seen crossing the core and connecting the flow tops and bases. B) A close up of a lava flow base displaying pipe vesicle structures. C) A close up of the vesiculation within lava flows, the filled vesicles show various sizes and are round to cylindrical. D) Vesicular banding within a compound flow lobe.*

4.3 Inter-lava beds

Inter-lava beds are seen across all of the Faroe Islands, separating the majority of lava flows. These beds often display poorly sorted clasts of volcanic material and are termed volcaniclastic units. These units vary significantly in coarseness from fine to conglomerates, with clasts occasionally up to 30 cm, usually angular. Inter-lava beds can be classed into two types, conglomerates (grey beds) and red beds

(Figure 25). Inter-lava beds are predominately red beds; these are sedimentary units that are fine to coarse in grain size and definitively red, whereas the grey beds are coarser, more poorly sorted, and generally softer, thus truncated in the landscape. The beds also appear similar colours to the lava flows.

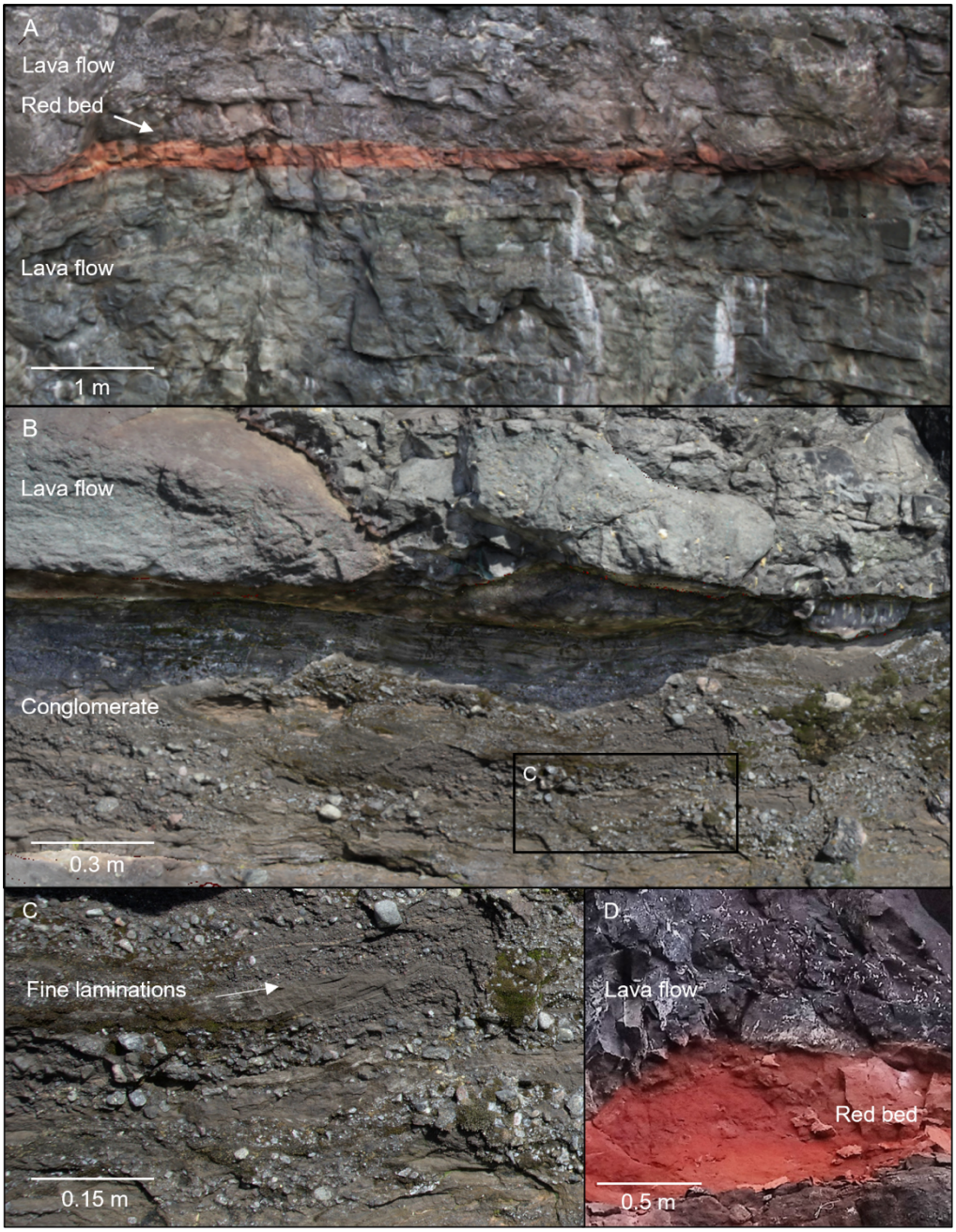

Figure 25 ***Types of inter-lava beds within the Faroe Islands.*** *A) Red bed shown to be flush with the cliff face and showing a moderately sorted grain size. B) Grey bed truncated from the overlying lava flow and showing a poorly sorted grain size.C) a close up of B showing clasts of up to*

Red inter-lava beds drape the underlying flows topography, which is primarily flat. The thickness of red beds is relatively homogeneous, even on steep slopes, with the most significant change coming

from depressions in the underlying flow unit and thus likely marking the original topography of the flow surface. At a distance, the relief of red beds' lower and upper surfaces appear parallel; however, more closely, inconsistencies can be observed where the upper horizon shows greater variability (Figure 26). This small scale variability appears to result from depressions from the emplacement of the overlying lava flow.

Variations in the bed thicknesses can be the result of depressions from erosional events such as channels. These channels cut into the underlying flow unit allowing for the sediment to accumulate, and it is noted that the accumulations of sediment within these channels represent grey beds (Figure 26). The largest channel observed spans 40 m with a depth of 25 m. The thickest sections of inter lava beds are associated with v-shaped and boxed shaped channels. Neither channel type was observed to show erosional relief with distance from the channel, suggesting an ephemeral stream deposition over a significant flow event. Grey beds are generally conglomerates showing matrix-supported clasts, indicating debris flows that preserved the rough nature of the channel walls, which are likely formed in heavy precipitation. The grey beds also show fine planar laminations indicating the settling of finer material in less turbulent times.

Figure 26 ***Thickness variations within inter-lava beds.*** *A) A large channel cut into the lava flows filled with a poorly sorted grey bed with visible clasts compared to the underlying red bed. B) A red bed showing a relatively flat base that conforms to the underlying topography and a more irregular top, though show an overall consistent thickness. Thickness variations arise from the doming of the sediment from the weight of the overlying flow.*

Laminations observed within the beds are parallel to subparallel to the underlying unit on both flat and sloped sections. The inter-lava beds show limited sedimentary features such as cross-bedding; however, the occasional sorting pattern can be observed; for example, within the Argir beds where a coarsening upward pattern is present.

4.4 Connectivity and compartmentalization

Vertical and lateral connectivity of units was observed throughout the field, especially on the larger scale, such as cliff sections like Svinoy (Figure 27). One of the most common forms is merging inter-lava bed units, where a flow separating two inter-lava beds wedges out, forming connectivity between two successive beds. This merging of inter-lava beds causes inter-lava bed distribution variations between areas. Furthermore, the thickness of the merged inter-lava bed approximately totals the combined thickness of the two joining beds. On the Svinoy cliff section, there is a discrepancy of inter-lava beds between the SE and NW, with seven beds observed within the SE compared to two in the NW.

Figure 27 ***The merging of successive inter-lava beds.*** *When a lava flow thins out, which is generally towards the NE, two successive inter-lava beds join and form inter-lava beds with an approximate thickness of the sum of the two beds.*

Other forms of connectivity between the inter-lava beds and intra-lava units can be from the sediment-filled channels (Figure 26), which may be large enough to join several inter-lava beds and flows. Other channels arise between two flow units that terminate towards one another, forming a box-like feature for the sediment or lava to fill (Figure 28). Thus channels are either v-shaped or box-shaped.

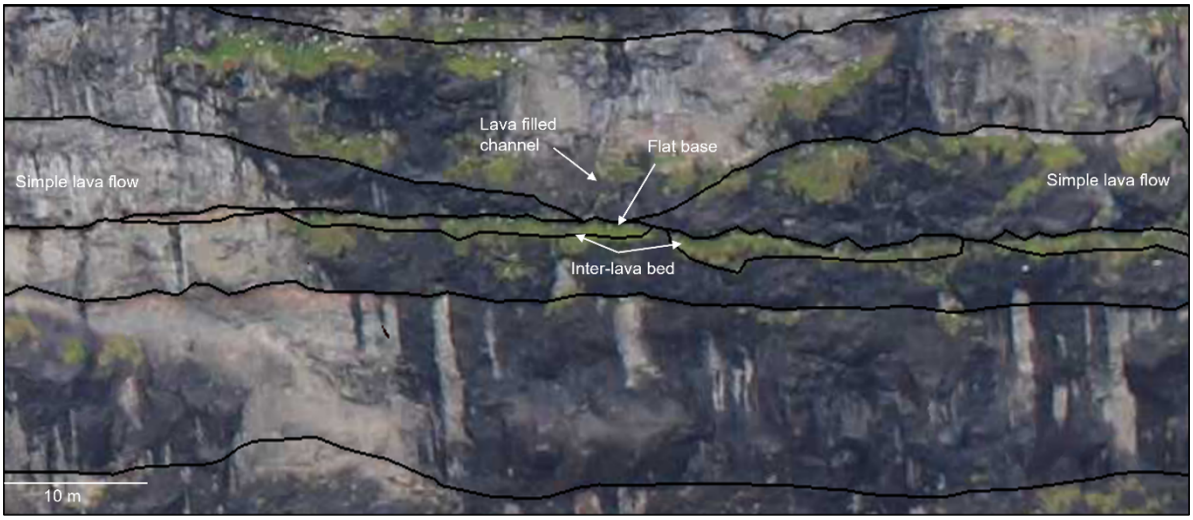

Figure 28 ***Box channel.*** *Two flows facing one another terminate, leaving a flat bottomed channel which in this case is filled by a lava flow.*

Besides connectivity, inter-lava beds show lateral compartmentalization in the form of dykes, faults, lava tubes, and lava-filled channels. Dykes up to ~6 m wide cross-cut the volcanic succession in multiple areas; however, the overall occurrence of the dykes is low. Lava tubes are more common within compound flows, rarely cross-cutting more than two inter-lava beds.

Significant compartmentalization comes in lava-filled channels that truncate the interbeds and intra-lava flows units, acting as impermeable barriers and occasionally cross-cutting multiple successive interbeds (Figure 29). This feature was often observed within the large cliff sections and is more common than sediment filling channels. In addition, erosion can compartmentalise or reduce both flow tops and inter-lava beds. The erosion removes some or all of the flow top within lava flows, leaving the core and base, whereas the softer and thinner inter-lava beds thin out completely (Figure 29).

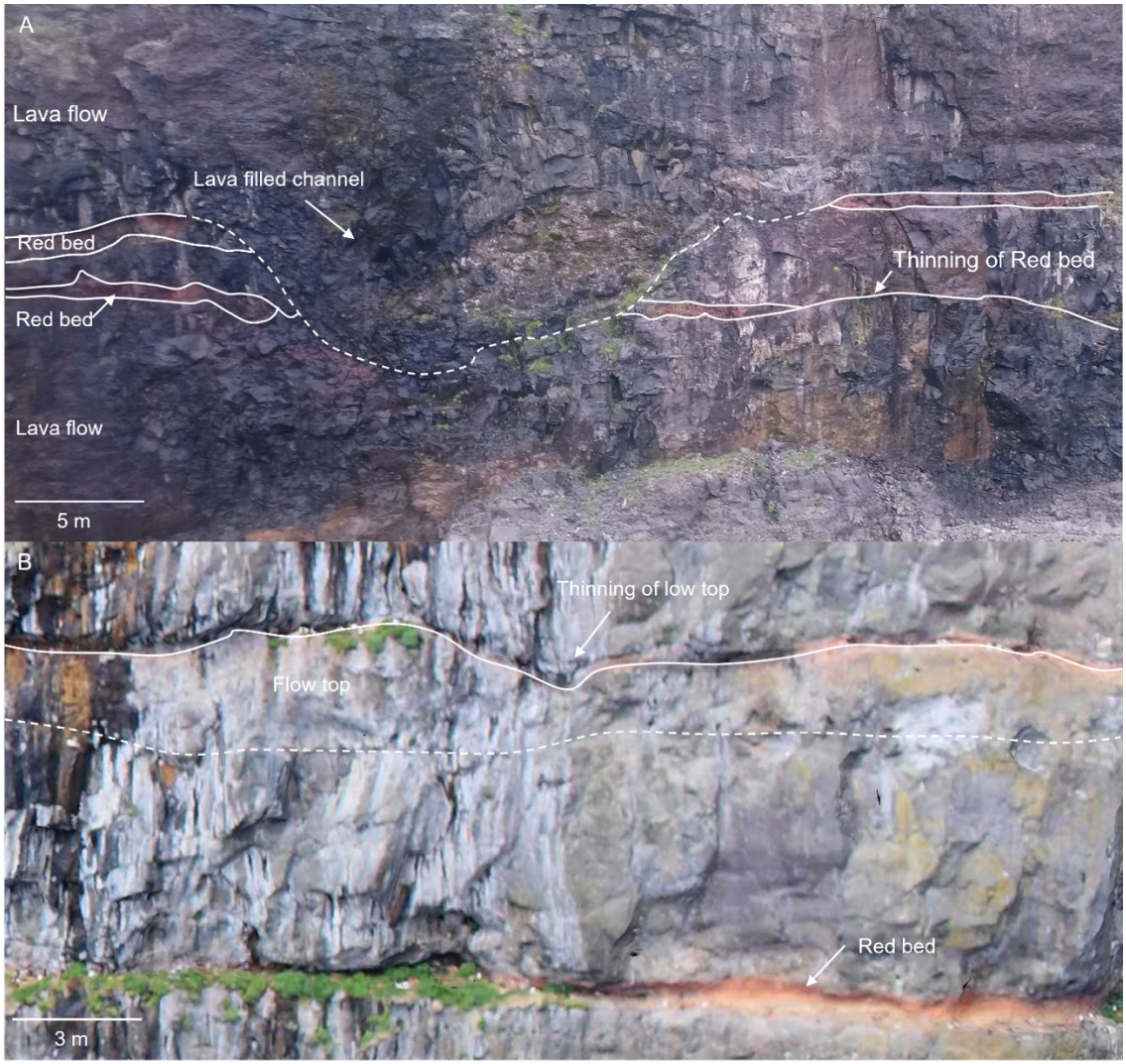

Figure 29 ***Erosional features.*** *A) A sizeable lava-filled channel cutting through multiple lava flows and red beds. There is also the complete thinning of an inter-lava bed on the middle right of the figure. B) Thinning of the flow top of a lava flow.*

The final observed feature contributing to compartmentalization is faulting (Figure 30). Faults within the Faroe Islands are commonly seen where their displacement juxtaposes inter-lava beds and lava flow units forming seals. The Svinoy cliff expresses a NE-SW striking fault with an angle of ~30° and a displacement of just less than 3 m, juxtaposing the interbeds to lava flow units. Other forms of faulting observed include significant conjugate normal faults cross-cutting entire cliff sections, normal faults, and asymmetric faulting (Figure 30). However, the asymmetric faulting was only seen at Vidareidi, and the displacement of the fault was not evident. The asymmetric fracture pattern decreases with distance from the fault, displaying an extensive array of filled and connected fractures on the hanging wall compared to the relatively few fractures on the foot wall. Adjacent to the fractures, there appears to be a paler zone representing some form of alteration. The fractures are filled with zeolites, the same material seen filling vesiculation throughout the Faroe Islands. The filled porosity generated from the faulting could suggest the ability for fluids to pass through the fault connecting successive units and allowing fluids to migrate laterally through the fracture patterns produced.

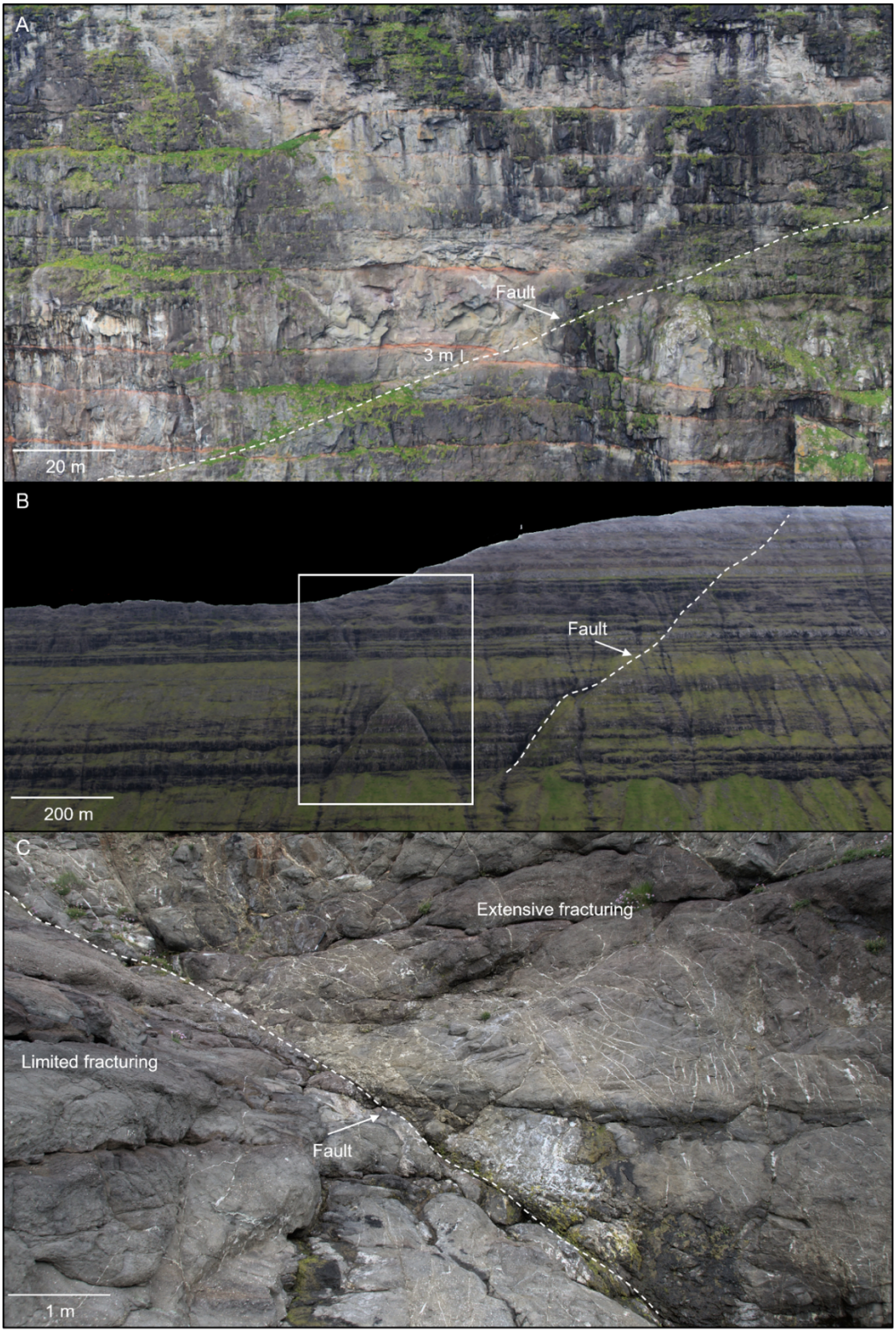

Figure 30 ***Faulting types within the Faroe Islands.*** *A) A reverse fault with a 3 m displacement within the Svinoy sea cliff. B) Conjugate fault as indicated within the square and adjacent to a large normal fault. C) An asymmetric fault with extensive fracturing on one side and limited fracturing to the other. Due to limited common features on either side of the fault, a displacement was not calculated.*

4.5 Lava flow and inter-lava bed extents and thicknesses

The VOM's were used to understand the vertical and horizontal extents of lava flows and inter-lava beds. The Svinoy sea cliff VOM is the most useful for calculating these extents due to its superior resolution and exposure, although it was possible to carry this out on the Vidoy west VOM.

The Svnoy sea cliff VOM shows 45 lava flows, 12 compound and 33 simple flow types. The average distance of these flow types is 2168.5 m for compound types and 1686.4 m for simple types. Notably, many flow distances for both flow types were more significant than the visible cliff section. Furthermore, flow thicknesses were greater for compound flows, whereas simple flow types were much thinner. The Svinoy sea cliff shows a maximum of 7 inter-lava beds between lava flow packages; however, this number is likely larger as it can be challenging to identify beds < 1 m in thickness. Furthermore, the continuity of beds is likely more continuous than interpreted on the model due to this resolution problem. However, compartmentalization of these inter-lava beds forms from in lava-filled channels; this may also be partly responsible for some of the pinching observed within the inter-lava beds. Due to the resolution issues with the inter-lava beds, their extents were not quantified. Vidoy west is of a lower resolution and exposure than the Svinoy sea cliff and was thus more difficult to track the flows, although some information was gathered. There are 23 simple flows, and 8 compound flows within the VOM, with the simple flows showing extents ranging from 180 m to 5809.8 m (the length of the VOM). Compound flows tended to be expressed across the entire VOM's extent with few exceptions. The values are also displayed in Table 5.

Table 5 ***Lava flow and inter-lava bed extents within the Svinoy sea cliff***

Extents of lava flows at Svinoy Sea cliff				
Type	Number	Average length	Maximum length (m)	Minimum length (m)
Simple	*33*	*1686.4*	*>4663*	*125.5*
Compound	*12*	*2168.5*	*>4618*	*330.2*
Extents of lava flows at Vidoy West				
Simple	*23*	*4460*	*>5809.8*	*180.4*
Compound	*8*	*>5809.8*	*>5809.8*	*3078.5*

Stratigraphic logs were taken of both the Svinoy sea cliff and Vidoy VOM's to quantify the compound and simple lava flows and thicknesses across the VOM's (Figure 31 and Figure 32). The extents and thickness of inter-lava beds within the Svinoy sea cliff were also measured, though not within the Vidoy VOM due to low resolution. The logs are named according to their position with each log interpreted with the quantity and average thickness of compound and simple lava flows and inter-lava beds (Table 6)

Table 6 ***Statistics on lava flows and inter-lava beds from the VOM's***

Thicknesses of lava flows at Svinoy sea cliff		
	Quantity	**Average thickness (m)**
West Log		
Compound flows	7	18.3
Simple flows	16	14.5
Inter-lava beds	5	0.9
Mid Log		
Compound flows	6	19.7
Simple flows	13	14.2
Inter-lava beds	3	1.1
East Log		
Compound flows	6	22.9
Simple flows	14	12.1
Inter-lava beds	2	2.3
Thicknesses of the lava flows at Vidoy west		
North log		
Compound flows	12	40.0
Simple flows	26	19.9
South log		
Compound flows	8	52.5
Simple flows	24	13.5

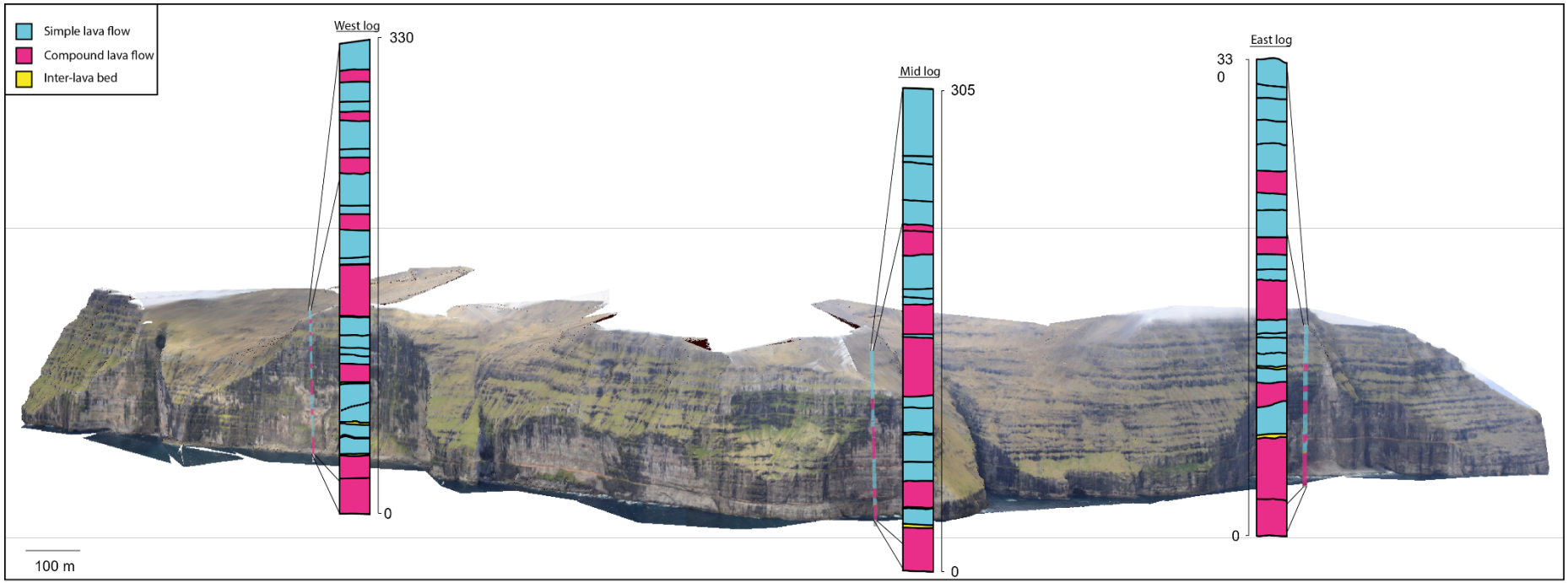

Figure 31 ***Overview of the Svinoy sea cliff VOM displaying log profiles.*** *All logs show an increasing proportion of simple lava flows with stratigraphic height.*

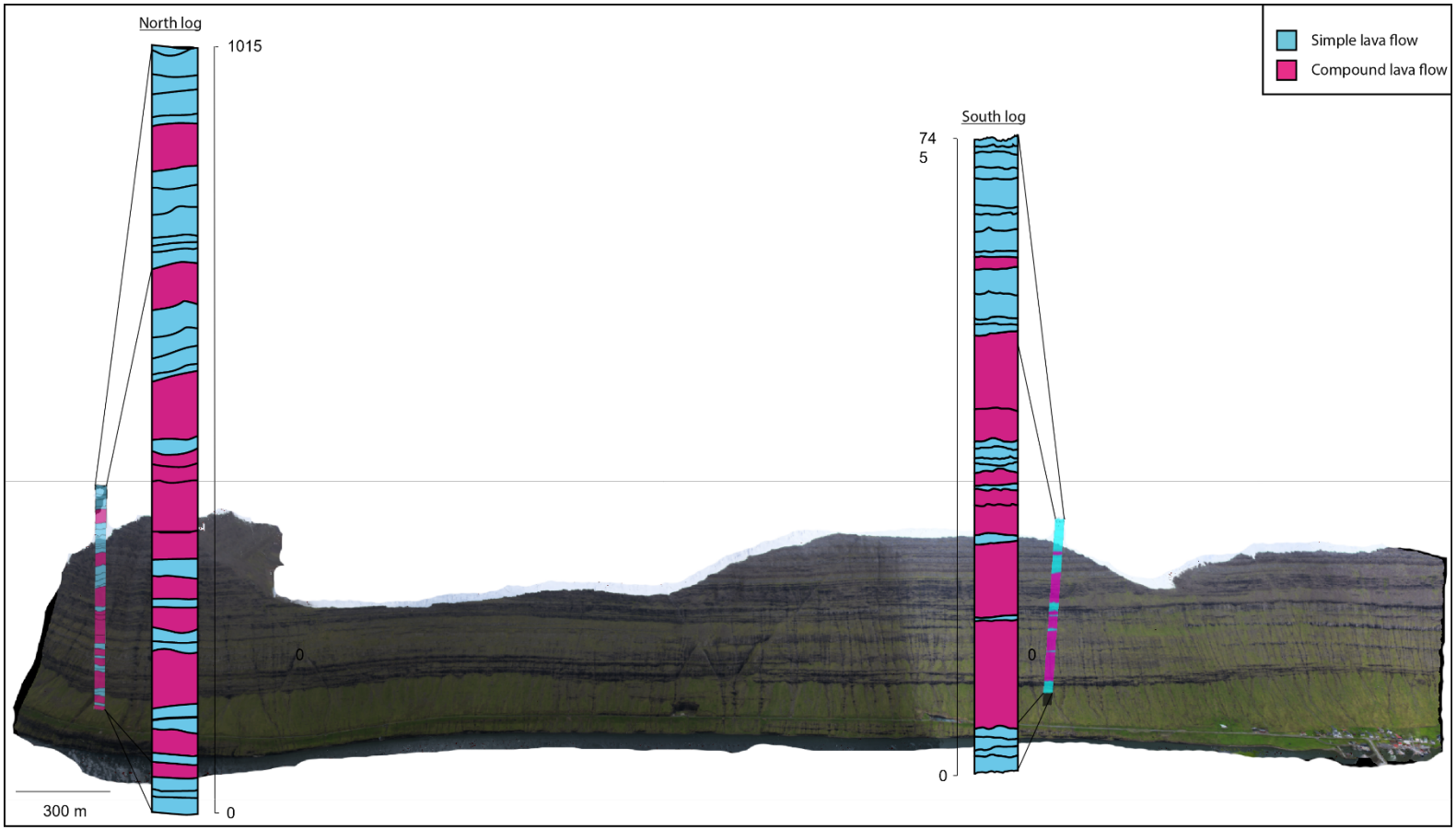

Figure 32 ***Overview of the Vidoy VOM displaying log profiles.*** *Logs show the increasing proportion of simple lava flows with stratigraphic height. Note the height discrepancies between the North and South logs, the former being ~250 m higher.*

Table 6 shows the thickest units to be defined by the compound flows, although simple flows are more numerous in all logs across both VOM's. The quantity of both compound and simple flows stay relatively consistent across the extent of the VOM's; whereas the inter-lava beds decrease towards the Eastern side of the Svinoy sea cliff; supplementary to this, the inter-lava beds successively thicken towards the East of Svinoy. The Vidoy VOM shows the southern portion to be predominately composed of compound flows, providing 56% by the surface area of the log; this reduces to 47% in the North, arising from the thickness of the compound flows in the south being greater than the North. Thicknesses within the Svinoy VOM are more consistent, and thus, this discrepancy is not observed. Both models show an increase of simple lava flows towards the top of the VOM's though is more exaggerated at Vidoy.

4.6 Sample set

This section describes the samples used within this study. The data is presented: sample descriptions of common features seen throughout the Faroe Islands, mineralogy and modal abundances, chemical variability, porosity and permeability distributions, and dissolution rates. The majority of samples were taken from cores apart from samples for CT analysis and dissolution testing.

4.6.1 Sample Descriptions

An array of secondary minerals fill the pore space within rocks from the Faroe Islands. The most common type are zeolite minerals, present within most rock samples; others include chalcedony and an assortment of clay minerals (Table 7 and Figure 33).

Table 7 ***Samples showing characteristic secondary mineralization***

Sample	Sample type	Porosity	Phenocrysts	Alteration	Reason
GM-12	*Lava flow top*	*high*	*Plagioclase phyric*	*No*	*A soft black mineral filling porosity.*
GM-14	*Lava flow top*	*High*	*Fine to medium plagioclase phyric*	*Soft teal mineral*	*What represents the green mineral.*
GM-18	*Lava flow top*	*High*	*Medium plagioclase phyric*	*light brown to orange mineral*	*What represents the brown to orange mineral.*
GM-26	*Lava flow top*	*High*	*Medium plagioclase phyric*	*soft cloudy grey mineral and minor amounts of the teal mineral often coats the vesicles' rims. Glassy clear and cloudy white minerals are also abundant within the sample.*	*Abundance secondary mineralization.*
T2M-02	*Lava flow top*	*High*	*Coarse plagioclase phyric*	*a clear glassy mineral, cloudy green mineral, and a cloudy white mineral.*	*The cloudy white mineral often coats the rims of some of the vesicles while the cloudy green mineral fills the core of the vesicle.*
T2M-03	*Lava flow top*	*High*	*Aphyric*	*Cloudy grey mineral*	*The groundmass of the sample shows significant reddened alteration and fractures running through the centre of the sample.*
T2M-04	*Lava flow core*	*Low*	*Aphyric*	*a soft cloudy white mineral and a soft black mineral*	*The pore space is also shared by both types of secondary minerals splitting the vesicle and sharing a sharp straight contact.*

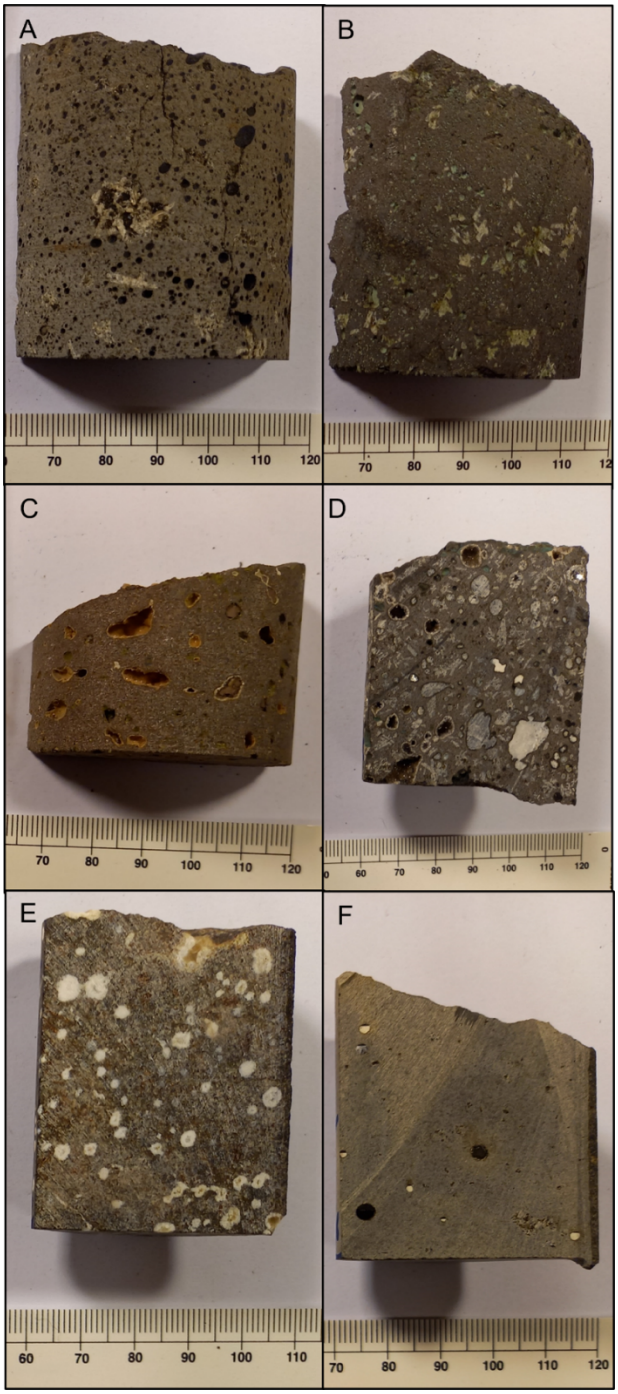

Figure 33 ***Samples showing the varying secondary mineralization throughout the Faroe Islands****. A) GM-12 is a plagioclase phyric flow top with significant vesiculation, predominantly filled with a soft black mineral. B) GM-14 is a fine to medium plagioclase phyric flow with plagioclase phenocrysts forming star shape clusters. The samples' abundant pore space (~ 1 mm) is filled with a soft teal coloured mineral. C) GM-18 represents a medium plagioclase phyric flow containing large vesicles (~ 3 mm), which shows rims of a distinctive light brown to orange mineral; however, less numerous teal and glassy white minerals are also present, filling some of the smaller (< 1 mm) vesicles. D) GM-26 is a medium plagioclase phyric flow containing significant pore space filled with abundant secondary mineralization. The secondary mineralization shows a soft cloudy grey mineral and minor amounts of the teal mineral, which often coats the rims of the vesicles. Glassy clear and cloudy white minerals are also abundant within the sample. E) T2M-02 is from a coarse plagioclase phyric flow, although no plagioclase phenocrysts are seen in this sample. The sample shows three different minerals filling pore space, a transparent glassy mineral, cloudy green mineral, and a cloudy white mineral. The cloudy white mineral often coats the rims of some of the vesicles, while the cloudy green mineral fills the core of the vesicle. F) T2M-04 is an aphyric flow core displaying sparse vesiculation; however, the present vesiculation is ~ 2 mm in size and is both open and filled. The vesicles are filled with either a soft cloudy white mineral or a soft black mineral. The pore space is also shared by both types of secondary minerals splitting the vesicle and sharing a sharp straight contact.*

The presence of alteration zones can be seen across a number of samples (Table 8, Figure 34). These alteration zones extend from areas of filled porosity into the reactive rock. The distance the alteration extends is limited to between 0.5 - 3.0 cm from the boundary and is seen as a darker zone than the surrounding material.

Table 8 ***Samples containing altered fracture zones***

Sample	Sample type	Porosity	Phenocrysts	Alteration	Reason
GM-21	*Lava flow core*	*Low*	*Olivine phyric*	*Soft teal mineral*	*distinctive alteration halo adjacent to a network of fine fractures cross-cutting the middle of the sample. The dark alteration zone extends ~ 5 mm from the mineralized fractures. Filling the fractures is a cloudy white mineral adjacent to the fracture wall, with a cloudy green mineral filling the centre of the fracture.*
GM-22	*Lava flow core/base transition*	*Low*	*Aphyric*	*light brown to orange mineral*	*A fracture towards the top of the sample and a thicker fracture at the samples base. The fractures show a green platy mineral in their centre and a cloudy white mineral at the fracture wall. An area of a blue hue can be seen radiate from the upper fracture.*
GNM-02	*Lava flow top*	*Low*	*Aphyric*	*cloudy white and clear glassy mineral with pale green minerals along the wall of the fracture*	*abundant cross-cutting alteration patterns. There appear to be fine fractures that join these darker bands.*
T2M-08	*Lava flow core*	*Low*	*Fine plagioclase phyric*	*white and glassy though some cloudy pink minerals are also present*	*a series of veins at the base of the sample. The minerals filling the fractures are white and glassy though some cloudy pink minerals are also present. Above the primary fracture, smaller offshoot fractures propagate into the basalt filled with a clear glassy mineral. The layered veins also show connectivity by fine fractures.*

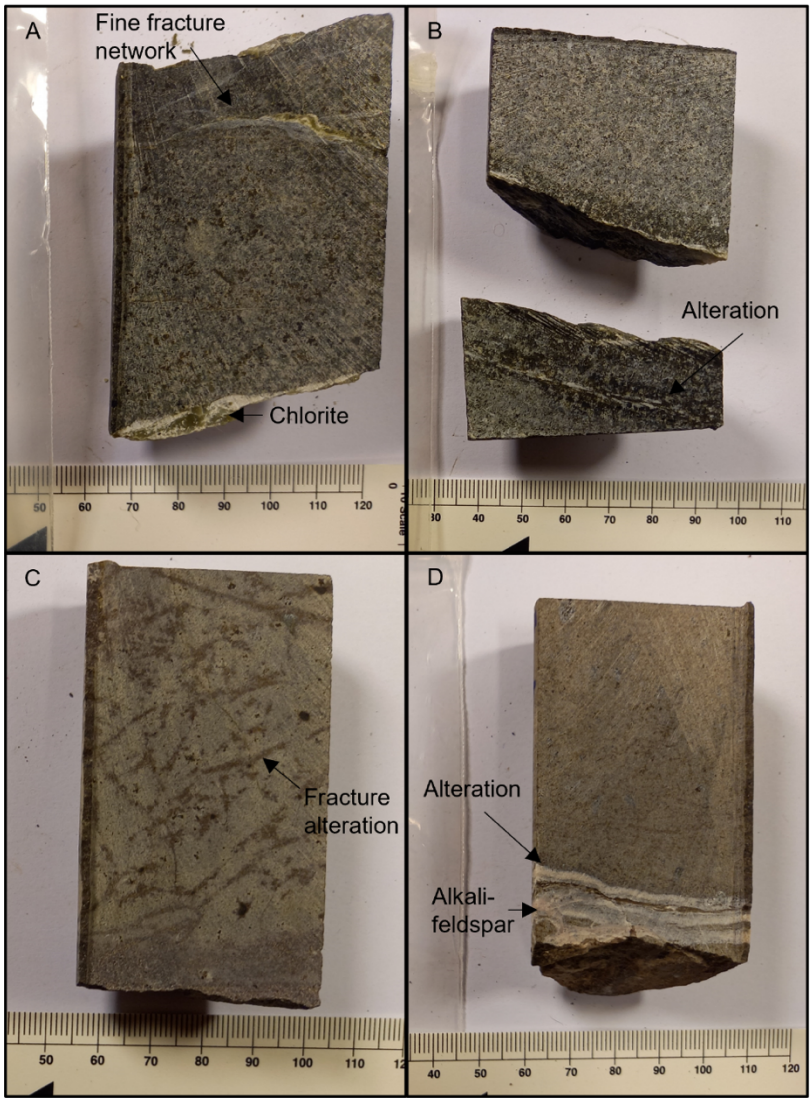

Figure 34 ***Zones of alteration.*** *A) GM-22 is an aphyric flow core-base transition displaying two areas of fractures—a fracture towards the top of the sample and a thicker fracture at the base of the sample. The fractures show a green platy mineral in their centre and a cloudy white mineral at the fracture wall. An area of a blue hue can be seen radiating from the upper fracture. B) GM-21 represents an olivine phyric flow core containing a distinctive alteration halo adjacent to a network of fine fractures cross-cutting the middle of the sample. The dark alteration zone extends ~ 5 mm from the mineralized fractures. Filling the fractures is a cloudy white mineral adjacent to the fracture wall, with a cloudy green mineral filling the centre of the fracture. C) GNM-02 is an aphyric flow showing abundant cross-cutting alteration patterns. There appear to be fine fractures that join these darker bands. Two fractures within the sample are filled with a cloudy white and clear glassy mineral with pale green minerals along the fracture wall. The sample base shows a clastic band with an offshoot into the wall rock composed of fine dark grains. D) T2M-08 is a fine plagioclase flow core showing a series of veins at the sample base. The minerals filling the fractures are white and glassy though some cloudy pink minerals are also present. Above the main fracture, smaller offshoot fractures propagate into the basalt filled with a clear glassy mineral. The layered veins also show connectivity by fine fractures.*

Three samples were analyzed by CT analysis (Table 9, Figure 35). These samples include a flow top, core, and base, with varying degrees of secondary mineralization and alteration. The flow top sample shows significant reddening to its groundmass in comparison to the other samples. The sample also shws the largest vesicles upto ~4mm in diameter however the flow base sample contains the greatest number of vesicles. The vesicles are larger than the upper half of the sample and filled with a different

secondary mineralization. The flow core sample appears to show very limited pore space and a homogeneous groundmass.

Table 9 ***Characterization of the CT scan samples***

Sample	Sample type	Porosity	Phenocrysts	Alteraltion	Reason	Other
F20-10	*Lava flow top*	*High*	*Aphyric*	*Extensive*	*Represents a flow top*	*All porosity is filled with two minerals, an inner core with a radial pattern and a glassy clear mineral around the rim of the pore*
F20-11	*Lava flow core*	*Low*	*Aphyric*	*Little*	*Represents a flow core*	*Needle-like minerals throughout groundmass*
F20-14	*Lava flow base*	*High*	*Aphyric*	*Filled with a soft white mineral and a soft black mineral*	*Represents a flow base*	*a cloudy white mineral and a black mineral split the pore and separated with a perfectly horizontal and sharp boundary.*

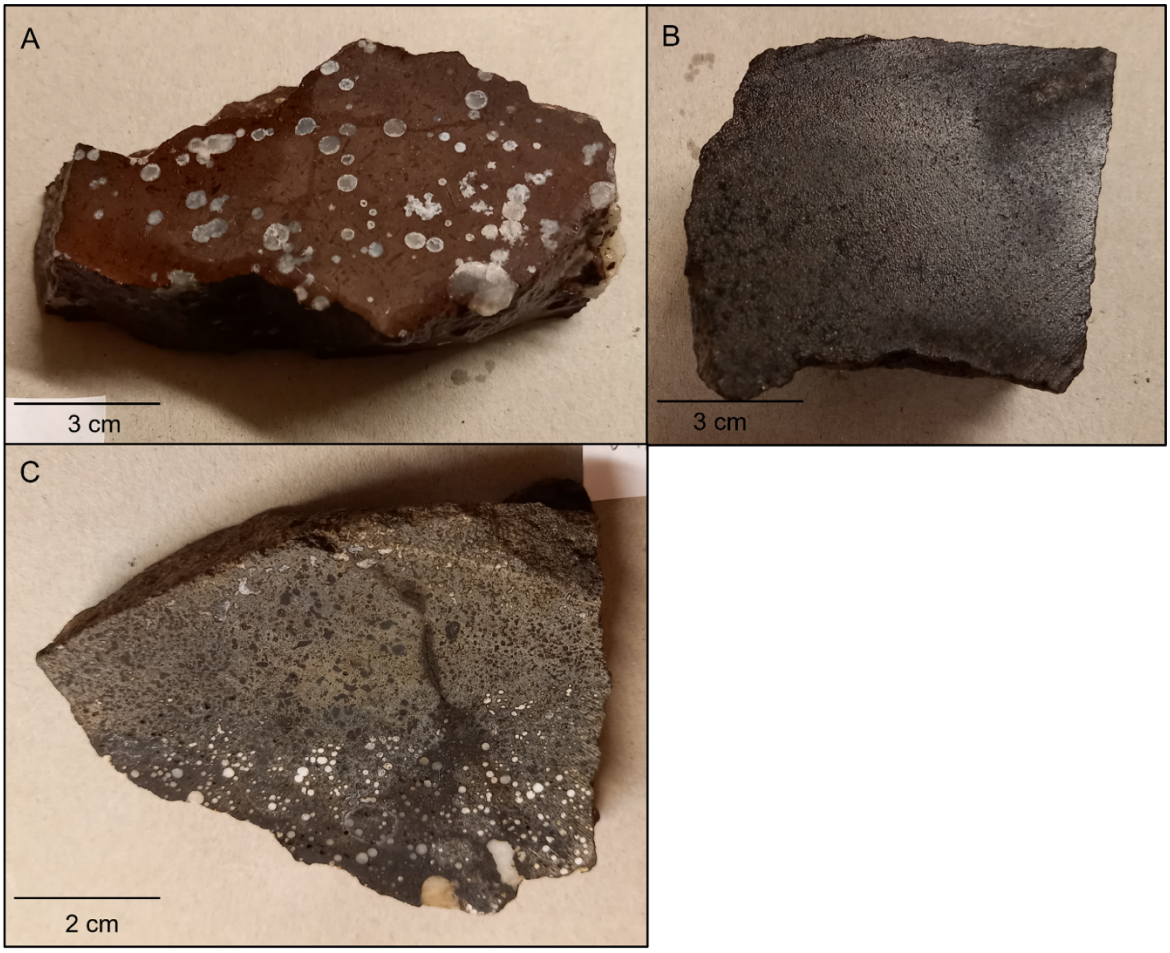

Figure 35 ***Samples for the CT analysis****. A) F20-10 a flow top showing a reddened groundmass and extensively filled vesicles. Fine fractures can be seen running through the groundmass, highlighted by their slightly darker appearance. B) F20-11, a flow core showing limited vesiculation and secondary mineralization. C) a flow base with two zones, an area represented by a soft white mineral filling the vesicles, which is the base of the sample in contact with an inter-lava bed and an upper area represented by a soft black mineral filling vesiculation. The sample base shows two pipe vesicles protruding into the sample, and the surrounding vesicles are larger than the filled vesicles within the black mineralization zone.*

Five samples were used for the dissolution experiments; these include four lava flows and one inter-lava bed (Table 10 and Figure 36). The samples for the lava flows were taken from two different flows a plagioclase phyric and aphyric flow, with a flow top and core taken from each. Thus GRM-01 and GRM-02 are related and represent the flow top and core respectively of the plagioclase phyric flow, with GRM-03 and GRM-04 represent the flow top and core respectively of the aphyric flow. The inter-lava bed represents a red bed from near the top of the Argir bed.

Table 10 ***Classification of reactivity samples***

Sample	Sample type	Porosity	Phenocrysts	Alteration	Other	Reason
GRM-01	*Lava flow core*	*low*	*Plagioclase phyric*	*No*	*Limited alteration and vesiclation*	*Sample representing a plagioclase phyric flow core from flow 10.*
GRM-02	*Lava flow top*	*High*	*Plagioclase phyric*	*Extensive*	*Very friable*	*Sample representing a plagioclase phyric flow top from flow 10.*
GRM-03	*Lava flow core*	*Low*	*Aphyric*	*No*	*Some large vesicles (up to 2 cm) filled with both zeolites and a soft black mineral split the vesicle and separated with a perfectly horizontal and sharp boundary.*	*Sample representing an aphric flow core of flow 2.*
GRM-04	*Lava flow top*	*High*	*Aphyric*	*Yes*	*Sample is somewhat friable, although less than GRM-02.*	*Sample representing an aphyric flow top of flow 2.*
GRM-05	*Sediment*	*High*	*N/A*	*Red coloured*	*Moderately to poorly sorted material with angular black clasts present*	*Sample of the Argir beds taken above flow 2.*

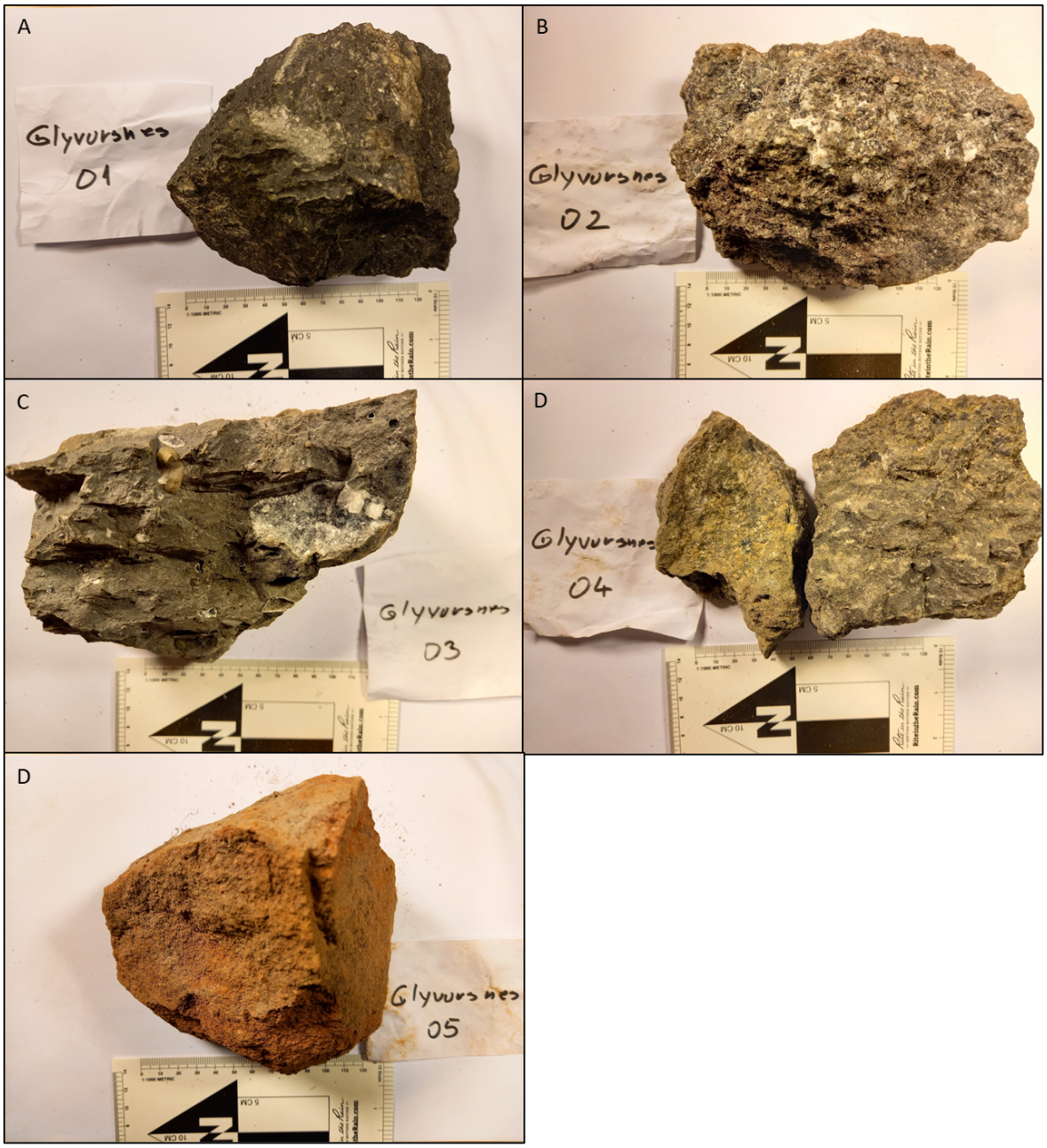

Figure 36 ***Sample for reactivity analysis.*** *A) GRM-01 represents the simple plagioclase phyric lava flow core displaying little alteration, vesiculation, and secondary mineralization. B) GRM-02 is of the same flow as A and represents a simple plagioclase phyric lava flow top displaying extensive alteration, contributing to the sample being quite friable. The sample shows extensive secondary mineralization filling abundant vesiculation. C) GRM-03 represents an aphyric flow core with rare pore space up to 25 mm in diameter filled with two minerals, a cloudy white mineral and a black mineral, splitting the vesicles and separated with a perfectly horizontal and sharp boundary. The relative amounts shown within each pore differ widely, with some pores only containing either the white or black mineral. D) GRM-04 is of the same flow as C) but represents the flow top with secondary mineralization present and is quite altered but not as extensive as B. E) GRM-05 is an inter-lava bed taken approximately 1 m from the top of the Argir beds, which is located above lava flow 2. The sample is red and moderately to poorly sorted, showing some distinctive black clasts.*

4.6.2 Geochemistry of reactivity samples

The reactivity samples were analyzed for both major and trace elements; the results of the analyses can be found in Table 11. The variability of SiO_2 between the samples ranged between 44.2 and 48.3%, with the largest variability observed between K_2O, Na_2O_3, P_2O_5, and TiO_2. The sum of the divalent cation oxide concentrations, CaO, MgO, and FeO, within the samples, ranges between 28.5% and

31.8%, highest in GRM-03 and lowest in GRM-05. The LOI shows variability between the samples, with GRM-02 expressing the greatest at 11.6% and GRM-03 the least at 2.6%.

Table 11 ***XRF major element raw data***

Sample	SiO2	Al2O3	Fe2O3	MnO	MgO	CaO	Na2O	K2O	TiO2	P2O5	LOI
GRM-01	*48.25*	*15.49*	*13.13*	*0.19*	*6.27*	*12.17*	*2.32*	*0.25*	*1.76*	*0.15*	*1.28*
GRM-02	*49.82*	*17.56*	*11.34*	*0.16*	*4.81*	*12.36*	*2.11*	*0.23*	*1.50*	*0.11*	*11.6*
GRM-03	*48.48*	*13.95*	*14.97*	*0.20*	*6.30*	*10.54*	*2.70*	*0.16*	*2.46*	*0.24*	*2.6*
GRM-04	*47.98*	*14.23*	*14.98*	*0.20*	*6.53*	*9.64*	*3.60*	*0.12*	*2.48*	*0.24*	*4.08*
GRM-05	*50.42*	*14.77*	*13.92*	*0.19*	*6.04*	*9.39*	*1.60*	*0.95*	*2.55*	*0.18*	*5.73*

Oxides are recalculated to 100 wt%

Plotting the dissolution samples of a TAS rock classification diagram, all the rocks plot within the basalt field (Figure 37).

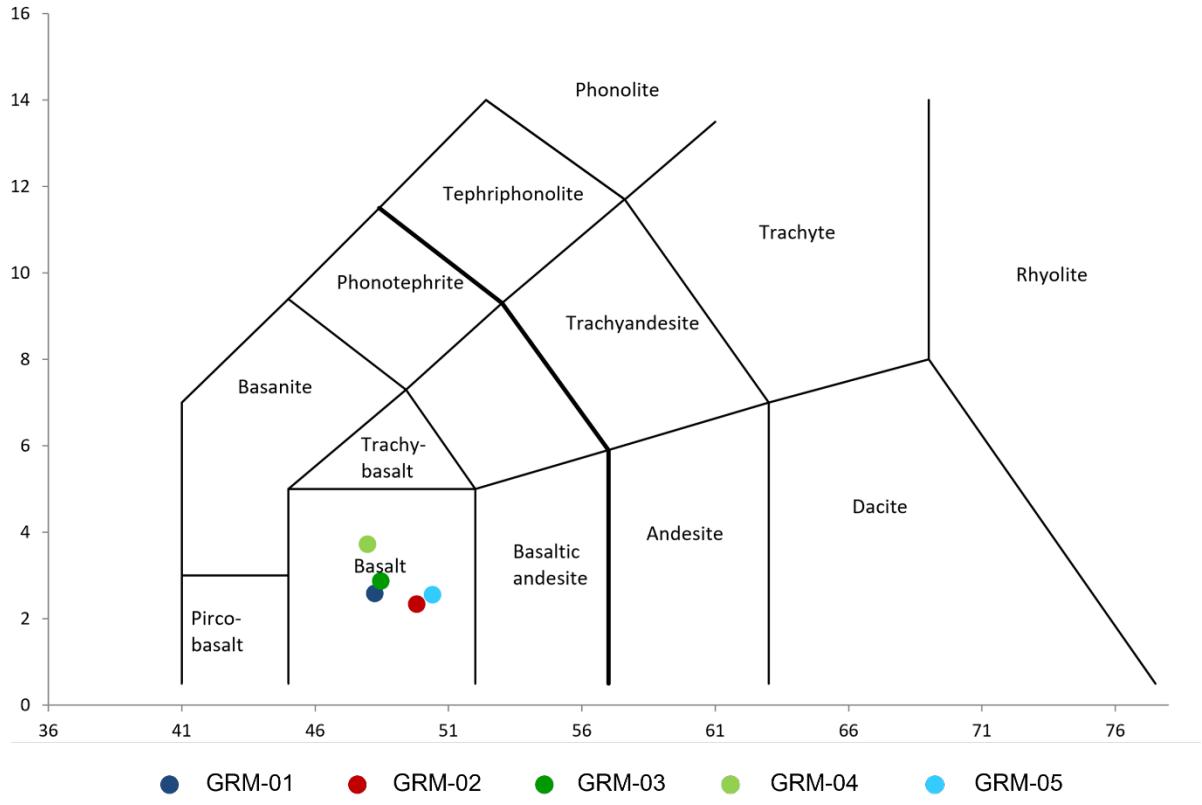

Figure 37 ***TAS classification diagram.*** *The dissolution samples plot within the basalt field. Using Le Maitre et al. (2002).*

The elemental ratios concerning Si are shown in Table 12 and Figure 38. The data shows large differences in Al/Si, Fe/Si, and Mg/Si ratios between GRM-01 and GRM-02, both genetically related samples; this is not the case for the two other genetically related Samples GRM-03 and GRM-04 which share very similar ratios across the board.

Table 12 ***Cation ratios with respect to Si for the reactivity samples***

	Al/Si	Fe/Si	Mg/Si	Ca/Si	Na/Si	K/Si
GRM-01	*0.247*	*0.313*	*0.168*	*0.386*	*0.038*	*0.005*
GRM-02	*0.271*	*0.262*	*0.125*	*0.379*	*0.034*	*0.004*
GRM-03	*0.221*	*0.355*	*0.168*	*0.332*	*0.044*	*0.003*
GRM-04	*0.228*	*0.359*	*0.176*	*0.307*	*0.059*	*0.002*
GRM-05	*0.225*	*0.318*	*0.154*	*0.285*	*0.025*	*0.017*

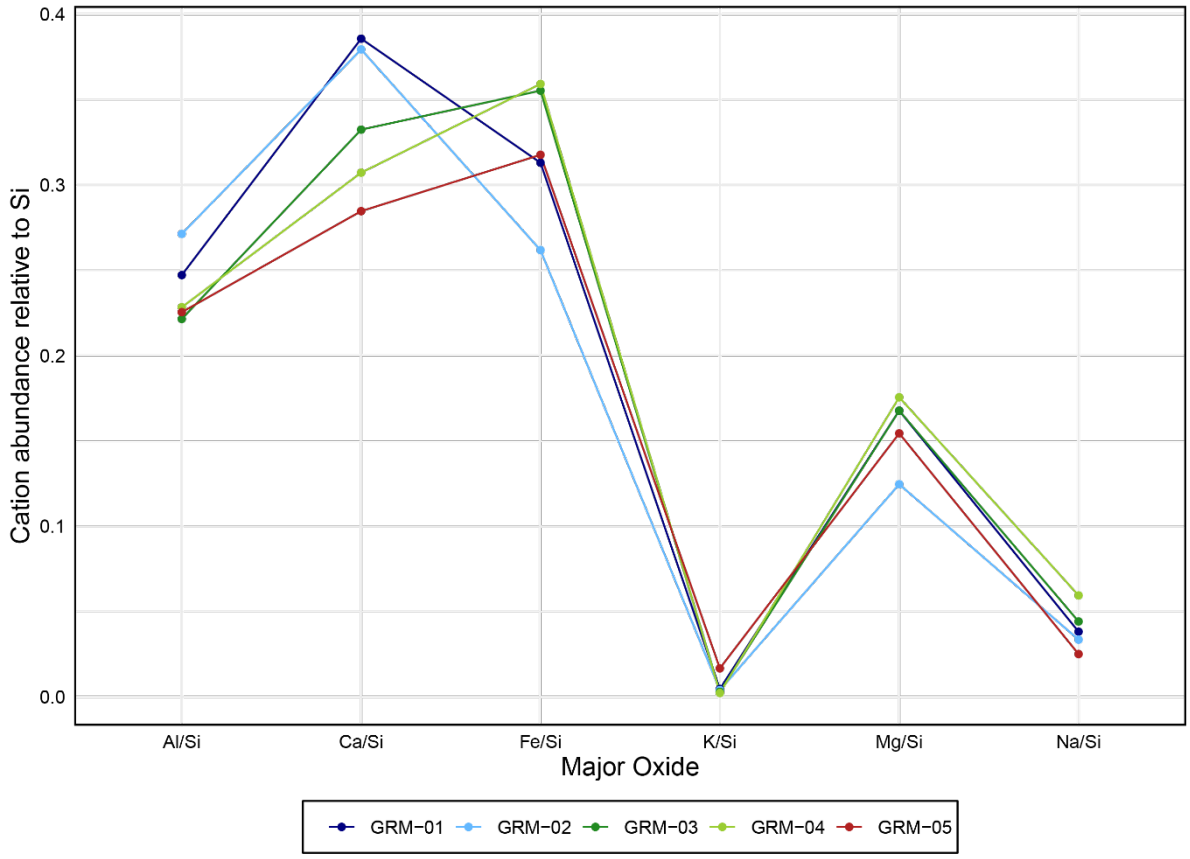

Figure 38 ***Cation concentrations relative to Si within the dissolution samples.*** *Most samples share similar profiles, albeit GRM-02 shows an elevated Al ratio and lower Fe and Mg ratios.*

The rare earth element plot from XRF results shows two groups (Figure 39), one with a steeper profile indicating a greater concentration of LREE relative to HREE compared to group 2. A markedly close profile shared between the inter-lava bed (GRM-05) and flow 10 samples makeup group 1 with flow 8 samples making up group 2. GRM-02 shares an almost identical profile to GRM-01, just lower, a result of LOI discrepancies.

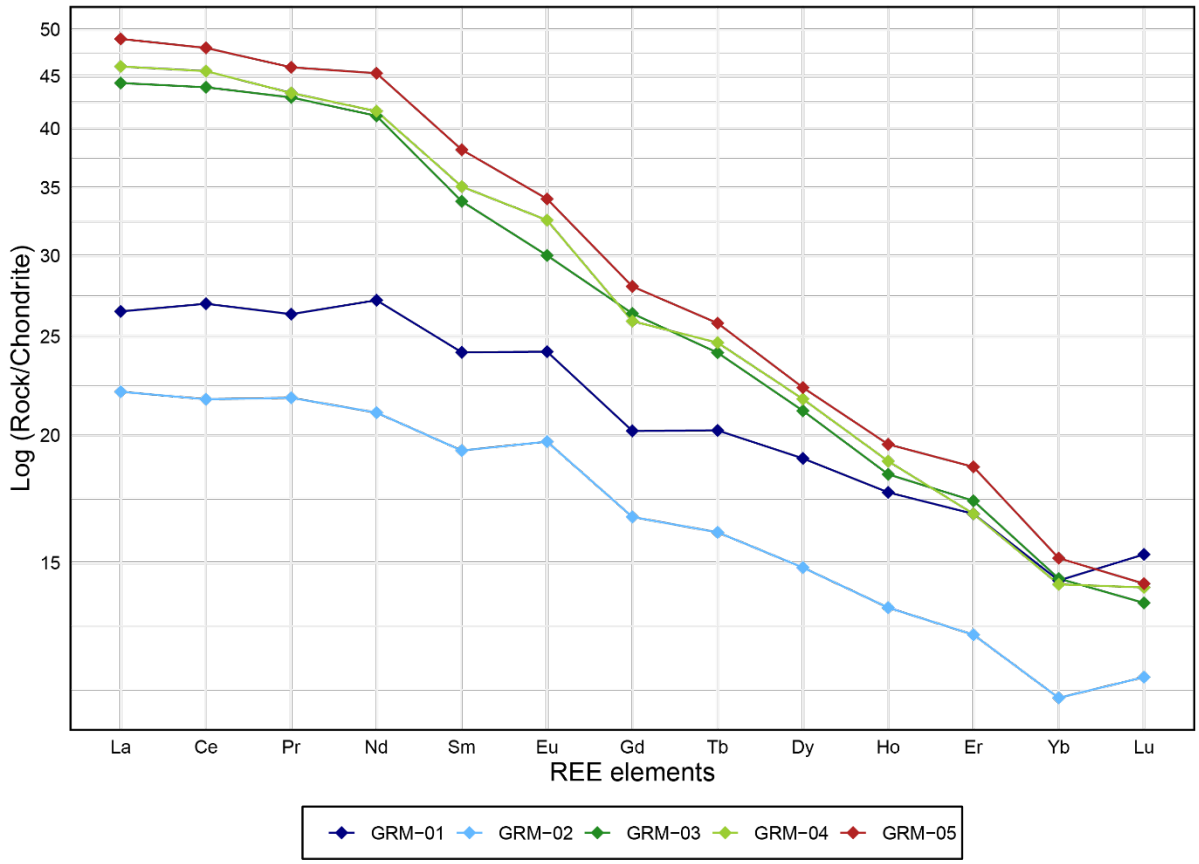

Figure 39 ***REE plot from XRF results on samples GRM-01 to GRM-05.*** *There appear to be two groups, one enriched in LREE and the other depleted in LREE. GRM-02 shares a very similar profile to GRM-03, just lower due to LOI. Chondrite values were taken from* Sun and Mcdonough (1989).

4.7 Petrography and mineral chemistry

Lava flows show a mostly porphyritic texture. Optical petrology combined with back-scatter electron (BSE) images reveal that the lava flows' mineralogy consists of a generally fine-grained holocrystalline texture of trachytic or apathetic type phenocrysts of plagioclase or olivine; however, the plagioclase being more common (Figure 40). The groundmass of the samples are generally devoid of olivine and composed of plagioclase microcrysts (predominantly labrodiorite) of acicular and subhedral laths and clinopyroxene (augite), with lesser amounts of Iron oxides (Illmenite and Ti-magnetite), and orthopyroxene. No textural groupings were observed within the plagioclase, however an ophitic texture within the clinopyroxene is common, where plagioclase laths are enclosed inside the mineral. The majority of plagioclase crystals are isolated, however glomerocrysts are seen. Accessory minerals (<5%) make the remaining mineralogy, include quartz, alkali-feldspar, apatite, chlorite, and smectite.

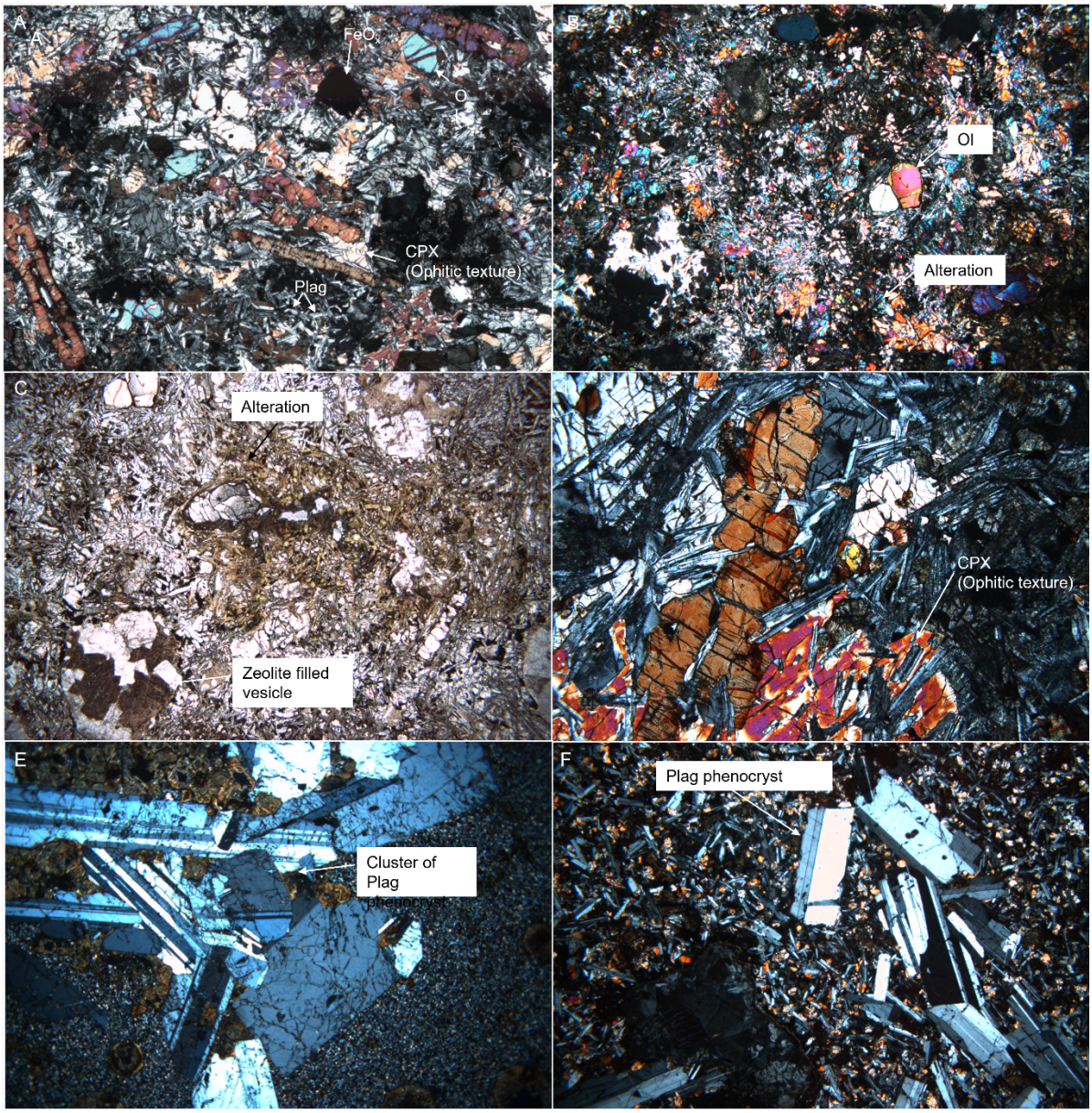

Figure 40 ***Key minerals and relationship.*** *A) F20-11 showing olivine phenocrysts surrounded by a plagioclase clinopyroxene groundmass with ophitic textures throughout B) F20-09 showing fresh olive phenocrysts adjacent to dark alteration zones C) F20-09 with distinctive green coloured alteration within the centre of the image and the presence of zeolite filled vesicles D) F20-11 dislaying ophitic textures E) GM-11 clusters of plagioclase phenocrysts F) GM-17 fresh plagioclase pheocrysts.*

The mineralogy of the red beds was hard to determine via optical means due to their extensive alteration, and thus the use of SEM was applied to understand the mineralogy of the red beds. The mineralogy of a pyroclastic bed and fluvial bed were analyzed. The pyroclastic and fluvial inter-lava beds are composed of clasts of lava flow material, glass, plagioclase, clays such as smectite and chlorite, and various forms of zeolites (Figure 41). The pyroclastic bed shows the addition of individual alkai-feldspar and plagioclase grains. Both inter-lava beds show clasts of lava flow material composed of micro-crystalline plagioclase, alkali-feldspar and clinopyroxene. Within the pyroclastic sample, one clast showed alkali-feldspar crystals with a elonglated lath habit with the edges of the alkali-feldspar

showing a plagioclase composition. Around the rims of the grains in both bed types smectite is often seen covering there surfaces. The grains appear to be angular and well sorted, with surfaces coated in an iron-rich coating causing their red appearance.

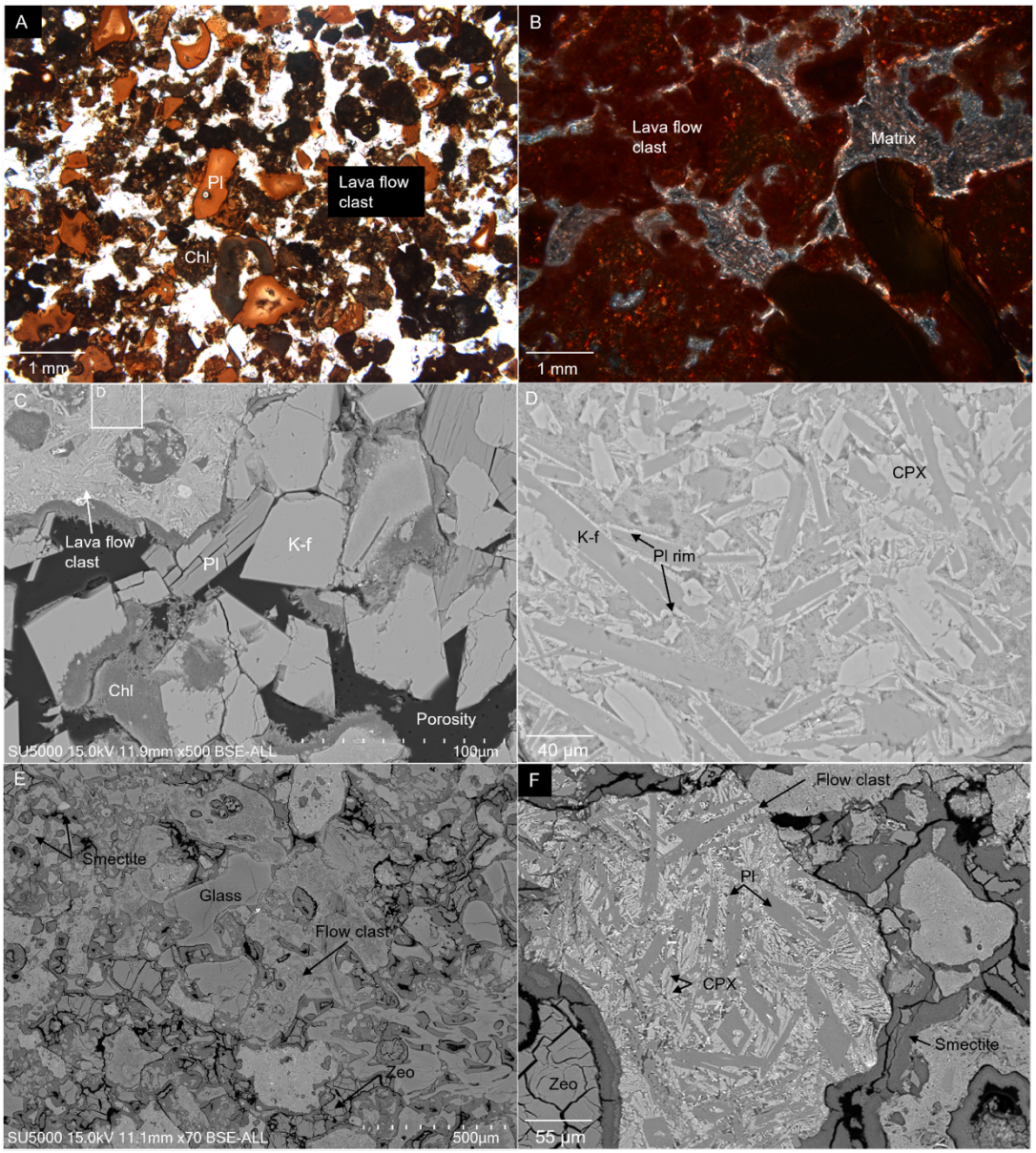

Figure 41 ***Mineralogy of the inter-lava beds****. A and B are optical images showing GM-23 (pyroclastic bed) and GRM-05 (fluvial bed) in PPL and XPL respectively. The redennded grains show significant Fe precipitation on the surfaces with large grains of eroded lava flow material being both crystalline and glass. C) BSE of a pyroclastic red bed. The BSE image shows clasts of lava flow material with a microcrystalline texture, grains of alkali-feldspar, plagioclase, and clay in the form of chlorite (chl) though smectite is common throughout. D) A closer up of lava flow crystalline clast represented in C. The clast contains laths of alkali-feldspar (K-f) with plagioclase (Pl) rims and CPX crystals. E) Overview BSE image of a fluvial interleave bed, mostly composed of vlcanic glass, lava flow clasts, zeolites, and smectite which rims most of the grains. F) close up section of a lava flow clast showing plagioclase and CPX.*

Zeolites are the major secondary mineral filling the porosity of the samples. However, lesser forms occur as glauconite and other pervasive forms of secondary mineralization throughout the samples are alkali-feldsapr, clays (chlorite and smectite), and quartz all commonly associated with fractures. Open porosity within the samples is in the form of micro-fractures that are often connected to inter-

granular secondary porosity along the rims of vesicles filled with zeolites and intra-granular porosity within the zeolites (Figure 42). The zeolites are confined to the vesicles of the lava flows connected by a network of fractures identified by the dark alteration zones. The vesicles can have a rim of either zeolites or clay. All vesicles observed within the sample set are filled almost entirely with zeolites.

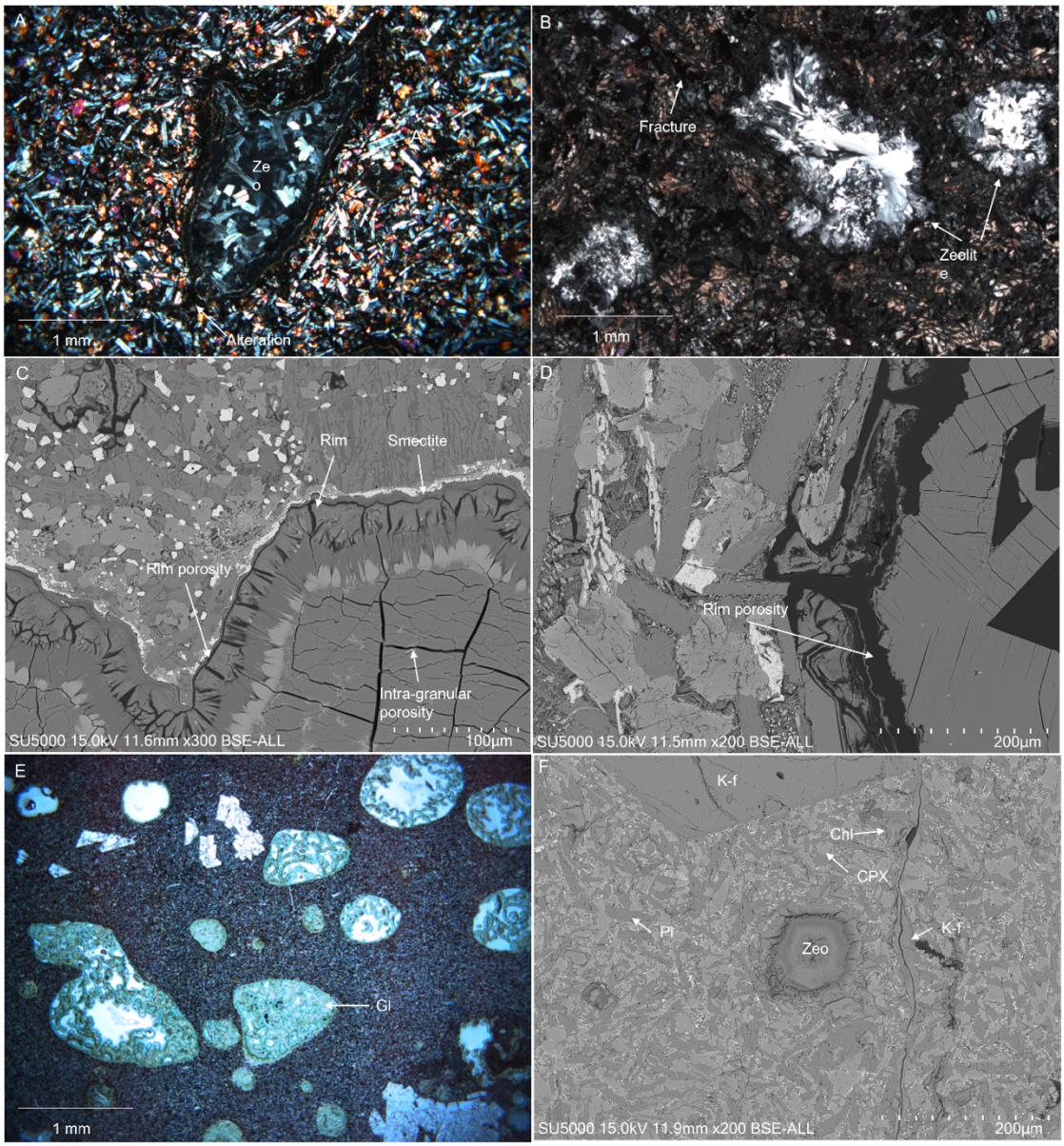

Figure 42 ***Zeolites seen in the thin sections.*** *A) GM-09 - a zeolite filled vesicle surrounded by plagioclase and clinopyroxene showing a dark alteration zone surrounding it, which appears to continue into the bottom left corner of the image. Towards the rim of the vesicle, a zeolite with a different form appears. B) F20-09 - Zeolite filled vesicles with a dark alteration network running between the adjacent zeolites. C) GM-14 - BSE image of the rim of a zeolite filled vesicle. The vesicle contains three types of zeolites from the centre to the edge. Smectite surrounds the edge of the vesicle. Porosity is present as an intra-granular porosity within the centre of the vesicle and around the rim. D) GM-18 - BSE image showing the present rim porosity of a filled vesicle. E) GM-13 - Glauconite filled vesicles. F) GM-14 - BSE image showing a fracture towards the centre-right of the image. The image shows a large alkali-feldspar (K-f) phenocryst in the top middle. The fracture is filled with chlorite (chl) and alkali-feldsapar. The image also shows a zeolite-filled vesicle and plagioclase, showing significant presence of albite and K-rich plagioclase patches.*

It is common for the plagioclse crystals to show thin Na-rich (albitic) rims with the Na phase becoming more prevelat towards the outer edge of the crystal with the cores showing a predominant

labrodiorite composition. The cores of the plagioclase occasionally express oscilatory zoning, however this is limited and the majority of the cores are homogeneous (Figure 43). Overall EDS data has shown plagioclase compositions to be relatively consistent throughout the samples with minor compositional ranges in some of the more altered samples, such as flow tops or within fracture zones for irregular patches of both Na and K representing albite and alkai-feldspar, respectively. Pyroxene also displays a variable composition, with some areas Ca-rich and others Mg-rich linked to augite (clinopyroxene) and enstatite (orthopyroxene) respectively, with augite the most common of the two (Figure 43). The Ca-rich and Na-rich plagioclase distribution does not seem to follow any particular pattern; however, flow tops have generally undergone more pervasive alteration than flow cores.

Patches of the most extensive alteration are seen adjacent to fractures. K-feldspar is commonly associated with these fractures. These zones often appear as dark bands through the sample, which can be seen in both thin sections and SEM to originate from fractures running through the sample. It is also common to observe greater abundances of minerals such as alkali-feldspar, ilmenite, and clays (chlorite and smectite) adjacent to fractured zones (Figure 43). In addition to fractures, it is also possible to see similar alteration next to some vesicles, though most vesicles show no alteration in their immediate proximity.

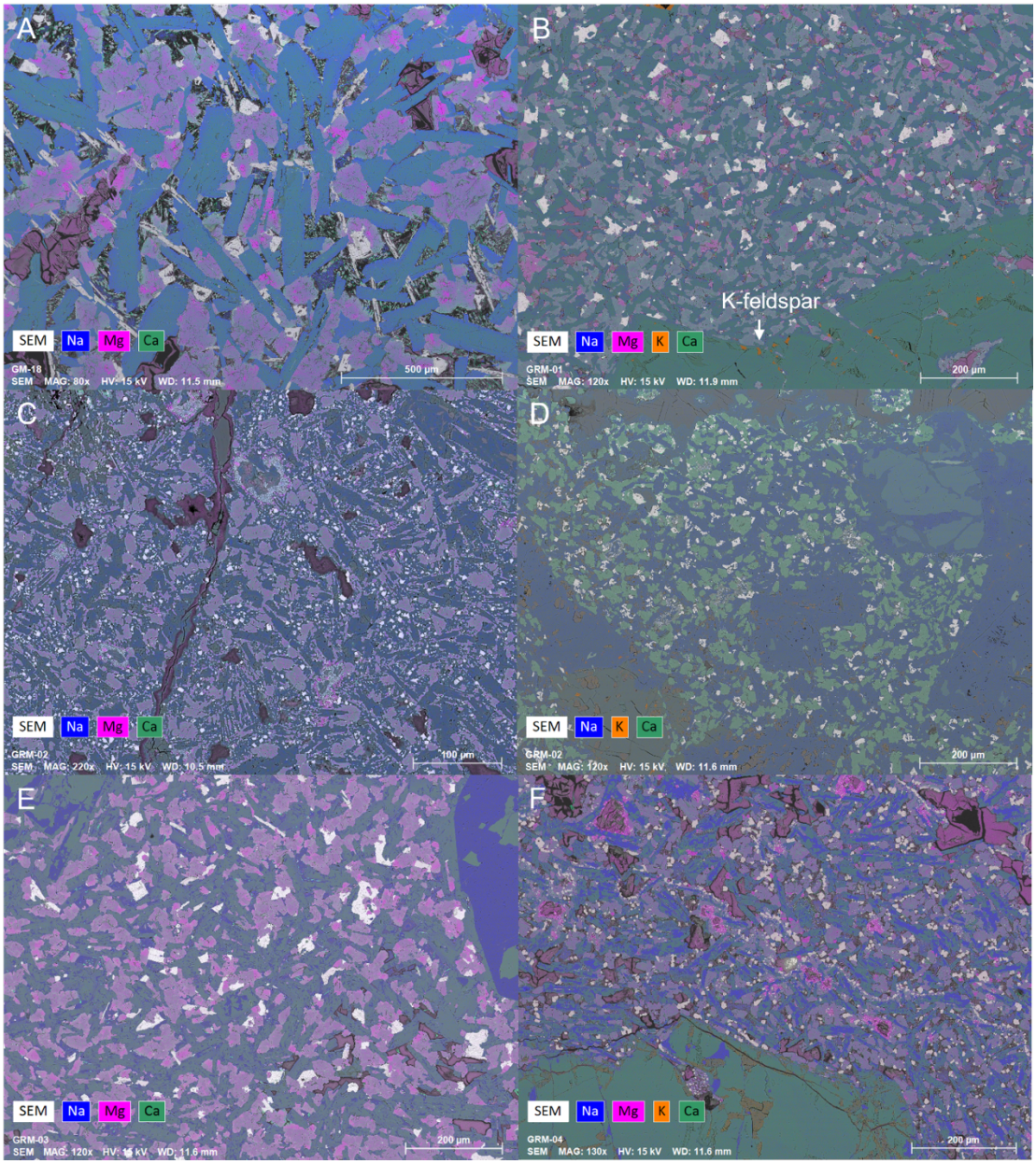

Figure 43 ***Plagiocalse elemental distribution using EDS elemental maps.*** *Samples are dominated by plagioclase, mostly labrodiorite, and clinopyroxene, Augite. The samples show lesser amounts of FeO_x minerals (Illmenite and Ti-magnetite), clays (smectite and chlorite), and +/- olivine. Plagioclase crystals show thin Na-rich rims with relatively homogeneous cores, although the occasionally patchy realm is present with both Na and K rich area related to albitization and alkali-feldspar respectively especially within lava flow top sampes and proximity to fractures.. A) GM-18 showing long slender plagioclase crystals with Ca-rich cores and Na rich rims. B) GRM-01 with specks of K-feldspar on the lower right plagioclase phenocryst. Most plagioclase is Ca-rich C) GRM-02 showing significant alteration of labrodiorite to albite. D) GRM-02 Specks of K-feldspar within both plagioclase phenocrysts and significant albitization of plagioclase. E) GRM-03 with a groundmass of plagioclase and pyroxene with the latter enstatite composition.F) GRM-04 is expressing alkali-feldspar replacement of plagioclase labrodiorite on the large phenocrysts at the base of the image. High Mg is expressed by both clays and zeolites.*

Zeolite, the main pore filler within the samples (Figure 44), comprises different zeolites with Ca-rich zeolites commonly seen in pore centres and Na and Mg-rich zeolites towards the pore rim. The Faroe Islands show zeolites such as analcime, stilbite, heulandite, mesolite, and chabazite varieties. The BSE imagines (Figure 44) show radial patterns of some zeolites growing into a pores centre. Further, many

samples show a distinctive rim to the vesicles towards the reactive wall rock, which was different from the pore filling. These rims tend to be clays such as chlorite and glauconite coating the reactive rock (Figure 44).

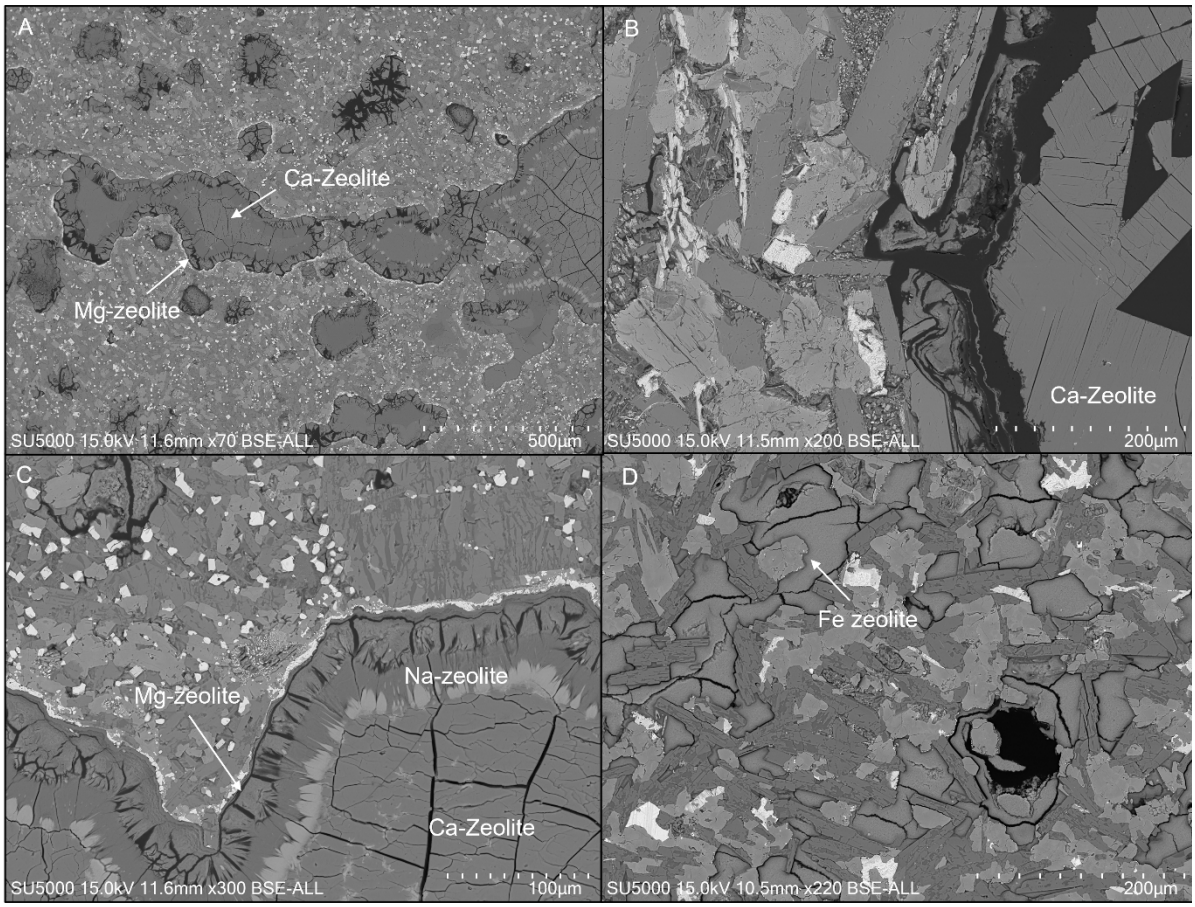

Figure 44 ***<u>Common types of zeolites found within the sample set.</u>*** *A) GRM-04 showing a Mg-zeolite rim and a Ca-zeolite core B) GM-18 showing the lath shaped crystals of a Ca-zeolite C) GRM-04 a close up of the same pore as A showing the addition of a Na-zeolite between the rim and core D) GRM-03 a Fe-zeolite.*

4.8 Mineralogy of the reactivity samples

The samples represent aphyric and plagioclase phyric types with their mineralogy and modal abundances displayed in Table 13 and optical and BSE images in Figure 45.

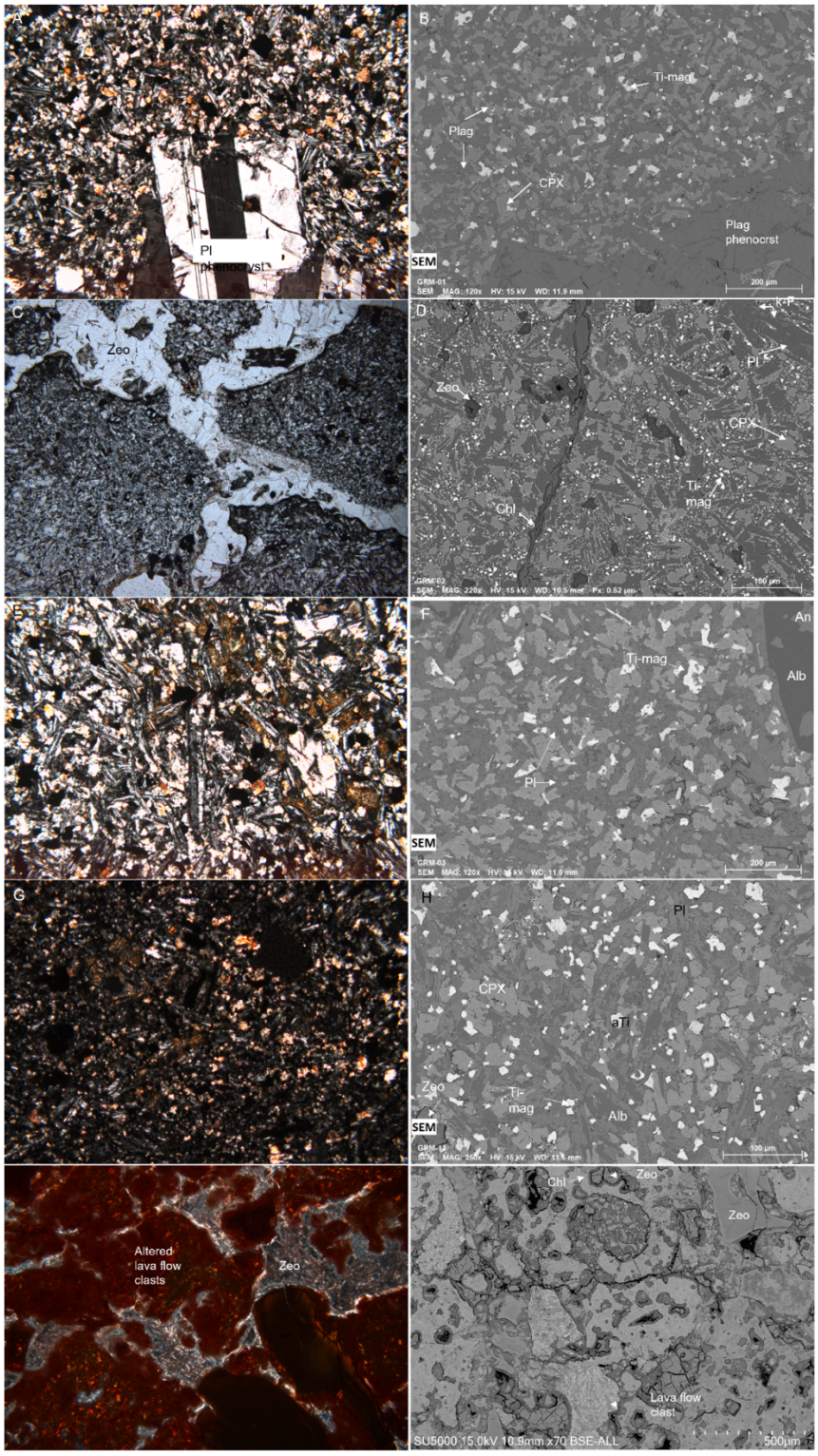

Figure 45 ***Mineralogy of the dissolution samples.*** *A) GRM-01 petrographic microscope image in XPL with a large plagioclase phenocryst, B) BSE of GRM-01 showing little alteration to the plagioclase and CPX groundmass and plagioclase phenocryst, C) GRM-02 petrographic microscope image in PPL showing zeolite filled fractures. D) BSE image of GRM-02 with a fracture running through the centre and filled with smectite and zeolites. The plagioclase shows albitization. E) GRM-03 petrographic microscope image in XPL showing patches of alteration. F) BSE image of GRM-03 with relatively unaltered CPX and plagioclase groundmass, whereas the plagioclase phenocryst shows albitiization. G) GRM-04 petrographic microscope image in XPL showing a fine-grained groundmass with significant iron-oxides. H) BSE image of GRM-04 showing plagioclase with patches of albitization I) GRM-05 petrographic microscope image in XPL altered lava flow clasts with zeolites between the grains. J) BSE image of GRM-05 displaying crystalline basalt and glass clasts with numerous zeolites and clay.*

Table 13 ***Modal abundances of the reactivity samples***

Mineral	GRM-01 (%)	GRM-02 (%)	GRM-03 (%)	GRM-04 (%)	GRM-05 (%)
Ca-rich Plagioclase	*62.62*	*34.20*	*46.95*	*24.59*	11.41
Clinopyroxene	*27.19*	*18.19*	*24.15*	*18.39*	15.51
Orthopyroxene	*2.98*	*–*	*5.46*	*1.19*	*–*
Ti-magnetite	*3.10*	*4.46*	*2.74*	*2.48*	0.99
Glass	*–*	*–*	*–*	*–*	19.65
Zeolites	*1.05*	*33.96*	*4.0*	*27.82*	24.31
Na-rich plagioclase	*–*	*3.79*	*8.36*	*23.05*	*–*
K-feldspar	*1.02*	*2.17*	*–*	*–*	0.47
Ilmenite	*1.47*	*1.88*	*–*	*1.62*	*–*
Smectite/chl	*0.57*	*3.23*	*0.28*	*0.86*	27.65

The samples are predominately composed of plagioclase labradorite and clinopyroxene augite with lesser amounts of ti-magnetite. Zeolites concentrations vary between samples with the highest within flow tops and the inter-lava bed; the same is true for clays.

The chemical variability within the dissolution samples shows more pagioclase of lower An varieties within flow 10 compared 8, with the addition of plagioclase andesine, which is still minor to plagioclase labradorite. Flow 8 differs with more An rich plagioclase with minor amounts of plagioclse bytownite. Alkali-feldspar is present within the plagioclase phenocrysts of GRM-01 and GRM-02 shown by the K in Figure 46, which shows a rough perspective of the elemental distributions within each individual sample.

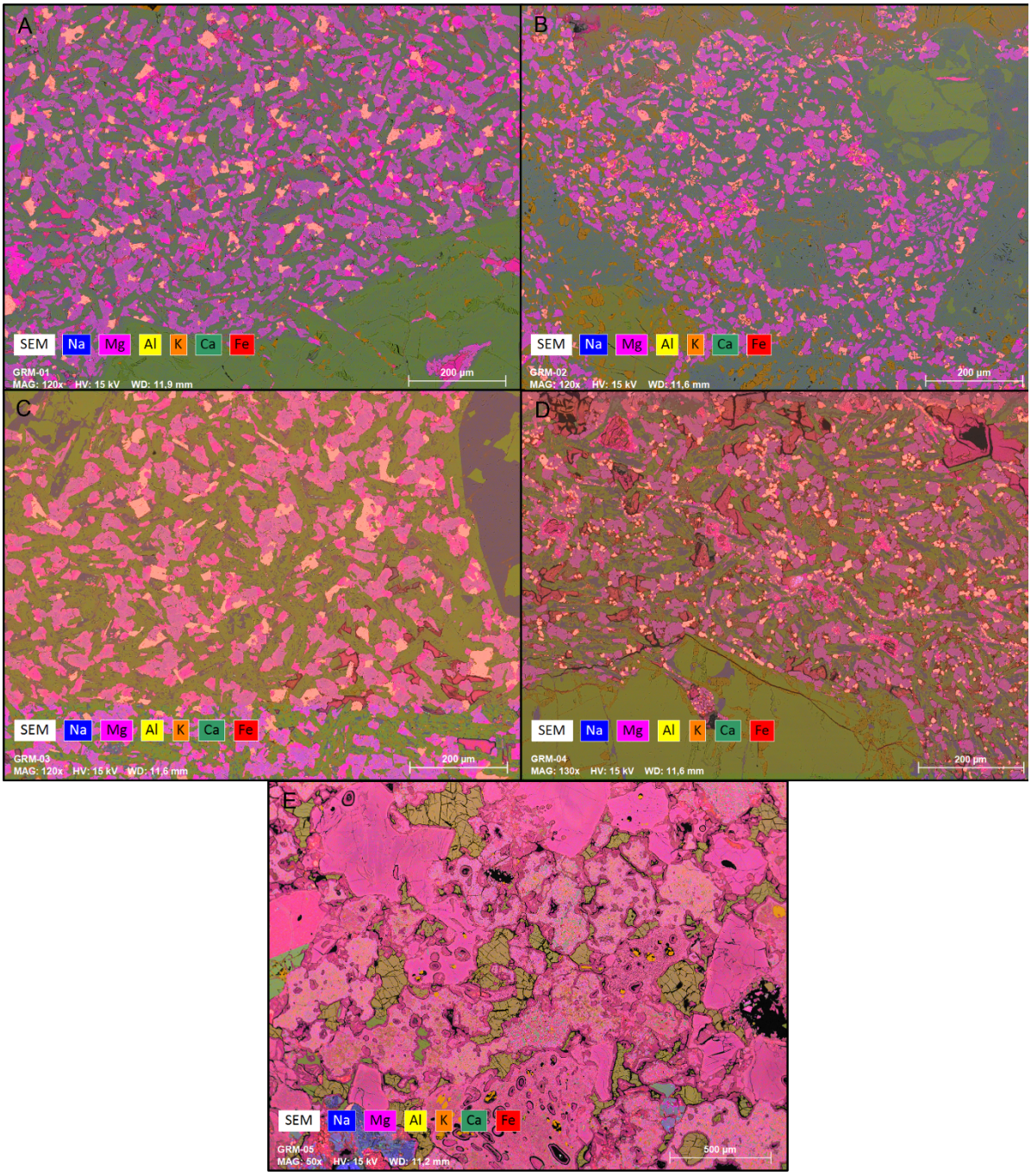

Figure 46 ***Elemental distributions within dissolution samples.*** *A) GRM-01 plagioclase shows a predominate labrodiorite composition with spots of alkali-feldspar on the plagioclase phenocryst. B) GRM-02 plagioclase labrodiorite shows albitization with most becoming more Na rich but still within the labrodiorite field, the sample shows more significant alkai-feldspar alteration and a network of zeolites in the upper section of the image. C) GRM-03 plagioclase has some albitization and the pyroxene in the lower part of the image is more Mg rich than the middle and upper parts showing more Fe D) GRM-04 extensive albitization to the plagioclase with significant zeolites and clays. E) GRM-05 high in Mg with Ca-rich zeolites. Spots of alkali-feldspar can be seen throughout.*

4.9 Porosity distribution

The CT scans show the vesicles to be rounded to sub-rounded and almost entirely filled with secondary minerals, zeolites and clays. The secondary minerals filling the vesicles show some inter and intra-crystalline porosity but no obvious inter or intra crystalline porosity is found within the primary

mineralogy of the samples (Figure 47). The flow top contains the largest vesicles, followed by the base, which shows the most numerous and thus greatest vesicle coalescence. All samples show a fracture network which with which runs between vesicles within the flow top and base sample and more extensively within the core, crossing the entire sample (Figure 47). Some of these fractures are very fine, whereas others are broader and more obvious to the eye, although they originate from the finer fractures and likely formed from the core extraction process. Some of these broader fractures cross-cut filled vesicles or follow the edge of the vesicles rim. The fractures travel through the groundmass of the sample with no preferred orientation, although conforming to the boundaries of crystals within the groundmass, linking adjacent vesicles.

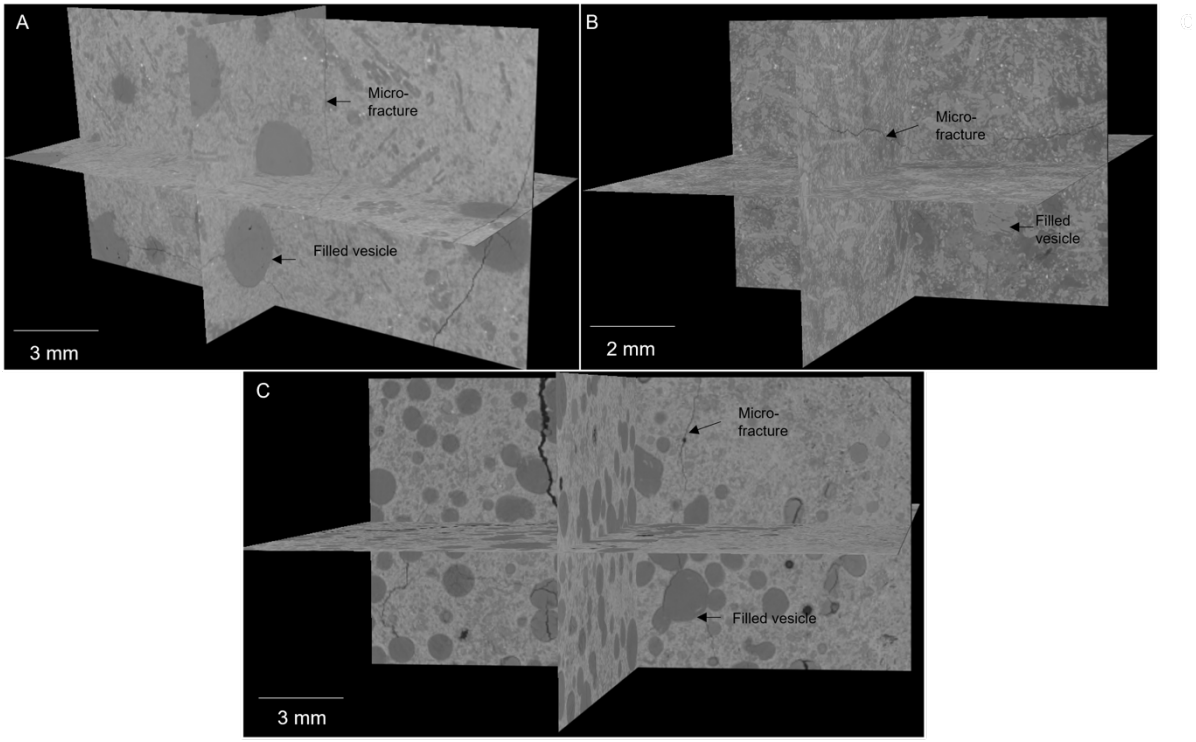

Figure 47 ***Orthoslices of CT scans****. A) F20-10 showing large vesicles and micro-fractures linking vesicles. F20-11 with limited vesicles and secondary mineralization. F20-14 shows two zones, one with more vesicles and one with limited vesicles, in the vesicle rich zone, micro-fractures can be seen linking vesicles.*

The presence of fractures provides a small addition to the porosity of the samples but significantly aids the permeability. The vesicles show show occlusion although this is limited to small groups and not all filled vesicles. The CT scans show the presence of intra-granular porsity alog the rims of the vesicles and within.

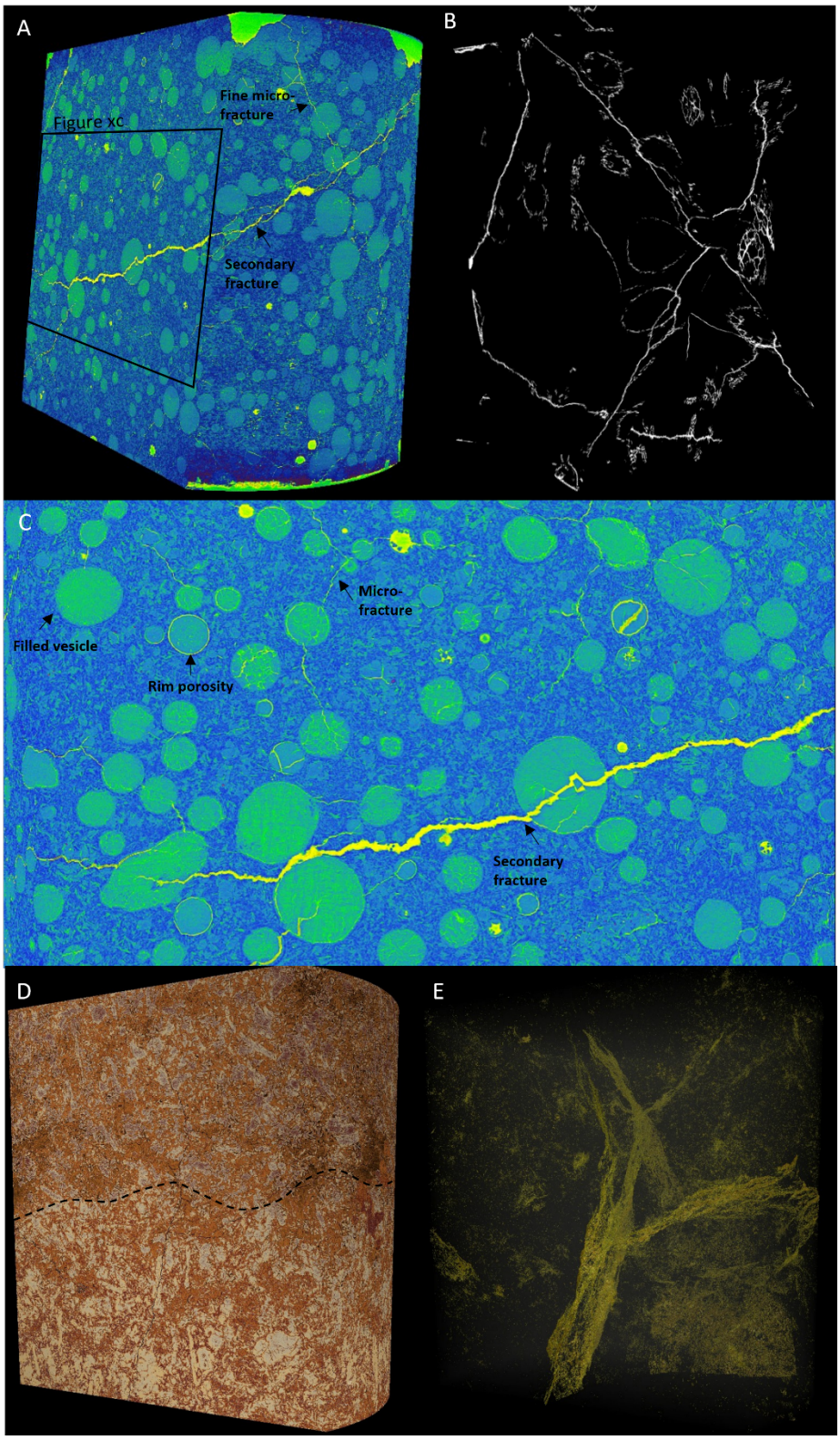

Figure 48 ***Key features observed within the CT sample.*** *A) F20-10 showing micro-fractures stretching between the filled vesicle and the presence of a thicker secondary fracture likely caused by the extraction process, although it appears to originate from these micro-fractures. B) Binary image of F20-10 only showing the open porosity. C) close up of the panel in A showing the mass of filled vesicles and fractures. Open porosity can surround the rim of many filled vesicles and within the secondary mineralization. D) Coloured reconstruction of F20-14 showing two distinctive zones defined by the secondary minerals filling vesicles shown by the dashed boundary. E) Image of F20-14 showing the open porosity within the sample.*

The CT scans were segmented to pick areas of interest and to perform calculations. These included porosities (primary and secondary) and the ability to calculate the original porosity of the samples. Table 14 shows the expected present and paleo-porosity on all the CT scans from the classified images shown in Figure 49.

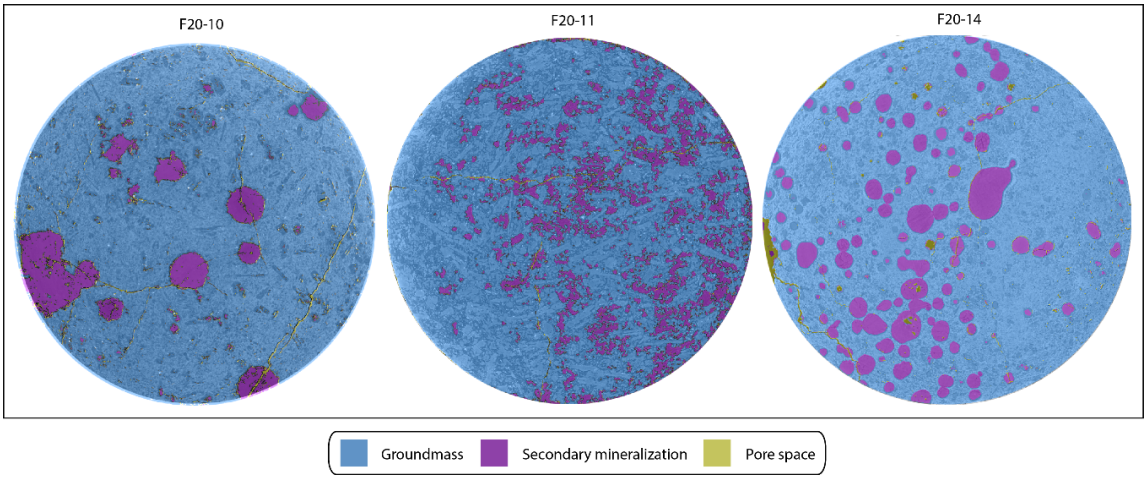

Figure 49 ***Classified CT scans****. Each sample shows the classification of the groundmass, secondary mineralization, and pore space.*

Table 14 ***Statistical data from the CT scans***

Calculation	F20-10	F20-11	F20-14
Present porosity (%)	*4.5*	*1.0*	*1.2*
Secondary mineralization (%)	*16.1*	*25.0*	*24.0*
Original porosity (%)	*20.6*	*1.0*	*25.2*

The CT scans show that the expected paleo porosities were significantly larger than current values for the lava flow top and base when removing the secondary mineralization within the vesicles. We also see the secondary mineralization within the flow core sample, although the secondary mineralization is very pervasive and not confined to vesicles like the flow top and base samples. As a result, the paleo-porosity within the lava flow core sample is determined to be the same as today. Fracturing appears to be most significant within the flow top, followed by the base and least in the core sample.

4.10 Specific surface areas

Specific surface areas were gathered to understand the reactive surface area for each of the fractions. The BET specific surface areas and the surface roughness factor are shown in Table 15.

Table 15 ***BET specific surface areas***

Sample	BET (m^2/g)	Surface roughness factor[a]
GRM-01	*2.04*	*82.9*
GRM-02	*44.02*	*1789.4*
GRM-03	*4.26*	*173.2*
GRM-04	*6.66*	*270.7*
GRM-05	*12.39*	*503.7*

[a] *BET/geo*

The top of flow 8 shows the large largest surface area by nearly four times the flowing sample. Both flow cores show smaller surface areas than their respective flow top. The surface roughness factor is included to show the differences between the BET surface area and the geometric surface area for each sample.

4.11 Dissolution experiments

Five experiments were carried out on four crystalline basalt samples and one sediment to understand the differences between lava flows, inter-lava beds, and flow architectures (lava flow tops and cores). Dissolution experiments were run for up to 700 hours at 25°C with pH 4 solution when steady-state conditions were achieved. The results of the experiments are highlighted in Table 16 where the average outlet pH, time to reach steady state conditions, final average elemental concentrations, and average steady-state Log_{SiBET} and Log_{Sigeo} dissolution rates for each sample are reported.

Table 16 ***Steady-state dissolution results.***

Sample	Flow rate	Outlet pH	Time to steady-state (hrs)	Si	Al	Ca	Mg	Fe	Log $r_{Si, BET}$	Log $r_{Si, geo}$
GRM-01	*1.83*	*4.07*	*558.6*	*4.90*	*3.03*	*1.52*	*0.43*	*0.46*	*-14.74*	*-12.82*
GRM-02	*1.97*	*4.60*	*125.98*	*24.32*	*20.30*	*9.04*	*0.20*	*0.05*	*-15.34*	*-12.09*
GRM-03	*1.77*	*4.18*	*505.77*	*9.82*	*8.14*	*3.91*	*0.63*	*0.71*	*-14.77*	*-12.53*
GRM-04	*1.86*	*4.18*	*452.95*	*7.53*	*8.13*	*3.23*	*0.43*	*8.13*	*-15.06*	*-12.63*
GRM-05	*1.83*	*4.09*	*452.82*	*7.23*	*2.58*	*2.38*	*1.24*	*0.14*	*-15.35*	*-12.65*

The first ~100 hours represent a relatively volatile phase before becoming more consistent after this interval (Figure 50). The consistent interval represents the steady-state conditions on the individual rocks. In general, the steady-state conditions are achieved after ~450 hours; however, for GRM-02 this steady-state condition is achieved far faster, at ~100 hours. Similar dissolution rates are expressed between the flow cores, whereas the flow tops show a significant difference, with GRM-04 being significantly faster. The steady-state profiles show GRM-01 to be very slightly ahead of GRM-03, followed by GRM-04, GRM-02, and GRM-05, respectively, although the latter two are very close (Table 16, Figure 50). There is also a significant difference between the Log $r_{,SiBET}$ and Log $r_{,SiBET}$ dissolution rates (Table 16). The BET specific surface areas are explicitly used to compare the dissolution results between samples due to their more accurate representation of true surface areas.

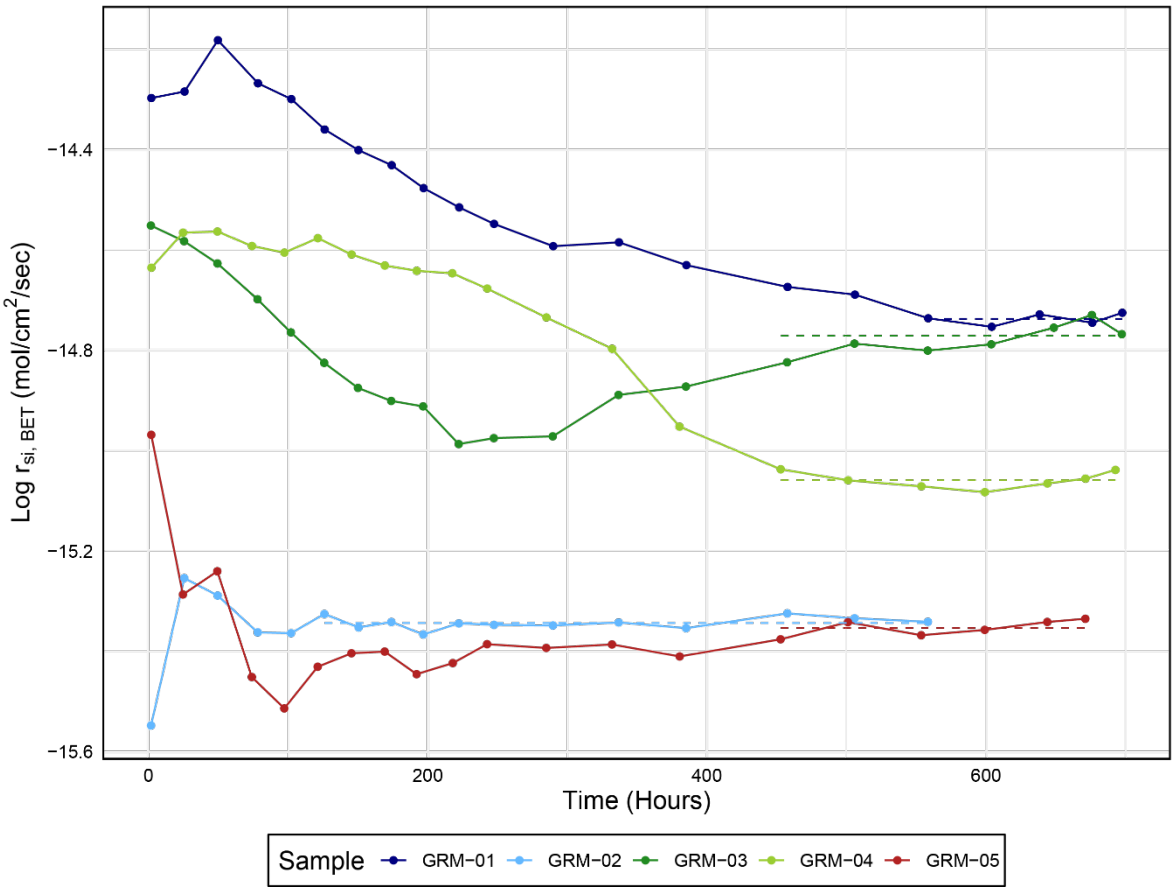

Figure 50 ***Dissolution rate versus time for each sample.*** *The experiments were run at pH 4 and 25°C for over ~700 hours when all the rocks reached a steady dissolution rate shown by a flat projection. At first, the rocks show a more volatile dissolution rate before reaching a steady state. The dotted lines illustrate the used steady-state dissolution rate.*

The elemental release rates reported as a ratio to Si and normalized against the related ratio within the dissolving rock is shown as a function of time in Figure 51. Preferential release of K and Al, clost to stociometric release for Ca, and the preferential retention of Mg and Fe. GRM-05 shows a different trend with Mg being, preferentially retained up to ~280 hours, where it becomes preferentially released, although close to stochiometric release.

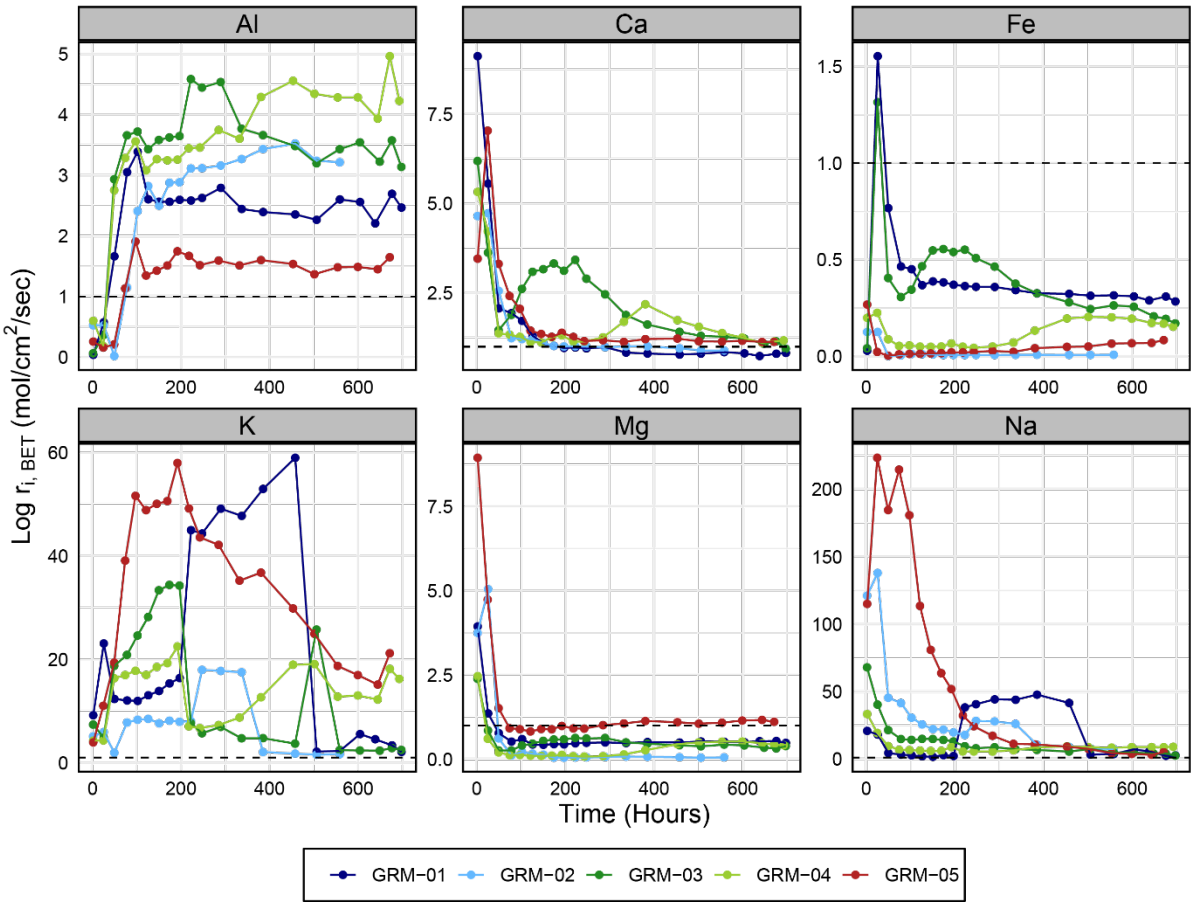

Figure 51 ***Stoichiometric elemental release rates vs time.*** *A line is drawn from 1 to illustrate the stoichiometric release relative to Si for a particular sample; if the ratio is below one the element is preferentially retained relative to Si, whereas if the ratio is above one, the element is preferentially released relative to Si. Data points above one show that element is preferentially released, whereas being below one the element is preferentially retained*

The elemental release rates reported as a ratio to Si and normalized against the related ratio within the dissolving rock are shown as a pH function in Figure 52. The experiments' elemental release rates over the pH changes generally show similar release trends with each element. Ca shows preferential release across the board of samples and pH conditions whereas Mg and Fe do not, with Mg being preferentially released at higher pHs before being retained at lower. Fe is overwhelmingly retained across the pH conditions in all samples. With some exceptions, Al is retained at higher pHs and released at lower.

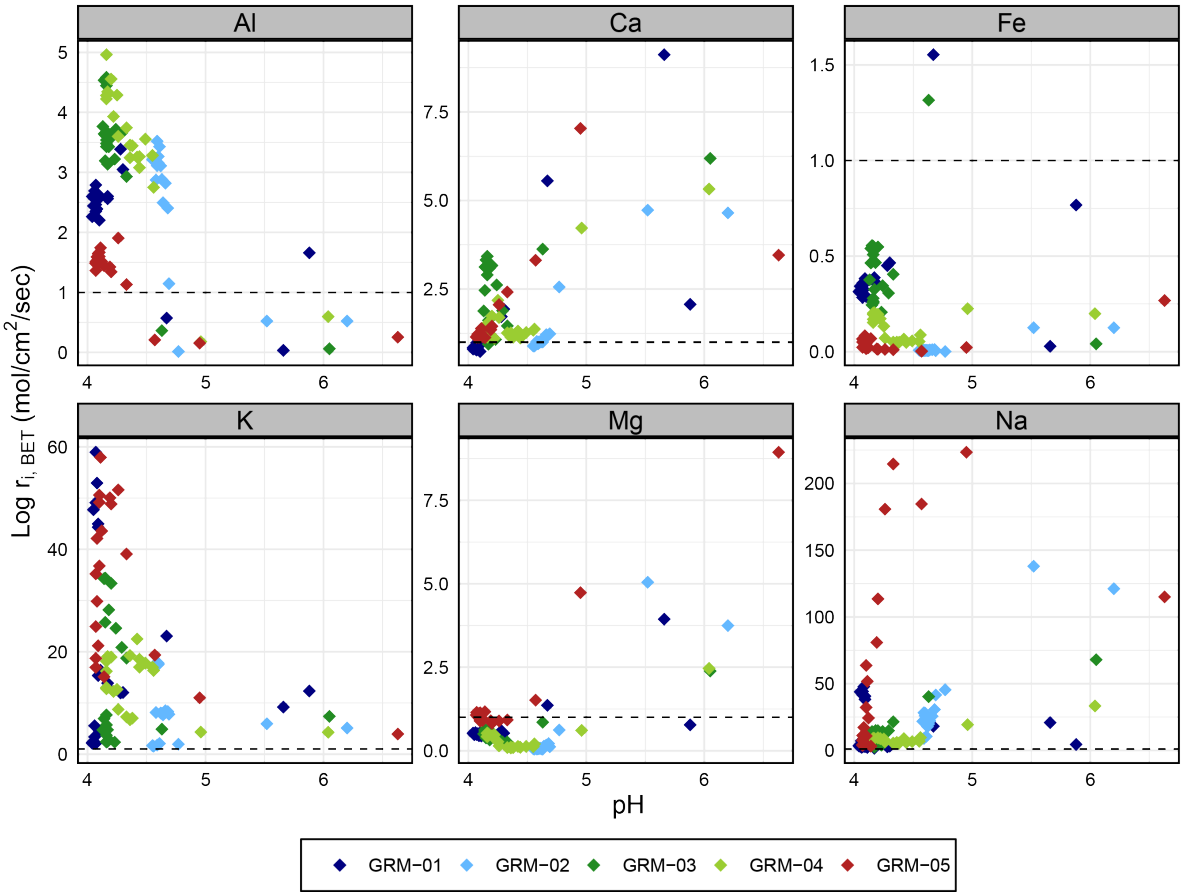

Figure 52 ***Normalized elemental release rates vs pH.*** *Data points above one show that element is preferentially released whereas being below one the element is preferentially retained*

Ca release rates from the dissolving samples relative to the total release rates of divalent metal cations within the rocks is shown to be between 64-97%, whereas Mg ranges between almost 0.01 to 34%, and Fe from almost 0 to 19% and hence Ca represents the most significant divalent metal cation being released (Figure 53).

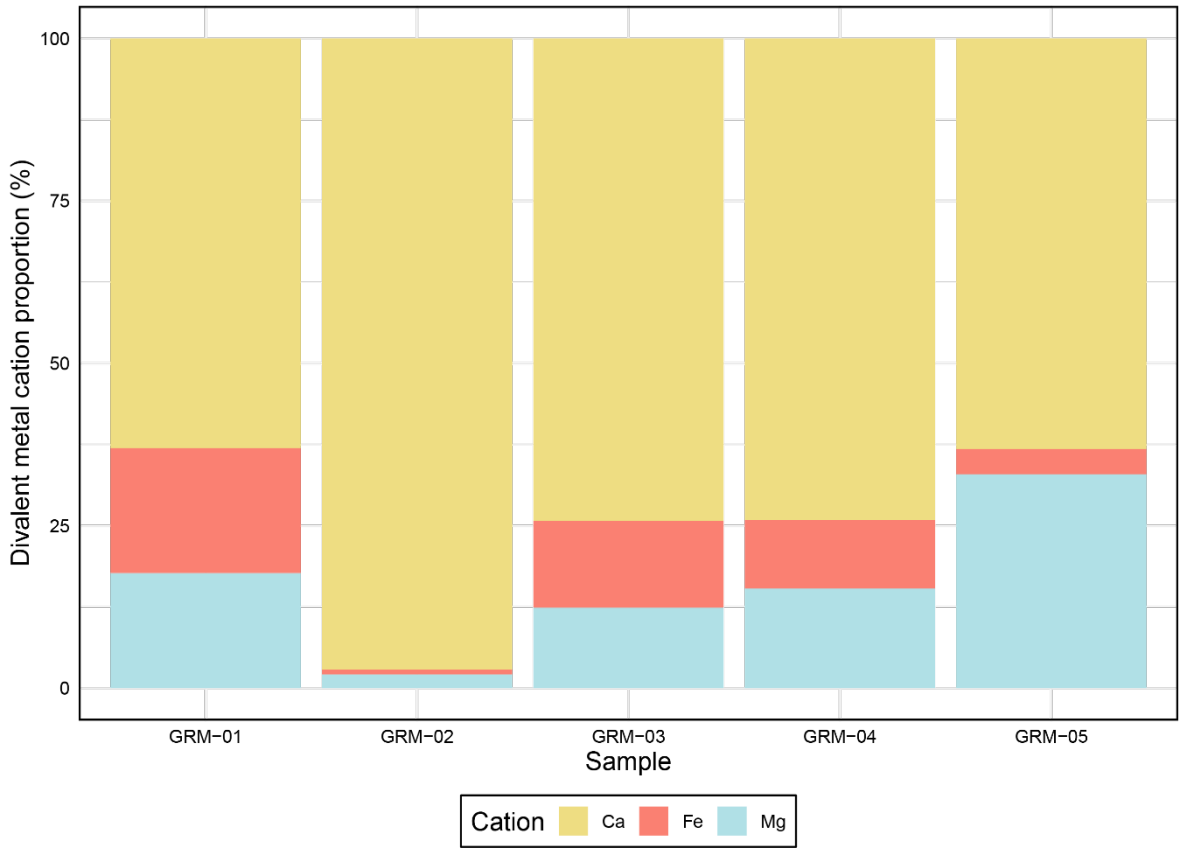

Figure 53 ***Proportions of divalent metal cations being released between the Faroe Islands dissolution samples.*** *Ca is the most prominent divalent cation released by a significant margin, followed by Mg and Fe.*

Throughout the experiments, no secondary minerals were noted within the outlet filter. Figure 54 shows the grains before and after the dissolution experiments. The grains are smaller than their original states, with GRM-03 and GRM-04 showing the least change in size. No secondary minerals are seen on the surfaces of the grains following the completion of the experiments. The grains following the experiments also appear slightly more rounded.

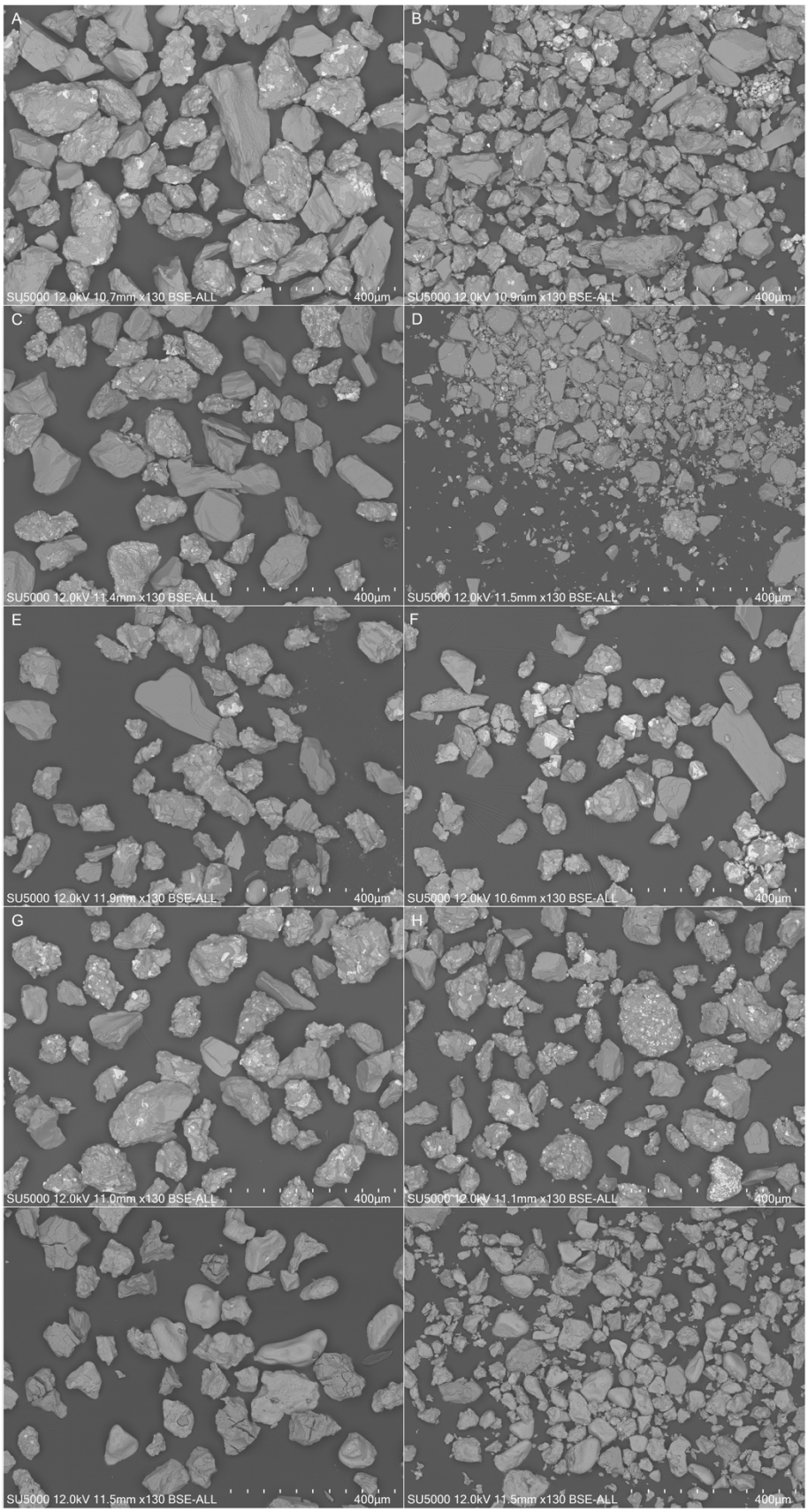

Figure 54 ***BSE images of the samples before and after the dissolution experiments.*** *A and B are GRM-01 before and after respectively the grains are noticeably smaller after and more rounded. B and C are GRM-02 before and after respectively*

Discussion

This study investigates the ability of the Faroe Islands Basalt Group (FIBG) to undergo CO_2 mineral trapping in an injection scenario. The results indicate that permeable inter-lava beds show significant hydraulic communication with successive units from the thinning of simple flows. Furthermore, the study demonstrates a correlation between flow top extents and flow type, with compound lava flows tend to have more significant flow tops as a proportion of the flow volume. However, the ability for those flow tops to communicate with each other will likely be limited by the lack of fractures spanning the cores of each lobe. In addition, it has been shown that the presence of inter-lava beds significantly increases the number of pipe vesicles and vesiculation within the flow base of the overlying flow. Data from the high-resolution CT scans have shown the presence of microfractures providing links between vesicles, and the analysis of the dissolution experiments confirm that basalts from the Faroe Islands represent the reactive lithology required for mineral trapping.

5.1 Petrology and geochemistry

In this study, the mineralogy of the lava flows and inter-lava beds showed little variation, with the largest discrepancies represented the presence or absence of olvine in low and high-Ti lava flows and some variability within the types of plagioclase. Because of the relatively homogeneous mineral asseblage seen within the FIBG, the type of carbonate precipitation is theorized to be highly dependent on flow classification.

The overall mineralogy of the investigated samples was dominated by plagioclase and clinopyroxene, and varying amounts of olivine and zeolites, including volcanic glass within inter-lava beds. Observations from this study have shown plagioclase labradorite to be the dominant mineral with little compositional variability, albeit with the presence of albite patches which are more prevalent within the flow tops and adjacent to fracture zones. When olivine was present, it appeared fresh, even close to alteration zones, which is important to maintaining its solubility and divalent cation proportions. Both plagioclase alteration and the presence of secondary minerals are expected to be more limited in offshore areas of the Faroe Islands Basalt Group (FIBG) due to reduced burial loads leading to less burial metamorphism (Chalmers and Waagstein, 2006; Passey and Jolley, 2009). The FIBG represents part of the greater North Atlantic Igneous Province (NAIP) which comprises significant volumes of volcanic sequences (Jerram *et al.*, 2009). Areas within the NAIP such as the Vøring Plateau Margin (VPM) comprise subaerial lava flows, interbedded with thin volcaniclastic beds, split by dykes and sills that may be comparable to the Faore Islands, and thus the Faroe Islands could shed light on

potential reservoir properties for these areas. The application of carbon storage within the NAIP is taken from the 642E well from the VPM, showing significant open porosity compared to the Glyvursnes-1 well from the Faroe Islands (Figure 55).

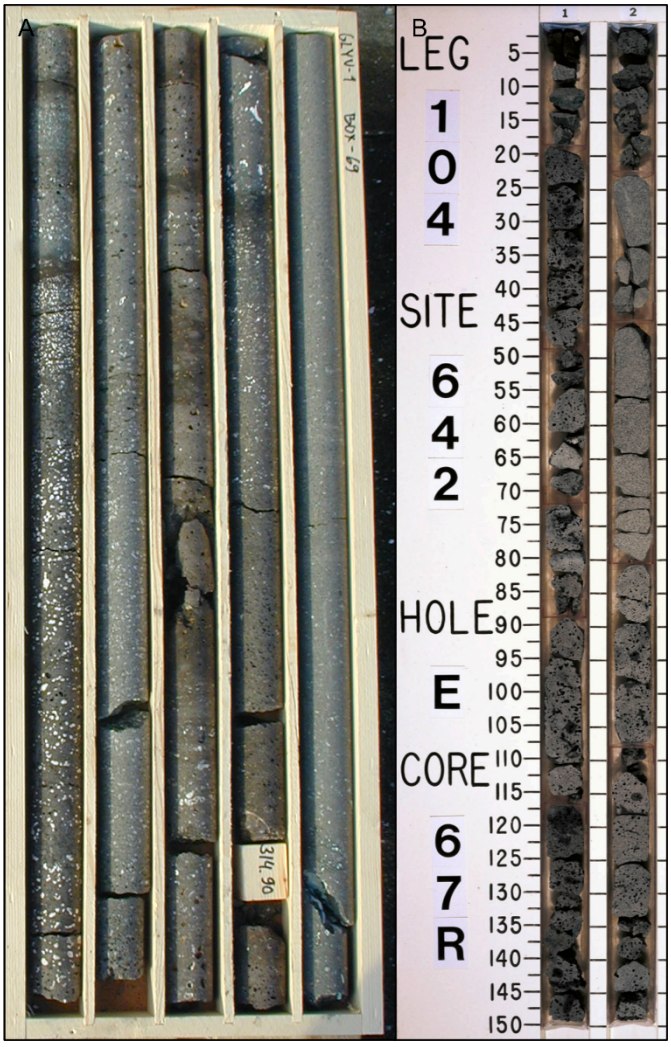

Figure 55 ***Core from Glyvursnes-1, Faroe Islands and 642E well within the NAIP.*** *A) cores from the Glyvursnes-1 well showing significant filled porosity predominantly by zeolites. B) The 642E core showing significant open porosity and representing a potential area for offshore reservoirs.*

Previous studies (Rasmussen and Noe-Nygaard, 1970; Waagstein, 1988; Passey and Bell, 2007; Dahren *et al.*, 2015; Millett *et al.*, 2017) on the petrology and geochemistry of the Faroe Islands basalt have detailed the presence of low and high-Ti for lava flows and two groups of plagioclase representing (An90-80 and A80-60). Waagstein (1988) studied the presence of these low and high-Ti lava flows and found them to be mineralogically distinct, with the low-Ti flows containing olivine and the high-Ti flows being absent in olivine. Furthermore, Millett *et al.* (2017) found low and high-Ti flows to show distinct REE signatures where the high-Ti flows had flatter profiles than low-Ti counterparts, suggesting the difference to be linked to two different magma batches that support differing melt fraction sizes or

sources. This finding is similar to findings from Dahren *et al.* (2015), who suggested the presence of two differing plagioclase groups to indicate two magma reservoirs of differing temperatures and lithostatic pressures. This study found olivine bearing lava flows and evidence for andesine, labradorite, and bytownite, which agrees with previous studies (Rasmussen and Noe-Nygaard, 1970; Waagstein, 1988; Passey and Bell, 2007; Dahren *et al.*, 2015; Millett *et al.*, 2017). However, to date, no studies have investigated if the low and high-Ti flows relate to the two plagioclase groups. Investigating the relationship between the two groups could therefore further aid the understanding of the formation and origins of these lava flows. Understanding the provenance of the lava flows would also shed light on the petrology and geochemistry of the inter-lava beds, which are directly related to the lava flows (Dahren *et al.*, 2015; Millett *et al.*, 2017). This was outside the scope of this study, however it is recommended that this could be an interesting area to explore.

Earlier studies have characterized inter-lava beds on the Faroe Islands to be derived from epiclastic and pyroclastic origins (Mathisen and McPherson, 1991; McGrail et al., 2006; Ólavsdóttir, Andersen and Boldreel, 2015), which is consistent with results from this study. The epiclastic beds contain remobilized volcanic material that is predominately from fluvial deposition and thus share similar mineralogies to the lava flows they have eroded. The pyroclastic beds are sub-parallel to parallel bedding to the surface of the underlying flow unit with minor sedimentary features, consistent thicknesses on steep slopes, and limited erosion of the underlying lava flow. All these findings indicate their province as fallout tuffs rather than reworked volcaniclastics. Based on existing data and findings from this study, it is suggested that inter-lava beds should be grouped based on their depositional environment as they appear to show different morphologies, petrophysical properties, and abundance (pyroclastic beds dominate). This study uses the terminology grey beds for fluvially derived beds and the red beds for the tuff deposits. Determining the petrology and geochemistry of different lava flows and inter-lava beds is significant for how they interact with CO_2 enriched fluids.

The type of carbonate that precipitates is dependent on the availability of divalent metal cations. With the mineralogy of the flows grouped into high or low-Ti flows, available divalent metal cations are dependent on this grouping. As olivine is only present in low-Ti flows, Mg is expected to be significantly more accessible than in high-Ti counterparts, which are dominated by Ca. Ca is found in plagioclase (predominately labradorite), pyroxene, and some Ca-rich zeolites. As high-Ti flows are devoid of olivine, Mg and Fe are found within pyroxenes and iron oxides, although these concentrations are low compared to Ca. It can therefore be assumed that high and low-Ti lava flows may support different carbonates, such as calcite and magnesite. The divalent metal cation proportions of the inter-lava beds are likely to follow the same groupings as the lava flows, as they depend on the underlying lava flow and the magma phase currently at play (low or high-Ti). Thus, the precipitating carbonate in inter-lava

beds is also controlled by the magma phase. The limited red bed sample size should be taken into consideration when applying learnings from this study, although previous research (Passey and Jolley, 2009; Ólavsdóttir, Andersen and Boldreel, 2015; Pokorný, Krmíček and Árting, 2015; Vosgerau *et al.*, 2016) do support these claims .

5.2 Reservoir extents

This study observed the extents of the lava flows and red beds to understand their ability to provide reservoir connectivity and compartmentalization. Previous studies Vosgerau *et al.* (2011, 2016) have found the inter-lava beds on the Faroe Islands to be laterally continuous, likely extending further than the viewed cliff sections. These reports are consistent with the findings in this study. However, the inter-lava beds were also found to have significant connectivity with successive units by the thinning of simple lava flows. Therefore, it is proposed that the inter-lava beds likely play a key role in the reservoir's capacity.

Lava flow cores are generally perceived to be tight, preventing vertical migration of fluids. Lava flows on the Faroe Islands have been found to have variable extents, with previous studies (Passey and Bell, 2007) showing simple lava flows to be more extensive than compound lava flows. Furthermore, Vosgerau *et al.* (2016) found that the thinning of lava flows allows for successive inter-lava beds to join. This study found that simple lava flows show more limited lateral extents, which is in contrast to findings by Passey and Bell (2007). However, this discrepancy may be due to the measured extents being limited to the EF compared to the more extensive study of Passey and Bell (2007), which incorporated all the onshore stratigraphic groups. This study supports the findings in Vosgerau *et al.* (2016), however adds that the simple lava flows control this thinning within the EF. Further findings from this study show there to be an increasing abundance of simple lava flows with stratigraphic height in the EF, an observation agreeing with Petersen (2014). Based on these findingfindings from this study and previous research (Passey and Bell, 2007; Petersen, 2014; Vosgerau *et al.*, 2016) it is suggested that offshore reservoirs, which are stratigraphically higher, will likely be dominated by simple lava flows that show limited lateral extents to provide an extensive network of joining inter-lava beds.

Recent studies have investigated the prospectivity of inter-lava beds within flood basalt sequences in application to oil, and have documented the lateral continuity of the inter-lava beds (Vosgerau *et al.*, 2011, 2016; Couves, 2015; Ólavsdóttir, Andersen and Boldreel, 2015). Results from this study partially agree with these findings, as the red beds were found to be laterally continuous, however the grey beds appeared to be confined to channels. In addition, the thicknesses of the red beds were generally found to be limited to <5m. This study builds on existing evidence that inter-lava beds may form

widespread reservoirs; however, their restricted vertical extents limit their capacity. Therefore it is suggested that the overall capacity of a potential reservoir will be directly linked to the connectivity of multiple porous units.

The addition of intra-lava units may greatly increase the capacity of the reservoir, as well as the quantity of available reactive rock. Studies have investigated the ability for flow tops to provide fluid migration pathways (Japsen et al., 2004; Couves, 2015; Ólavsdóttir, Andersen and Boldreel, 2015; Vosgerau et al., 2016; Ólavsdóttir, Eidesgaard and Stoker, 2017), with the general consensus that flow tops provide the most effective and continuous porosities and permeabilities. It is therefore important to understand the extents of these intra-lava units in understanding their ability to contribute to the capacity of a reservoir. Furthermore, this study has found that the combined volume of the flow tops within the compound flows to likely surpass that of the simple lava flows. However, there is little evidence to suggest that the flow tops within flow lobes of compound flows can effectively communicate with one another and thus, it is noted that the flow tops within the simple lava flows are of more significance to the overall reservoir capacities.

5.3 Reservoir morphology

The interaction between the intra-lava and inter-lava units is essential for both the communication of porous units and their compartmentalization. This indicates the ability of the inter-lava beds to provide significant storage opportunities to sequester CO_2. Thus it is important to understand the morphology of inter-lava beds within the FIBG that may influence the capacities of a reservoir and the movement of CO_2 enriched fluids.

The upper boundary of the inter-lava beds contain a significant localized topography attributed to the differential weight during the emplacement of the overlying flow forming domed structures (Vosgerau *et al.*, 2011). Vosgerau *et al.* (2011) theorized this topography indicates a lack of erosive nature during the emplacement of lava flows. The observation of sedimentary material within the flow bases of the overlying flow in this study contradicts this theory, suggesting the movement and consumption of inter-lava bed material. Further to this, the addition of domed structures within the inter-lava bed is thought to indicate shovelled material, thus supporting minor erosive behaviour during the emplacement of the lava flows. This study also found an increase in both vesiculation and pipe vesicle structures above inter-lava beds compared to occasions where inter-lava beds were not present. Moreover, these vesicles and pipe vesicle structures were more abandunant when associated with domed structures. The domed structures are therefore suggested to provide the potential for fluids to migrate into the lava flow bases, as fluids gather within the domes.

Columnar joints within lava flows span the impermeable flow cores, allowing fluids to migrate between successive porous units. Although numerous studies (Passey and Bell, 2007; Passey and Jolley, 2009; Couves, 2015) have noted columnar joints within the simple lava flows of the onshore FIBG within simple lava flows, the presence of columnar joints were deemed rare by this study. It is therefore expected that these structures will likely not play a major role in supplying vertical pathways for fluids and thus help slow their migration.

Vosgerau *et al.* (2011) and Ólavsdóttir, Andersen and Boldreel (2015) state that the base of the inter-lava beds is markedly planar, with variations resulting from differential erosion or lava flow terminations causing thickness changes within the bed. The studies state the thickness variations to be determined by the erosion of the inter-lava beds, causing complete thinning as well as channels that were observed to be filled with both lava and sediment. Vosgerau *et al.* (2011) suggest the sediment filled channels provide a means of communication to successive inter-lava beds. Observations from this study have found similar features, especially with the thinning of the inter-lava flows, lava-filled channels, and the previously discussed simple lava flow thinning. However, the sediment-filled channels were less prevalent than both Vosgerau *et al.* (2011) and Ólavsdóttir, Andersen and Boldreel (2015) state. Thus, this study suggests that the inter-lava beds' connectivity is significantly more influenced by the thinning of the simple lava flows than sediment filling. As such, the contribution of sediment-filled channels aiding the communication to other porous units and providing extra storage capacities will likely be limited. The addition of lava-filled channels is regularly seen cutting into inter-lava beds and flow top units. Furthermore, this study also indicates that the significant presence of lava-filled channels would likely play a major role in locally compartmentalizing the inter-lava beds and the flow tops of an underlying flow due to their prevalence cutting into inter-lava beds and flow tops.

Compartmentalization of a reservoir is essential to prevent liquids from escaping. Field evidence from previous studies (Passey and Bell, 2007; Vosgerau et al., 2011, 2016; Couves, 2015; Millett et al., 2017) indicate that compartmentalization within the Faroe Islands can be controlled by faulting, lava-filled channels, lava tubes, dykes, and the onlapping of sediment against a rising relief. However, this study found few lava tubes and dykes, suggesting limited contribution to a reservoir's compartmentalization. Furthermore, the ability for faults to transfer fluids should be taken into account as faults may also act as conduits if not sealed which could allow for the leakage and potential fast trasfer of CO_2 enriched fluids. Old faults may also become reactivated from high injection pressures (Vilarrasa, Makhnenko and Laloui, 2017). They may however cause the juxtaposition of permeable units against impermeable flow cores. This study did not observe the onlapping of sediment, a likely consequence of their formation as fall out tuffs with little reworking. Overall this

study suggests lava-filled channels to provide the most significant local scale compartmentalization, with faulting being the most extensive. The ability for faults to act as conduits or seals must be thoroughly surveyed. It is also important to note that the observed cliff sections were perpendicular to the cliff, and any compartmentalization may be regained along the strike of the bed.

5.4 Porosities and permeabilities

Primary magmatic porosity is poorly preserved within the Faroe Islands due to extensive secondary mineralization. However, it is possible to use secondary filled features to understand the paleo primary porosity and thus provide an analogue for offshore settings that have not undergone extensive burial metamorphism.

Porosity is essential to a reservoir's capacity and differs widely depending on the lithology and alteration state. Using data form Couves (2015) it is possible to see the distribution of porosity within lava flow architectures. Flow tops show the most significant porosity followed by flow bases, while core flows show the lowest porosity. These porosities are mostly dependent on the vesicles present within these zones. Findings from this study complement Couves' (2015) findings but build on the units' porosity distribution. Flow units were shown to have highly variable porosity distributions, which provides difficulties for estimating representable porosities for these units. This study notes that porosity distributions within the flow bases are significantly localized and dependent on the presence of an inter-lava bed. The extensive distribution of inter-lava beds aids the porosity of the flow bases, however observation of the inter-lava bed domes, further supports the idea of localized porosity. It may therefore be difficult to understand how fluids might migrate into intra-lava zones using total porosity alone.

Permeability is important to allow for the migration of CO_2 enriched fluids between porous zones. Couves (2015) investigated the permeabilities of the flow architectures within the onshore FIBG. Couves (2015) found the effective porosities of the flows to be tied to the concentration of vesicles and as a result concluded that the presence of coalescing vesicles dominates effective porosity. Due to the vesiculation of the flow tops generally being higher than the flow bases, it can be assumed that the ability of fluid to flow through the flow tops will be greater than flow bases. However, this study showed the presence of micro-fracture networks spanning between vesicles within the CT scans. These micro-fractures provide minimal additions to the porosity, but significantly aid the effective porosity of the sample and likely played a key role for the paleo-fluids to access the vesicles and precipitate zeolites. Applying this learning from the Faroe Islands it may be expected that these micro-fractures, if present in offshore settings, may aid the slow movement of CO_2 charged fluids into the vesicles, increasing the available pore space within the reservoir. Moreover, the presence of micro-

fractures within the porous intra-flow units will help aid the ability of fluids to reach reactive grains that could allow for reaction induced fracturing, further enhancing and maintaining the available reactive surfaces. The Presence of fractures in offshore settings should be therefore investigated. In addition to the porosity and permeability of intra-lava flow architectures, movement may be further aided by the increased porosity and permeability of inter-lava beds.

Ólavsdóttir, Andersen and Boldreel (2015) investigated the porosities and permeabilities of both the red beds and grey beds and found both permeability and porosity were significantly higher within the grey beds, concluding that the fluvial derived beds may provide adequate reservoir units. Although investigating permeability and porosity was beyond the scope of this study, observations may be combined with finding from Ólavsdóttir, Andersen and Boldreel (2015) to aid the application of these findings to offshore settings. This study found the red beds to be significantly more prevalent than the grey beds; as was alluded by Ólavsdóttir, Andersen and Boldreel (2015), with the proportion of each bed sampled being 22% and 78% for grey beds and red beds, respectively. As the majority of inter-lava beds are red beds the available capacity of the reservoir may be limited. However, the upper section of the offshore stratigraphy has not been buried to levels observed on the Faroe Islands, meaning the red beds may retain more primary permeability and porosity. Couves (2015) suggested the importance of preservation of pyroclastic porosity by the degree of welding. Couves (2015) notes this welding to be a factor of emplacement temperature, but also burial. With significantly less burial seen in offshore settings this study predicts the red beds to express greater porosities and permeabilities than those of the Faroe Islands. It is important to investigate the porosities and permeabilities of the red beds in offshore settings to understand the potential for these units to support reservoir qualities.

Evidence from previous literature (Couves, 2015; Ólavsdóttir, Andersen and Boldreel, 2015) combined with observations from this study suggests that the inter-lava beds provide significantly better main fluid pathways than intra-lava units, such as flow tops. This conclusion is based on the channel like networks dominating the permeability within porous intra-lava units; even though micro-fractures significantly aid the effective porosity of the units, their permeability will be low. Inter-lava beds are theorized to contain significantly greater effective porosities and permeabilities derived from their granular nature and theorized limited welding, allowing for faster injection rates. It is also expected that the larger effective porosities within the inter-lava beds likely provides a greater resistance to becoming clogged compared to the narrow channels in intra-lava architectures.

This study shows that the quantity of open-pore space greatly increases when secondary minerals are discounted or significantly reduced. The secondary mineralization of the Faroe Islands will have

influenced the measured porosities and permeabilities of previous literature (Couves, 2015; Ólavsdóttir, Andersen and Boldreel, 2015). Therefore, it is suggested that further investigations into the porosities and permeabilities of the porous intra-lava flow architectures and inter-lava beds should be undertaken to understand the potential capacities within these zones, which will likely be much larger than current estimates suggest. This, therefore, puts observations from the Faroe Islands in context to offshore settings.

5.5 Solubility of the lava flows and volcaniclastic units of the FIBG

Dissolution experiments were conducted to constrain the differences in solubility between the lava flows, inter-lava beds, and flow architectures (flow tops and cores). The results from the dissolution experiments demonstrated that flow cores have faster dissolution rates than corresponding flow tops. Hence, the data supports the theory that differences in alteration influence the dissolution rates. In addition, differences in dissolution rates between distinct lava flows and inter-lava beds support previous claims that the mineral assemblage and the minerals intrinsic dissolution rates control the dissolution rates of the entire system. Analysis of the divalent metal cation proportions indicates that Ca^{2+} is the dominant cation produced during the dissolution of the Faroe Islands rocks. The data also suggests that the reactive surface area characterized by BET exceed the area estimated by simple geometric considerations by more than three orders of magnitude (up to 1789 times larger).

The dissolution of flow tops and flow cores has been investigated by Schaef and Mcgrail (2009) within the Columbia River Basalt Group (CRBG). Schaef and Mcgrail (2009) found flow tops to undergo the fastest dissolution of the two flow architectures. This finding is in contrast to this study, where the cores were found to be to have greater solubilities than the tops. Schaef and Mcgrail (2009) showed there to be a greater quantity of volcanic glass within the flow tops of the CRBG. Differences in the dissolution rates of volcanic glass and crystalline rock have been investigated by Gudbrandsson et al. (2011). Gudbrandsson et al. (2011) noted comparative glass showed significantly faster dissolution rates than crystalline basalt. Therefore, the presence of the volcanic glass within the flow top of the CRBG sample aid faster dissolution rates. Volcanic glass within the lava flow samples of the Faroe Islands is limited and no significant difference was observed between the flow tops and cores. Furthermore, this study found there to be a disproportionate spread of zeolites between the flow tops and cores, with the tops expressing significantly more. As presented earlier zeolites show slower dissolution rates compared to other relevant minerals. This study therefore suggests the higher proportion of zeolites within flow tops negatively impact total rock solubility, leading to decreased dissolution rates. The lack of glass within the flow tops combined with the proportion of zeolites explain the slower dissolution rates compared with Schaef and Mcgrail (2009). However, this study focused on rocks from the Faroe Islands, that although are similar to offshore settings, are thought to

contain significantly more zeolites. Thus, the dissolution trends of flow architectures are likely to show trends similar to Schaef and Mcgrail (2009).

This study provides new insights into the solubility of volcaniclastic beds. Results found the solubility of the inter-lava bed to be slower than the lava flow material. The volcaniclastic bed contains a significant proportion of volcanic glass, which would be expected to show elevated dissolution rates. However, the inter-lava bed sample expresses a significant proportion of zeolite material, suppressing the dissolution rate. Furthermore, the volcanic glass show large quantities of plagonitization, indicative of significant fluid alteration which this study suggests covers the reactive surface of the reactive grains limiting their solubility.

The experiments conducted for this study provided new insights into the dissolution rates of the Faroe Islands rocks, which can be compared to previous research (Figure 56; Schaef and Mcgrail, 2009; Gudbrandsson *et al.*, 2011). The dissolution rates presented by this study are within the range of rates found within previous studies (Schaef and Mcgrail, 2009; Gudbrandsson *et al.*, 2011), with differences down to varying mineralogy. The Icelandic rocks contain olivine, which dissolves significantly faster than other common basaltic minerals (Figure 4; Barnes and O'Niel, 1969; Seifritz, 1990; Kelemen and Manning, 2015; Fanning *et al.*, 2017; Kelemen *et al.*, 2018), whereas the high Ti-flows of the Faroe Islands are devoid of olivine, explaining the slower bulk dissolution rate for the Faroe Islands rocks. The CRBG are also devoid of olivine and also show slower dissolution rates to the Icelandic rock. However, the CRBG samples show solubilities lower than the Faroe Islands despite similar mineralogies, and thus the discrepancies are not immediately apparent. Though, the plagioclase within the CRBG samples appears to contain a significant pure andesine component. Solubilities of andesine were not found; however, looking at the solubilities of plagioclase with differing An contents, Na-rich plagioclase appear to have lower solubilities than more Ca-rich varieties at this studies conditions, causing some influence on the rates, although not enough to explain the difference (Gudbrandsson *et al.*, 2014). Schaef and Mcgrail (2009) used a significantly larger fraction size (0.42-2 mm) within the experiments that may further explain the results presented.

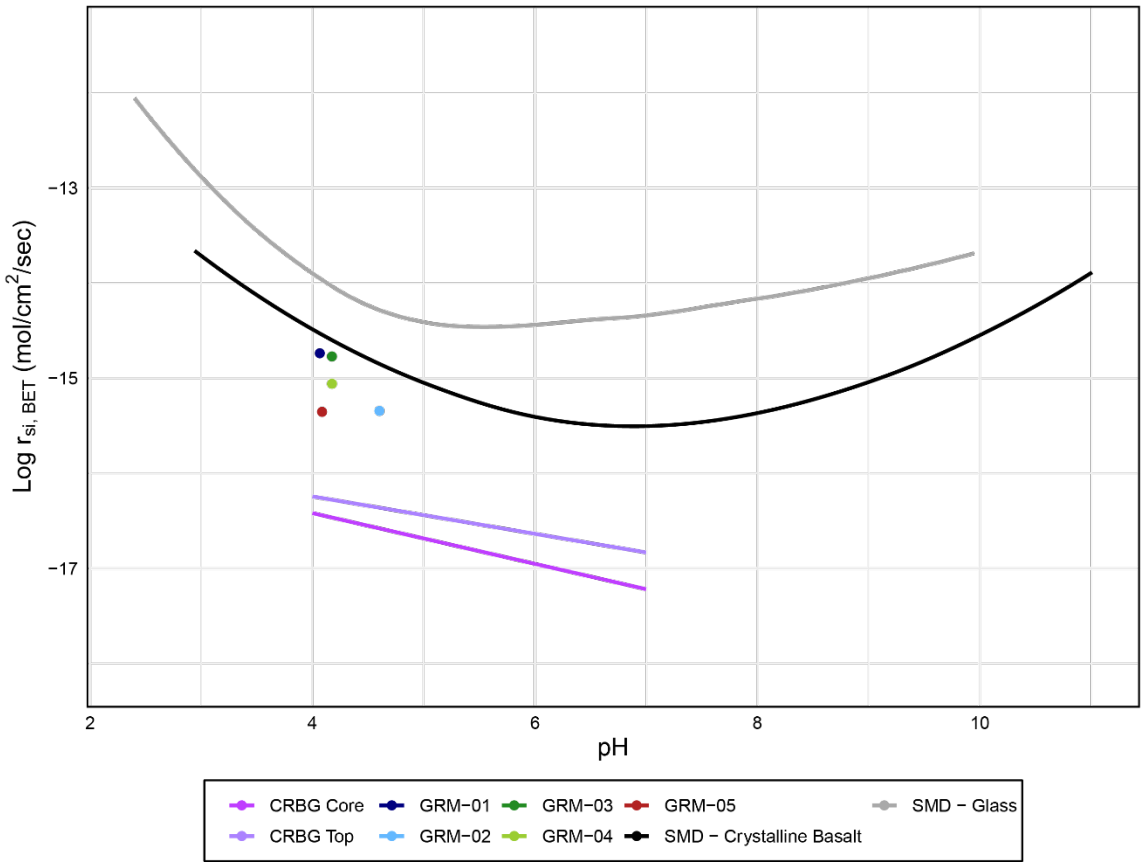

Figure 56 ***Comparison between the steady-state dissolution rates.*** *The bulk rock cation concentrations relative to Si for the Faroe Islands rocks, the Icelandic basalt, and CRBG samples show that the Icelandic basalt has significantly more Mg. The data shows a pH dependency on Si release with was not investigated specifically for this study but can be assumed that this pH dependence would also be present within these rocks.*

The release of divalent metal cations (Ca^{2+}, Mg^{2+}, and Fe^{2+}) is important to consider as they are integral to forming carbonates (Matter, Takahashi and Goldberg, 2007; Kelemen *et al.*, 2011; Kelemen and Hirth, 2012). Gudbrandsson *et al.* (2011) provided an insight into the dissolution of an abundant olivine basalt. While Gudbrandsson *et al.* (2011) showed the preferential release of Mg and Fe but the retention of Ca, this study found the opposite. Olivine is high in Mg and Fe, but poor in Ca and has significantly faster dissolution than other common basaltic minerals, and therefore considerably influences the overall dissolution rate, with Mg and Fe as a larger proportion of the cations releasedThis study showed that the Faroese dissolution samples were olivine devoid, and thus the Mg and Fe were locked in pyroxene and iron oxides. This may also be observed in Figure 57 where Mg is significantly higher than both the Faroe Islands and CRBG rocks and likely the result of olivine. Ca was predominately contained within plagioclase labradorite, Ca-rich but Mg and Fe devoid. Labradorite follows the dissolution rate of olivine, albeit by nearly an order of magnitude, and thus the dissolution of the Faroese rocks is dominated by plagioclase labradorite, providing significant quantities of Ca

compared to Mg and Fe. This is similar to observations from the CRBG samples, and thus it is predicted that the dissolution of these samples would support a calcite dominated system compared to the magnesite predicted by Gudbrandsson *et al.* (2011).

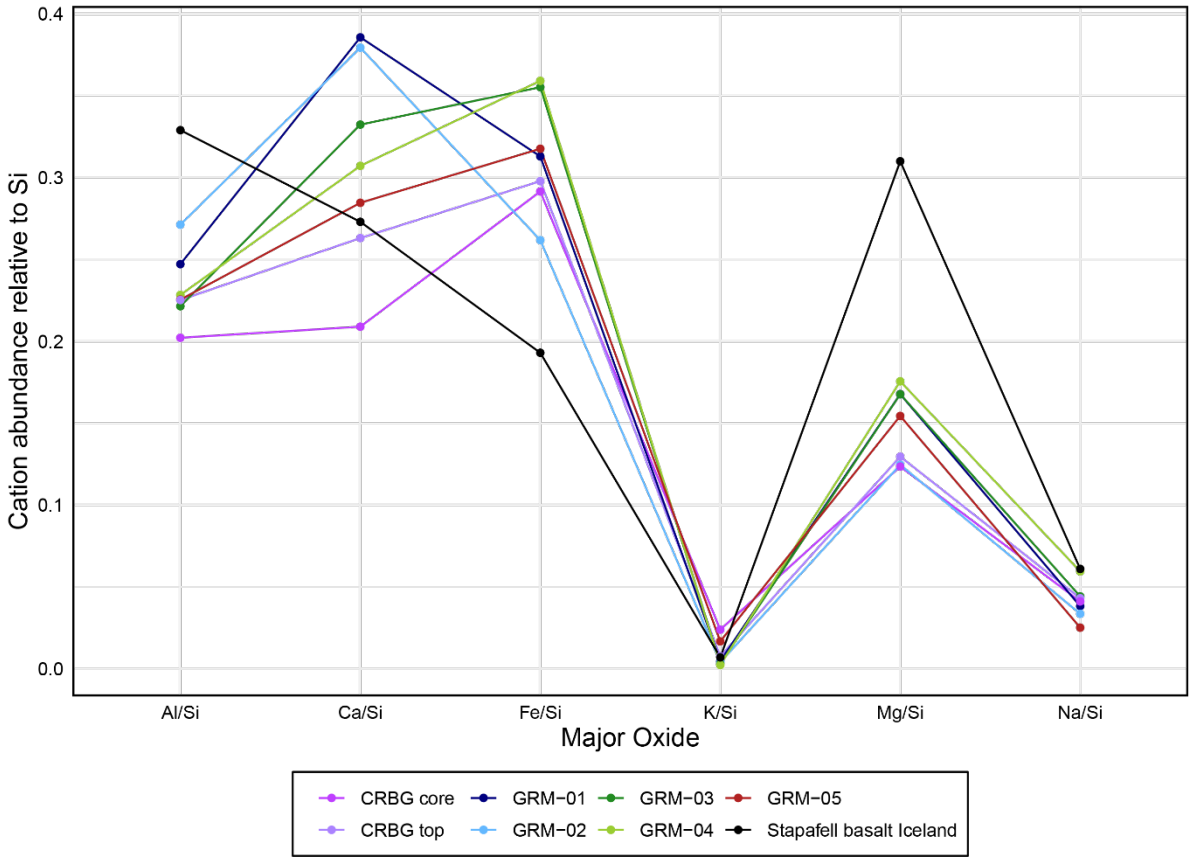

Figure 57 ***Cation concentrations relative to Si within the Faroes samples, CRBG, and the SMD.***

The release rate of divalent metal cations would control the type of carbonate mineral precipitation during CO_2 storage. Data from this study found the concentration of Ca^{2+} released in each sample to show an inverse relationship to the dissolution rates. It is also worth noting that the core of flow 10 contains the highest Ca^{2+} but shows the lowest release rate for this element and the lowest quantity of secondary mineralization of the sample set. The samples' differences further indicate a positive correlation between the amount of secondary mineralization and the Ca^{2+} release rates. Thus, as zeolites overwhelmingly dominate the secondary mineralogy, it is likely that the high Ca^{2+} release rates compared to the other divalent metal cations is derived from these zeolites, which can be of Ca-rich throughout the Faroe Islands such as, chabazite, mesolite, scolecite, Stilbite heulandite, and laumonite (Jørgensen, 2020). As zeolites are microporous and have very high surface areas, they dominate the samples' surface area and likely provide the extreme differences that can be observed between the flow tops and cores. Although zeolites show slow dissolution rates, their rates are inversely linked to their extreme surface areas, and thus they show slow dissolution rates for their sizable surface areas.

Consequently, the proportion of cation release rates relative to their surface area is low, but their surface areas are so large that the zeolites still provide significant cation contributions. These results indicate that calcite precipitation would be favoured over magnesite and siderite under these conditions for these rock samples.

Flow tops have experienced more fluid flow than cores and thus show more alteration, as can be seen by the divalent metal cation release rates. Schaef and Mcgrail (2009) found that flow tops show reduced Fe release rates compared with corresponding flow cores, which is likely a consequence of the low solubility of Fe^{3+} within the alteration products of the flow top. This study agrees with findings from Schaef and Mcgrail (2009) with flow tops showing 2.3 and 141 times lower Fe release than the corresponding cores and also indicates that the alteration within the top of flow 8 is less extensive than flow 10. These results indicate the available Fe within the flow tops is dominated by Fe^{3+} and thus not available for the reaction with bicarbonate to form carbonates. Moreover, the inter-lava bed shows the slowest Fe release rate of the samples, suggesting Fe^{3+} is dominant in the multivalent Fe in this sample. However, the Fe component of the rocks from the Faroe Islands is low compared to Ca^{2+} and Mg^{2+} and thus the oxidation of Fe to Fe^{3+} will have limited influence on carbonate formation.

Literature for the dissolution minerals, crystalline rocks, and basaltic glass show a variety of dissolution rates determined using both geometric and BET specific surface areas. Previous studies (Schaef and Mcgrail, 2009; Gudbrandsson *et al.*, 2011) have shown a dramatic difference between the calculated geometric surface area and BET surface area measurements, by the surface roughness factor. This study found similar differences between the two surface area measurements. The significance is noted within the dissolution rates of the samples. Dissolution rates calculated using geometric surface areas are approximately two orders of magnitude faster than BET counterparts. Thus, the findings suggest that the dissolution rates derived from geometric means are not accurate representations. Even though BET surface area may not be a perfect analogy for actual surface area, measuring the surface roughness of a sample provides a significantly more representative surface area, and thus dissolution rate. Furthermore, learnings from this study indicate that the surface areas may be significantly different from comparatively similar rocks. These differences may be a result of highly microporous minerals such as zeolites and the ability for differing minerals to be crushed, causing a preferential bias for one mineral being a particular size. This is of concern as smaller grains have a larger surface area to volume ratios, and are preferentially dissolved. Thus, it is not appropriate to use geometric derived calculations to compare two separate dissolution rates as this will provide inaccurate interpretations.

In addition to issues associated with surface area before experiments take place, grain surface areas may also change once experiments begin. This change in the surface area has been alluded to by various studies (Schaef and Mcgrail, 2009; Gudbrandsson *et al.*, 2011) through the rounding of grains. This study found similar features; however, due to the nature of this study, investigating the rates of different samples, irregularities between the samples for the final sizes of the grains was observed. This is believed to influence the solubility of the grains, which likely change during the experiments due to smaller grains expressing larger surface areas to volume ratios allowing faster dissolution rates. Furthermore, the top of flow 10 displayed a large size range between the grains, including a greater angularity. Therefore it is interpreted that the smaller size of these samples results from the grains breaking up during the experiment, again affecting the surface areas of individual samples. This study highlights that BET dissolution rates indicate a materials' dissolution rate, but changes during the experiment from either the smoothing of grains or the breaking up of the material will alter their surface area, changing the actual dissolution rate of the substance. Measuring the surface areas of the reacted grains may further provide insights into this and could be the more appropriate surface area to use in calculating the dissolution rate.

The results support existing evidence that basaltic rocks provide good sources of divalent metal cations for potential carbonate precipitation (Gudbrandsson *et al.*, 2011, 2014; Matter *et al.*, 2016; Kelektsoglou, 2018; Kelemen *et al.*, 2019; Pogge von Strandmann *et al.*, 2019). However, this study also stresses the potentially important role of the inter-lava beds within flood basalt sequences because they are both reactive and highly porous. The dissolution data indicate that the inter-lava beds dissolve relatively slowly in the experiments compared with most other samples investigated in this study. However, due to a considerably higher reactive surface area in uncrushed samples, it is suggested that the inter-lava beds would have a significantly higher overall dissolution rate per volume in natural settings. This interpretation stems from inter-lava beds comprising grains and clasts, compared to the surface area of intra-lava units, which is represented by fractures and vesicles with significantly less surface area for fluid-rock interactions.

In this study, only the dissolution rates of high-Ti lava flows were investigated, indicated from the absence of olivine and TiO_2 values >1.5 wt% from the flow cores. Flow 10 shows TiO_2 values much closer to the Low-Ti group than flow 8 and likely explains why two groups were observed within the REE plots (Figure 39), a feature also noted in Millett *et al.* (2017) between these two groups. Flow 10's more depleted LREE signature is a possible consequence of it being derived from a larger melt fraction, indicating a more complex theory behind the two magma reservoir model and suggesting possible magma mixing which may support findings in Millett *et al.* (2017).

As Low-Ti flows occur higher in stratigraphy, it could be expected that offshore reservoirs contain a greater abundance of low-Ti flows. As low-Ti flows contain olivine, their solubility is expected to be greater than the tested High-Ti rocks. Moreover, only the Argir beds' dissolution rate were determined; this bed is a fluvial deposit instead of the more common fallout tuffs seen separating most of the lava flows. Though they are observed to be similar in terms of mineralogy and alteration, and likely share similar solubilities, it would be interesting to test the solubilities of both a low-Ti lava flow and a red bed.

5.6 Reservoir model and greater implications

The results and learnings from this study can be applied to an offshore reservoir as the Faroe Islands acts as an analogue. As previously mentioned, the offshore FIBG is higher stratigraphic level than the Faroe Islands, providing less extensive burial metamorphism and significantly more pore space and a greater frequency of low-Ti lava flows, both of which support reactive reservoir properties. The findings from this study have been applied to a schematic model (Figure 58) to summarize the findings.

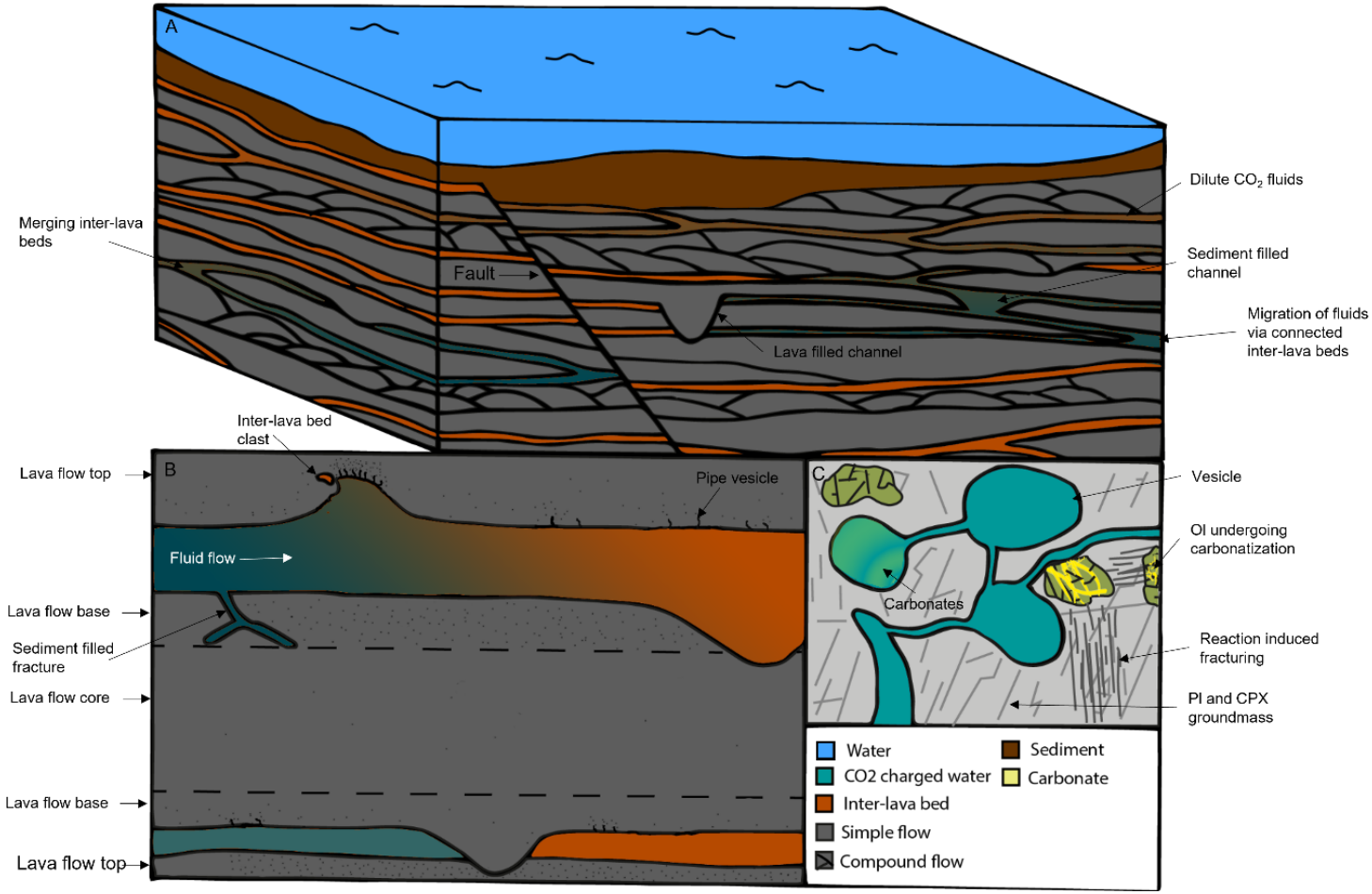

Figure 58 ***Schematic of potential offshore site****. A) An overview schematic showing a series of simple and compound flows split by inter-lave beds. The inter-lava beds show the spread of a CO_2 enriched fluid spreading through connected inter-lava beds, mostly from the thinning of simple lava flows and sediment-filled channels to a lesser extent. However, the fluids are stopped by a large normal fault juxtaposing porous inter-lava beds against impermeable lava flow cores. There are also lava-filled channels stopping the migration of fluids. At the top of the lava pile, sediment can be seen capping any fluid that has made its way to the surface. B) The image shows a close up of simple lava flows and inter-lava beds. The flow tops appear vesicle rich, whereas the vesiculation within flow bases is more localized. Lava flow bases show the addition of pipe vesicle structures, increasing in concentration with vesiculation above domes in the inter-lava bed. These inter-lava beds are the main fluid migration pathways, though fluids migrate into the flow tops and bases, further contributing divalent metal cations and capacities. C) A zoomed-in section of a flow base shows microfractures linking vesicles. Fluids migrating from the inter-lava beds move slowly through the connected vesicles. Over time these carbonates begin to precipitate and clog the system covering the reactive surfaces. Fluids may alter the surrounding groundmass and begin causing carbonatization to minerals such as olivine, leading to reaction induced fracturing.*

Observations from the Faroe Islands have shown that the main fluid pathways are represented by the inter-lava beds. These beds are also expected to provide a significant proportion of the necessary divalent metal cations required for mineral trapping due to their elevated surface areas. In contrast, the flow tops and bases will likely act as subsidiary fluid pathways that are expected to be become blocked without porosity enhancement mechanisms. However, they are interpreted as significant areas for additional capacity within the reservoir and a source of additional divalent metal cations. Domes observed within the inter-lava beds would support greater opportunities for fluids to migrate into the lava flows via their flow bases, thus further enhancing the fluids' ability to migrate away from the main fluid pathways (inter-lava beds). This migration is also supported by the network of micro-fractures linking vesicles, which, although they would represent slow flow rates, increase the amount of reactive surface area within the reservoir, especially over long time scales and will also be the case for flow tops. These micro-fractures also provide more opportunity for CO_2 enriched fluids to reach reactive grains, such as olivine, which would undergo carbonatization and possibly lead to reaction included fracturing, further enhancing and maintaining the reactive surface area. The observed cores of simple lava flows that dominate the upper portions of the stratigraphy will likely be important for the communication between successive lays. These simple flows show limited lateral extents and thus only slow the vertical migration of the fluids. This is essential for the overall capacity of the reservoir, which is composed of relatively laterally extensive but vertically limited inter-lava and intra-lava units. Lava-filled channels predominately form the compartmentalization of the reservoir units, however, the addition of faulting will likely play a significant role with surveys needed to understand their sealing properties.

The reactive nature, high porosities and permeabilities, and communication with successive layers of inter-lava beds are key units in a reactive reservoir. As offshore reservoirs within the FIBG are believed to contain less secondary mineralization, meaning fewer zeolites, Ca release rates are expected to be comparable to the core of flow 1. With the addition of olivine, Mg would be elevated and support a more magnesite dominated precipitation. In a natural system, the dissolution rates of the inter-lava beds are expected to be faster than the crystalline basalt flows due to their higher natural surface areas. Furthermore, the tight nature of the flow cores and limited fracturing would slow the fluids vertical migration but still allow for communication of successive porous units from the thinning out of simple flows. The inter-lava beds would likely hold a significant proportion of the fluids, and with the connectivity of these beds observed on the Faroe Islands being so great, the fluids would spread, supporting a reservoir comprising a network of layers linked by the thining of simple lava flow. This leakage would likely be minimal due to the fast formation of carbonates, even in CO_2 enriched seawater (McGrail *et al.*, 2006; Kelemen *et al.*, 2011; Voigt *et al.*, 2021).

The expected greater solubilities of the offshore FIBG, combined with the far more extensive porosity and permeabilities seen on the Faroe Islands, it is assumed that the potential offshore reservoirs would hold the required reactive reservoir characteristics for carbonate mineralization, these being capacity, communication, compartmentalization, and reactive mineralogy. It is important to note that the conclusions from this study are only expectations based on findings from this study and previous literature that could aid the understandings of potential reactive reservoirs in offshore areas. The offshore FIBG more closely ties to the Faroe Islands, especially with their solubilities, than other areas within the NAIP, such as the VPM. These represent a different suite of rocks that share similarities to the onshore FIBG and may also take learnings from this study to help understand their internal facies relationships and potential solubilities.

Conclusions

Carbon capture and storage is an essential tool in combatting the escalating threat of climate change. Mineral trapping within reactive rocks allows for the secure sequestration of CO_2 for geological time, making it an alluring field of study. This study aimed to generate vital insights into the reservoir potential and rock reactivities from the onshore Faroe Islands Basalt Group (FIBG), which is believed to be analogous with offshore settings, including the more extensive North Atlantic Igneous Province. Based on field observations, petrological, petrophysical, and laboratory analysis, it is speculated that offshore reservoirs within the FIBG contain the required properties of a reactive reservoir for the sequestration of CO_2. The results from the Faroe Islands indicate that reservoir communication from the thinning of simple lava flows is the dominant form of communication between porous units. The inter-lava beds, in particular the common red beds, are thought to be the main fluid pathways in an injection scenario. Lava flow tops and bases present additional capacities; however, as they are expected to have lower permeabilities than inter-lava beds and show a greater tendency to clog due to their channel like networks these are not major fluid pathways. Furthermore, observations from the Faroe Islands showed the presence of domes within the inter-lava beds. These domes show increased vesiculation and pipe vesicle structures, which are thought to have acted as conduits for upward fluid migration into overlying flow bases, and could be of importance for the migration of fluids away from main fluid pathways. The study found micro-fractures linking areas of porosity (vesicles), aiding the effective porosities of the lava flow tops and bases. If present in offshore settings, these micro-fractures are thought to be significant for the slow movement of fluids over a reservoir's evolution. Dissolution rates from high-Ti lava flows showed solubilities comparable to samples from Iceland and the Columbia River Basalt Group, USA, both of which have shown successful mineral trapping of CO_2 (McGrail *et al.*, 2011; Kelektsoglou, 2018). However, offshore settings are expected to contain a greater abundance of low-Ti flows, and thus olivine. This study therefore recommends utilizing offshore FIBG sites for future CO_2 injection.

Recommendations for future work

- The CT scans showed the micro-fracture networks; however, alteration and secondary mineralization were present in places away from these networks, particularly within the flow core sample. It is therefore suggested that a new CT scan is taken away from the fracture networks and adjacent to an area of alteration to understand the ability for fluids to flow through the groundmass of the sample. This is particularly apparent in the CT scan of the core and could have significance for the migration of CO_2 bearing fluids into the reactive rock during the reservoir evolution.
- Low-Ti flows, which contain olivine, increase in presence higher up the stratigraphy. Therefore the theorized elevated solubilities of the low-Ti flows would support more favourable reactive reservoirs offshore. Thus it is suggested that the testing of these Low-Ti flows should be a priority to confirm the theorized potential of these flows.
- The presence of plagioclase groups and low and high Ti flows are thought to individually represent distinct magma batches (Dahren *et al.*, 2015; Millett *et al.*, 2017) however, it has not be investigated whether the plagioclase compositions conform to the low and high-Ti groups and thus represent the same theory behind the magma reservoirs. This knowledge would have significance for better understanding the available divalent metal cation distributions within flow packages and thus aid the ability to pick reservoir opportunities.

References

Agisoft Metashape version 1.5 (2019) 'Agisoft Metashape User Manual', *Agisoft Metashape*, (September), p. 160. Available at: https://www.agisoft.com/pdf/metashape-pro_1_5_en.pdf.

Appelo, C. A. J. and Postma, D. (1993) 'Geochemistry, groundwater and pollution', *Geochemistry, groundwater and pollution*. doi: 10.1016/0016-7037(94)90585-1.

Arganda-Carreras, I. *et al.* (2017) 'Trainable Weka Segmentation: A machine learning tool for microscopy pixel classification', *Bioinformatics*, 33(15), pp. 2424–2426. doi: 10.1093/bioinformatics/btx180.

Buckley, Simon John *et al.* (2019) 'LIME : Software for 3-D visualization , interpretation , and communication of virtual geoscience models', *Geosphere,* 15(1), pp. 222-235. doi: 10.1130/GES02002.1.

Brunauer, S. etal. (1938) 'Adsorption of gases in multimolcular layers', Journal of the American Chemical Society, 60(2), pp. 309-319. DOI: 10.1021/ja01269a023.

Bryan, S. E. and Ernst, R. E. (2008) 'Revised definition of Large Igneous Provinces (LIPs)', *Earth-Science Reviews,* 86, pp. 175–202. doi: 10.1016/j.earscirev.2007.08.008.

Callow, B. *et al.* (2018) 'Assessing the carbon sequestration potential of basalt using X-ray micro-CT and rock mechanics', *International Journal of Greenhouse Gas Control*. Elsevier, 70(February), pp. 146–156. doi: 10.1016/j.ijggc.2017.12.008.

Chalmers, J. A. and Waagstein, R. (2006) 'Scientific results from the deepened Lopra-1 borehole, Faroe Islands', *Geological Survey of Denmark and Greenland Bulletin*, 9(2006), pp.1-156.

Chen, Y. and Brantley, S. L. (1998) 'Diopside and anthophyllite dissolution at 25° and 90°C and acid pH', *Chemical Geology.* Elsevier, 147 (1998), pp. 233-248. doi: 0.1016/S0009-2541(98)00016-3.

Collins, T. J. (2007) 'ImageJ for microscopy', *BioTechniques*, 43(1S), pp. S25–S30. doi: 10.2144/000112517.

Couves, R. C. (2015) 'Investigating the Petrophysical Properties of Volcanic Reservoir Analogues through the use of Micro-Focus X-ray Computed Tomography'. PhD thesis. University of Southampton.

Dahren, B. et al. (2015) 'Plagioclase mineral chemistry in the Faroe Islands Basalt Group', Faroe Islands Exploration Conference: Proceedings of the 4th Conference, Annales Societatis Scientiarum, Færoensis, Supplementum LXIV, (February 2016), pp. 39–51.

Dai, Z. et al. (2017) 'CO2 Sequestration and Enhanced Oil Recovery at Depleted Oil/Gas Reservoirs', *Energy Procedia*. 114(November 2016), pp. 6957–6967. doi: 10.1016/j.egypro.2017.08.034.

Edwards, R. W. J. and Celia, M. A. (2018) 'Infrastructure to enable deployment of carbon capture, utilization, and storage in the United States', *Proceedings of the National Academy of Sciences of the United States of America*, 115(38), pp. E8815–E8824. doi: 10.1073/pnas.1806504115.

Eldholm, O., Thiede, J. and Taylor, E. (1989) 'Evolution of the Voring volcanic margin', Proc., scientific results, ODP, Leg 104, Norwegian Sea, 5 (25), pp. 1033–1065. doi: 10.2973/odp.proc.sr.104.191.1989.

Ellis, D. et al. (2002) 'The stratigraphy, environment of eruption and age of the Faroes Lava Group, NE Atlantic Ocean', Geological Society, London Special Publication, 197, pp. 253–269. doi: 10.1144/GSL.SP.2002.197.01.10.

Gilfillan, S. M. V. et al. (2009) 'Solubility trapping in formation water as dominant CO2 sink in natural gas fields', *Nature*. Nature Publishing Group, 458(7238), pp. 614–618. doi: 10.1038/nature07852.

Gislason, S. R. and Oelkers, E. H. (2014) 'Carbon storage in basalt', *Science*, 344(6182), pp. 373–374. doi: 10.1126/science.1250828.

Glover, E. T., Faanu, A. and Fianko, J. R. (2010) 'Dissolution Kinetics of Stilbite at Various Temperatures under Alkaline Conditions'. *West African Journal of Applied Ecology*, 16(1). doi: 10.4314/wajae.v16i1.55871

Google Earth Pro, (2008) *Faroe Islands*. [Online] Available at: http://www.earth.google.com/web/ [Accessed 22 March 2021].

Goldberg, D. S., Takahashi, T. and Slagle, A. L. (2008) 'Carbon dioxide sequestration in deep-sea basalt', *Proceedings of the National Academy of Sciences of the United States of America*, 105(29), pp. 9920–9925. doi: 10.1073/pnas.0804397105.

Goldberg, D. and Slagle, A. L. (2009) 'A global assessment of deep-sea basalt sites for carbon sequestration', *Energy Procedia*. Elsevier, 1(1), pp. 3675–3682. doi: 10.1016/j.egypro.2009.02.165.

Gudbrandsson, S. et al. (2011) 'An experimental study of crystalline basalt dissolution from 2pH11 and temperatures from 5 to 75°C', *Geochimica et Cosmochimica Acta*. Elsevier Ltd, 75(19), pp. 5496–5509. doi: 10.1016/j.gca.2011.06.035.

Gudbrandsson, S. et al. (2014) 'Experimental determination of plagioclase dissolution rates as a function of its composition and pH at 22°C', *Geochimica et Cosmochimica Acta*. Elsevier Ltd, 139, pp. 154–172. doi: 10.1016/j.gca.2014.04.028.

Gudbrandsson, S. (2014) 'Experimental weathering rates of aluminium-silicate', PhD thesis. Géosciences Environnement Toulouse, Université Paul Sabatier.

Gysi, A. P. and Stefánsson, A. (2012) 'Experiments and geochemical modeling of CO 2 sequestration during hydrothermal basalt alteration', *Chemical Geology.* Elsevier B.V., 306–307, pp. 10–28. doi: 10.1016/j.chemgeo.2012.02.016.

Hansen, J. and Jerram, D. Mccaffrey, K. Passey, S. (2011) 'Early Cenozoic saucer-shaped sills of the Faroe Islands : an example of intrusive styles in basaltic lava piles', Journal of the Geological Society, 168(1), pp. 159–178. doi: 10.1144/0016-76492010-012.

Hansen, L. D. et al. (2005) 'Carbonated serpentinite (listwanite) at Atlin, British Columbia: A geological analogue to carbon dioxide sequestration', *Canadian Mineralogist*, 43(1), pp. 225–239. doi: 10.2113/gscanmin.43.1.225.

Harkin, C. et al. (2020) 'Origin, composition and relative timing of seaward dipping reflectors on the Pelotas rifted margin', *Marine and Petroleum Geology*. Elsevier, 114(2020), p. 104235. doi: 10.1016/j.marpetgeo.2020.104235.

Hövelmann, J. (2012) 'Carbonation reactions in ultramafic rocks: Experimental insights into physicochemical processes, microtexture evolution and reaction mechanisms', PhD thesis. University of Oslo.

Jamtveit, B., Malthe-Sørenssen, A. and Kostenko, O. (2007) 'Reaction enhanced permeability during retrogressive metamorphism', *Earth and Planetary Science Letters*, 267(3–4), pp. 620–627. doi: 10.1016/j.epsl.2007.12.016.

Japsen, P. et al. (2004) 'Seismic and petrophysical properties of Faroe Islands basalts: The SeiFaBa project', *Geological Survey of Denmark and Greenland Bulletin*, 65(4), pp. 53–56. doi: 10.34194/geusb.v4.4784.

Jerram, D. A. et al. (2009) 'Understanding the offshore flood basalt sequence using onshore volcanic facies analogues: An example from the Faroe-Shetland basin', *Geological Magazine*, 146(3), pp. 353–367. doi: 10.1017/S0016756809005974.

Jørgen, H. et al. (2019) 'Emplacement mechanisms of a dyke swarm across the brittle-ductile transition and the geodynamic implications for magma-rich margins', *Earth and Planetary Science Letters*. Elsevier B.V., 518, pp. 223–235. doi: 10.1016/j.epsl.2019.04.016.

Jørgensen, O. (2020) 'The regional distribution of zeolites in the basalts of the Faroe Islands and the significance of zeolites as palaeo- temperature indicators', *GEUS Bulletin*, 44(2020), pp. 123–156. dio: 10.34194/geusb.v44.5342.

Kelektsoglou, K. (2018) 'Carbon capture and storage: A review of mineral storage of CO2 in Greece', *Sustainability* (Switzerland), 10(12). doi: 10.3390/su10124400.

Kelemen, P. et al. (2019) 'An Overview of the Status and Challenges of CO2 Storage in Minerals and Geological Formations', *Frontiers in Climate*, 1(9), pp. 1–20. doi: 10.3389/fclim.2019.00009.

Kelemen, P. B. et al. (2011) ' Rates and Mechanisms of Mineral Carbonation in Peridotite: Natural Processes and Recipes for Enhanced, in situ CO 2 Capture and Storage ', *Annual Review of Earth and Planetary Sciences*, 39(1), pp. 545–576. doi: 10.1146/annurev-earth-092010-152509.

Kelemen, P. B. et al. (2018) 'In situ carbon mineralization in ultramafic rocks: Natural processes and possible engineered methods', *Energy Procedia*. Elsevier B.V., 146, pp. 92–102. doi: 10.1016/j.egypro.2018.07.013.

Kelemen, P. B. and Hirth, G. (2012) 'Reaction-driven cracking during retrograde metamorphism: Olivine hydration and carbonation', *Earth and Planetary Science Letters*. Elsevier, 345–348, pp. 81–89. doi: 10.1016/j.epsl.2012.06.018.

Kelemen, P. B. and Manning, C. E. (2015) 'Reevaluating carbon fluxes in subduction zones, what goes down, mostly comes up', *Proceedings of the National Academy of Sciences of the United States of America*, 112(30), pp. E3997–E4006. doi: 10.1073/pnas.1507889112.

Kelemen, P. B. and Matter, J. (2008) 'In situ carbonation of peridotite for CO2 storage', *Proceedings of the National Academy of Sciences of the United States of America*, 105(45), pp. 17295–17300. doi: 10.1073/pnas.0805794105.

Lacinska, A. M. et al. (2017) 'An experimental study of the carbonation of serpentinite and partially serpentinised peridotites', *Frontiers in Earth Science*, 5(37). doi: 10.3389/feart.2017.00037.

Lormand, C. et al. (2018) 'Weka trainable segmentation plugin in ImageJ: A semi-automatic tool applied to crystal size distributions of microlites in volcanic rocks', *Microscopy and Microanalysis*, 24(6), pp. 667–675. doi: 10.1017/S1431927618015428.

Martin, B. and Fyfe, W. S. (1970) 'Some experimental and theoretical observations on the kinetics of hydration reactions with particular reference to serpentinization', *Chemical Geology*, 6(C), pp. 185–202. doi: 10.1016/0009-2541(70)90018-5.

Mathisen, M. E. and McPherson, J. G. (1991) 'Volcaniclastic deposits: implications for hydrocarbon exploration', *Sedimentation in volcanic settings*, 45, pp. 27–36. doi: 10.2110/pec.91.45.0027.

Matter, J. M. et al. (2016) 'Rapid carbon mineralization for permanent disposal of anthropogenic carbon dioxide emissions', *Science*, 352(6291), pp. 10–13. dio: 10.1126/science.aad8132.

Matter, J. M., Takahashi, T. and Goldberg, D. (2007) 'Experimental evaluation of in situ CO2-water-rock reactions during CO2 injection in basaltic rocks: Implications for geological CO2 sequestration', *Geochemistry, Geophysics*, Geosystems, 8(2). doi: 10.1029/2006GC001427.

McGrail, B. P. et al. (2006) 'Potential for carbon dioxide sequestration in flood basalts', *Journal of Geophysical Research: Solid Earth*, 111(12), pp. 1–13. doi: 10.1029/2005JB004169.

McGrail, B. P. et al. (2011) 'The Wallula basalt sequestration pilot project', *Energy Procedia.* Elsevier, 4, pp. 5653–5660. doi: 10.1016/j.egypro.2011.02.557.

Millett, J. M. et al. (2017) 'Geochemical stratigraphy and correlation within large igneous provinces: The final preserved stages of the Faroe Islands Basalt Group', *Lithos*. Elsevier B.V., 286–287, pp. 1–15. doi: 10.1016/j.lithos.2017.05.011.

Oelkers, E. and Schott, J. (2000) 'An experimental study of enstatite dissolution rates as a function of pH, temperature, and aqueous Mg and Si concentration, and the mechanism of pyroxene/pyroxenoid dissolution', *Geochimica et Cosmochimica*, 65(8), pp. 1219–1231.

Ólavsdóttir, J., Andersen, M. S. and Boldreel, L. O. (2015) 'Reservoir quality of intrabasalt volcaniclastic units onshore Faroe Islands, North Atlantic igneous province, Northeast Atlantic', *AAPG Bulletin*, 99(3), pp. 467–497. doi: 10.1306/08061412084.

Ólavsdóttir, J., Eidesgaard, Ó. R. and Stoker, M. S. (2017) 'The stratigraphy and structure of the Faroese continental margin', *Geological Society Special Publication*, 447(1), pp. 339–356. doi: 10.1144/SP447.4.

Passey, S. R. and Bell, B. R. (2007) 'Morphologies and emplacement mechanisms of the lava flows of the Faroe Islands Basalt Group, Faroe Islands, NE Atlantic Ocean', *Bulletin of Volcanology*, 70(2), pp. 139–156. doi: 10.1007/s00445-007-0125-6.

Passey, S. R. and Jolley, D. W. (2009) A revised lithostratigraphic nomenclature for the Palaeogene Faroe Islands Basalt Group, NE Atlantic Ocean, *Earth and Environmental Science Transactions of the Royal Society of Edinburgh*. doi: 10.1017/S1755691009008044.

Petersen, U. K. (2014) 'PhD thesis Propagation and scattering of reflection seismic waves in a basalt succession' . PhD thesis. University of Stavanger and University of Faoe Islands.

Pettus, H. D., Pettus, H. D. and Virginia, W. (2021) 'Independent , Semi-Automated Classification of Petrographic Features in Volcanic Rocks Using FiJi and Weka Rocks Using FiJi and Weka'. Masters Thesis. West Virginia University.

Planke, S. (1994) 'Geophysical response of flood basalts from analysis of wire line logs: Ocean Drilling Program Site 642, Voring volcanic margin', *Journal of Geophysical Research*, 99(B5), pp. 9279–9296. doi: 10.1029/94JB00496.

Planke, S., Berndt, C., and Alvarez Zarikian, C.A., 2021. *Expedition 396 Scientific Prospectus: Mid-Norwegian Conti- nental Margin Magmatism*. International Ocean Discovery Program. https://doi.org/10.14379/iodp.sp.396.2021.

Plümper, O. et al. (2012) 'The interface-scale mechanism of reaction-induced fracturing during serpentinization', *Geology*, 40(12), pp. 1103–1106. doi: 10.1130/G33390.1.

Pogge von Strandmann, P. A. E. et al. (2019) 'Rapid CO 2 mineralisation into calcite at the CarbFix storage site quantified using calcium isotopes', *Nature Communications*, 10(1), pp. 1–7. doi: 10.1038/s41467-019-10003-8.

Pokorný, R., Krmíček, L. and Árting, U. E. (2015) 'The first evidence of trace fossils and pseudo-fossils in the continental interlava volcaniclastic sediments on the Faroe Islands', *Bulletin of the Geological Society of Denmark*, 63(1968), pp. 45–57. doi: 10.37570/bgsd-2015-63-05.

Pokrovsky, O. and Schott, J. (2000) 'Kinetics and mechanism of forsterite dissolution at 25°C and pH from 1 to 12', *Geochimica et Cosmochimica*, 64(19), pp. 3313–3325.

R Core Team (2020). R: A Language and Environment for Statistical Computing'. Vienna, Austria: R Foundation for Statistical Computing. Available at: https://www.r-project.org/.

Ragnars, K. V. (1993) 'Dissolution kinetics of heulandite at pH 2-12 and 25 ° C', *Geochrmica et Cosmochimrca Acta*, 57(11), pp. 2439–2449. doi: 10.1016/0016-7037(93)90408-O.

Randolph, J. B. and Saar, M. O. (2011) 'Combining geothermal energy capture with geologic carbon dioxide sequestration', *Geophysical Research Letters,* 38(10), pp. 1–7. doi: 10.1029/2011GL047265.

Rasmussen, J. (1968) 'Petrology of a 3,000 metre sequence of basaltic lavas in the Faroe Islands', *Lithos*, 1(3), pp. 286-304. doi: 10.1016/S0024-4937(68)80045-3.

Rasmussen, J. and Noe-Nygaard, A. (1970) 'Geology of the Faroe Islands (Pre-Quarternary)', *Danmarks Geologiske Undersøgelse I. Række*, 25, pp. 1–142. doi: 10.34194/raekke1.v25.6780.

Real, P. G. and Vishal, V. (2016) 'Mineral Carbonation in Ultramafic and Basaltic Rocks', in Real, P. G. and Vishal, V. (eds.) *Geologic Carbon Sequestration: Understanding Reservoir Behavior*, pp. 1–338.

RStudio Team (2020). RStudio: Integrated Development Environment for R. RStudio, PBC, Boston, MA URL. Available at: http://www.rstudio.com/.

Rudge, J. F., Kelemen, P. B. and Spiegelman, M. (2010) 'A simple model of reaction-induced cracking applied to serpentinization and carbonation of peridotite', *Earth and Planetary Science Letters*. Elsevier B.V., 291(1–4), pp. 215–227. doi: 10.1016/j.epsl.2010.01.016.

Røyne, A. et al. (2011) 'Crack propagation driven by crystal growth', *Epl*, 96(2). doi: 10.1209/0295-5075/96/24003.

Saxov, S. & Abrahamsen, N. (1964). A Note on some gravity and density measurings in the Faroe Islands. *Bollettino di Geofisica Teorica ed Applicata*, VI, 249–262.

Schaef, H. T. and Mcgrail, B. P. (2009) 'Applied Geochemistry Dissolution of Columbia River Basalt under mildly acidic conditions as a function of temperature : Experimental results relevant to the geological sequestration of carbon dioxide', *Applied Geochemistry*. Elsevier Ltd, 24(5), pp. 980–987. doi: 10.1016/j.apgeochem.2009.02.025.

Seifritz, W. (1990) 'CO2 disposal by means of silicates', *Nature*, 345, pp. 486. doi: 10.1038/345486b0.

Snæbjörnsdóttir, S. et al. (2017) 'The chemistry and saturation states of subsurface fluids during the in situ mineralisation of CO2 and H2S at the CarbFix site in SW-Iceland', *International Journal of Greenhouse Gas Control*. Elsevier Ltd, 58, pp. 87–102. doi: 10.1016/j.ijggc.2017.01.007.

Stockmann, G. J. et al. (2011) 'Do carbonate precipitates affect dissolution kinetics? 1: Basaltic glass', *Chemical Geology*. Elsevier, 284(3–4), pp. 306–316. doi: 10.1016/j.chemgeo.2011.03.010.

Sun, S. and Mcdonough, W. F. (1989) 'Chemical and isotopic systematics of oceanic basalts : implications for mantle composition and processes', (42), pp. 313–345. doi: 10.1144/GSL.SP.1989.042.01.19.

Tomsich, C. S. et al. (2015) 'Ultramafic and Mafic Rock Distributions in Central Alaska and Implications for CO2 Sequestration', *Natural Resources Research*. Springer US, 24(3), pp. 349–368. doi: 10.1007/s11053-014-9259-3.

US EPA. (2021). Inventory of U.S. Greenhouse Gas Emissions and Sinks | US EPA. [online] Available at: https://www.epa.gov/ghgemissions/inventory-us-greenhouse-gas-emissions-and-sinks (Accessed 19 August 2021).

Ussiri, D. A. N. and Lal, R. (2017) Carbon Sequestration for Climate Change Mitigation and Adaptation, Carbon Sequestration for Climate Change Mitigation and Adaptation. doi: 10.1007/978-3-319-53845-7.

Vilarrasa, V., Makhnenko, R. Y. and Laloui, L. (2017) 'Potential for Fault Reactivation Due to CO2 Injection in a Semi-Closed Saline Aquifer', Energy Procedia, 114(2017), pp. 3282–3290. doi: 10.1016/j.egypro.2017.03.1460.

Voigt, M. et al. (2021) 'An experimental study of basalt–seawater–CO2 interaction at 130 °C', *Geochimica et Cosmochimica Acta*, 308(2021), pp. 21–41. doi: 10.1016/j.gca.2021.05.056.

Vosgerau, H. *et al.* (2011) *Palaeogene volcaniclastic sedimentary units interbedded with basalt lava flows - a 3-D photogeological study of cliff sections from the Faroe Islands*.

Vosgerau, H. et al. (2016) 'Reservoir architectures of interlava systems: A 3D photogrammetrical study of Eocene cliff sections, Faroe Islands', *Geological Society Special Publication*, 436(1), pp. 55–73. doi: 10.1144/SP436.7.

Waagstein, R. (1988) 'Structure, composition and age of the Faeroe basalt plateau', *Geological Society Special Publication*, 39(39), pp. 225–238. doi: 10.1144/GSL.SP.1988.039.01.21.

Wang, P. et al. (2015) 'Characteristics of volcanic reservoirs and distribution rules of effective reservoirs in the Changling fault depression, Songliao Basin', *Natural Gas Industry B*. Elsevier Ltd, 2(2015), pp. 440–448. doi: 10.1016/j.ngib.2015.09.020.

Westoby, M. J. et al. (2012) 'Geomorphology " Structure-from-Motion " photogrammetry : A low-cost , effective tool for geoscience applications', *Geomorphology*. Elsevier B.V., 179, pp. 300–314. doi: 10.1016/j.geomorph.2012.08.021.

Wigley, T. M. L., Jones, P. D. and Kelly, P. M. (2019) 'Global warming of 1.5°C?', *Nature*, 291(5813), p. 285. doi: 10.1038/291285a0.

Williams, R. G., Katavouta, A. and Goodwin, P. (2019) 'Carbon-Cycle Feedbacks Operating in the Climate System', *Current Climate Change Reports*, 5(4), pp. 282–295. doi: 10.1007/s40641-019-00144-9.

Xiao, Y., Xu, T. and Pruess, K. (2009) 'The effects of gas-fluid-rock interactions on CO2 injection and storage: Insights from reactive transport modeling', *Energy Procedia*. Elsevier, 1(1), pp. 1783–1790. doi: 10.1016/j.egypro.2009.01.233.

Appendices

Appendix A – Sample list

Table A. 1 Sample list. *A list of all the samples collected by this study from a combination of fieldwork and cores.*

Sample	Description	Analysis	Formation	Location
GM-05	Flow directly above Argir beds	Thin section	Enni	Glyvursnes-1
GM-06	Sediment showing varying colouration	Thin section	Enni	Glyvursnes-1
GM-08	Sample that spans a mineralized dark fracture like patterns.	Thin section	Enni	Glyvursnes-1
GM-09	Visual colour change which appears to represent a fracture like network.	Thin section	Enni	Glyvursnes-1
GM-10	A coherent sample of plagioclase phyric basalt	Thin section	Enni	Glyvursnes-1
GM-11	Dark alteration lines in a light aphyric flow	Thin section	Enni	Glyvursnes-1
GM-12	Natural core split of basalt furthest from sediment	Thin section	Enni	Glyvursnes-1
GM-13	Natural core split of basalt	Thin section	Enni	Glyvursnes-1
GM-14	Basalt closest to sediment	Thin section	Enni	Glyvursnes-1
GM-15	Sediment	Thin section	Enni	Glyvursnes-1
GM-16	Sediment	Thin section	Enni	Glyvursnes-1
GM-17	Flow base to act as calibration to fluid flow	Thin section	Enni	Glyvursnes-1
GM-18	Distinct yellow coloured mineral filling vesicles.	Thin section	Enni	Glyvursnes-1
GM-19*	Asymmetry to host beside a fracture	Polished section	Enni	Glyvursnes-1
GM-20*	Asymmetry to host beside a fracture	Polished section	Enni	Glyvursnes-1
GM-21	Distinct alteration halos adjacent to mineralized fractures	CT	Enni	Glyvursnes-1
GM-22 A-B	Mineralized fractures in flow	CT	Enni	Glyvursnes-1
GM-23	Volcaniclastic sediment	Thin section	Enni/Malinstindur	Glyvursnes-1
GM-24	Green coloured secondary mineralization	Thin section	Malinstindur	Glyvursnes-1
GM-25	Many thin mineralized fractures in the basalt	CT	Malinstindur	Glyvursnes-1
GM-26	Blue-green coloured alteration mineral	Thin section	Malinstindur	Glyvursnes-1
GM-27	White mineralization, including an alteration halo	Polished section	Malinstindur	Glyvursnes-1
T2M-01	Sediment sample 5-10 cm of upper Enni fm	Thin section	Enni	Tjørnunes_2
T2M-02	Flow with lots of secondary mineralisation	Thin section	Enni	Tjørnunes_2
T2M-03	Flow top with infingering of sediment	CT	Enni	Tjørnunes_2
T2M-04	Aphyric flow core	CT	Enni	Tjørnunes_2
T2M-05	Aphyric flow core	Thin section	Enni	Tjørnunes_2
T2M-06	A large section of connecting mineralized fractures	Thin section and CT	Enni	Tjørnunes_2
T2M-07	Lots of crossing mineralized fractures	Thin section and CT	Enni	Tjørnunes_2
T2M-08	Alteration halo adjacent to mineralized fracture	CT	Enni	Tjørnunes_2
T2M-09	Alteratation halo adjacent to mineralized fracture	Thin section	Enni	Tjørnunes_2
GNM-01	Interesting alteration pattern	Thin section	Enni	Grønadalsnøva_1
GNM-02	Interesting alteration pattern	Polished section	Enni	Grønadalsnøva_1
GNM-03	alteration halo adjacent to natural fracture	CT and thin section	Enni	Grønadalsnøva_1

GRM-01	Tabular plagioclase physic basalt/flow core (Flow 10)	Reactivity, thin section, XRF	Enni	Glyvursnes
GRM-02	Tabular plagioclase physic basalt/flow top (Flow 10)	Reactivity, thin section, XRF	Enni	Glyvursnes
GRM-03	Aphyric basalt/flow core (Flow 8)	Reactivity, thin section, XRF, inc. GRM-06 blind	Enni	Glyvursnes
GRM-04	Aphyric basalt/flow top (Flow 8)	Reactivity, thin section, XRF	Enni	Glyvursnes
GRM-05	Sediment/sample taken 1 m below the top	Reactivity, thin section, XRF	Enni	Glyvursnes
F20-14	Volcanic rock sampled directly above a thick volcaniclastic bed	CT, thin section	Malinstindur	Nolsoy
F20-11	Volcanic rock adjacent to long pipes	CT, thin section	Malinstindur	Eidi
F20-10	Flow top showing extensive alteration	CT, thin section	Malinstindur	Eidi Quarry
F20-09	Flow core showing some banding of vesicles	Thin section	Malinstindur	Eidi Quarry

Appendix B – Supplementary geochemical data

Table B. 1 Raw XRF data for major elements.

Report Number:
A21-05248
Report Date:
20/4/2021

Analyte Symbol	SiO2	Al2O3	Fe2O3(T)	MnO	MgO	CaO	Na2O	K2O	TiO2	P2O5	LOI	Total
Unit Symbol	%	%	%	%	%	%	%	%	%	%	%	%
Detection Limit	0.01	0.01	0.01	0.001	0.01	0.01	0.01	0.01	0.001	0.01		0.01
Analysis Method	FUS-ICP	FUS-ICP	FUS-ICP	FUS-ICP	FUS-ICP	FUS-ICP	FUS-ICP	FUS-ICP	FUS-ICP	FUS-ICP	GRAV	FUS-ICP
GRM-01	47.53	15.26	12.938	0.188	6.18	11.99	2.29	0.25	1.737	0.15	1.28	99.77
GRM-02	44.21	15.58	10.062	0.142	4.27	10.97	1.87	0.2	1.332	0.1	11.56	100.3
GRM-03	47.38	13.63	14.639	0.199	6.16	10.33	2.64	0.16	2.403	0.23	2.66	100.3
GRM-04	46.29	13.73	14.451	0.191	6.3	9.33	3.47	0.12	2.393	0.23	4.08	100.6
GRM-05	47.77	13.97	13.174	0.184	5.71	8.88	1.51	0.9	2.415	0.17	5.73	100.3
GRM-06	48.25	13.45	14.885	0.205	6.16	10.31	2.68	0.15	2.431	0.23	2.11	100.8

Table B. 2 Raw trace element data from XRF analysis

Report Date: 20/4/2021

Analyte Symbol	Sc	Be	V	Cr	Co	Ni	Cu	Zn	Ga	Ge	As	Rb	Sr	Y	Zr	Nb	Mo	Ag	In	Sn	Sb	Cs
Detection Limit	1	1	5	20	1	20	10	30	1	0.5	5	1	2	0.5	1	0.2	2	0.5	0.1	1	0.2	0.1
GRM-01	40	< 1	341	210	41	70	200	80	19	1.3	< 5	2	188	24.5	110	6.1	< 2	< 0.5	0.1	1	< 0.2	< 0.1
GRM-02	31	< 1	241	170	36	70	160	70	22	1	< 5	4	258	20.3	72	4.1	< 2	< 0.5	< 0.1	1	0.2	< 0.1
GRM-03	37	< 1	389	140	46	80	220	100	19	1.3	< 5	1	215	27.8	135	9.2	< 2	0.5	0.1	1	< 0.2	0.1
GRM-04	36	< 1	416	150	48	90	210	100	18	1	< 5	1	178	27.1	130	9.2	< 2	0.5	0.1	1	< 0.2	0.1
GRM-05	34	< 1	258	150	46	70	310	90	20	1.7	< 5	11	146	29.4	141	9.6	< 2	0.5	0.1	1	0.2	< 0.1

Analyte Symbol	Ba	La	Ce	Pr	Nd	Sm	Eu	Gd	Tb	Dy	Ho	Er	Tm	Yb	Lu	Hf	Ta	W	Tl	Pb	Bi	Th	U
Detection Limit	2	0.05	0.05	0.01	0.05	0.01	0.005	0.01	0.01	0.01	0.01	0.01	0.005	0.01	0.002	0.1	0.01	0.5	0.05	5	0.1	0.05	0.01
GRM-01	49	6.27	16.5	2.44	12.4	3.57	1.36	4.02	0.73	4.67	0.96	2.68	0.36	2.32	0.376	2.7	0.41	< 0.5	< 0.05	< 5	< 0.1	0.46	0.15
GRM-02	19	5.23	13.3	2.02	9.62	2.86	1.11	3.31	0.58	3.65	0.74	2.04	0.289	1.78	0.285	1.9	0.3	< 0.5	< 0.05	< 5	< 0.1	0.36	0.09
GRM-03	54	10.5	26.9	3.98	18.8	5.02	1.69	5.24	0.87	5.2	1	2.76	0.378	2.33	0.337	3.3	0.68	2.5	< 0.05	< 5	< 0.1	0.77	0.25
GRM-04	37	10.9	27.9	4.02	19	5.19	1.83	5.15	0.89	5.34	1.03	2.68	0.37	2.3	0.349	3.4	0.68	< 0.5	< 0.05	< 5	< 0.1	0.79	0.24
GRM-05	529	11.6	29.4	4.26	20.7	5.64	1.92	5.57	0.93	5.48	1.07	2.98	0.406	2.44	0.352	3.8	0.7	< 0.5	0.08	< 5	< 0.1	0.82	0.28

Appendix C – Blank data from the solubility analysis

Table C. 1 Blanks taken directly from the DI water and the inlet solution. Blanks 1-3 represent the inlet solution in the bucket which fed samples GRM-1 to GRM-03 and Blanks 4-5 are from the inlet solution in the bucket feeding GRM-04 and GRM-05.

Date and time	**Blanks**	SiO2 (ppm)	**Na (ppm)**	**K (ppm)**	**Ca (ppm)**	**Mg (ppm)**	**Fe (ppm)**	**Al (ppm)**	**B (ppm)**	**S (ppm)**
26/05/2021	Blank 1	0.21	0.08	0.00	0.00	0.00	0.00	0.00	0.01	0.02
26/05/2021	Blank 2	0.22	0.09	0.00	0.00	0.00	0.00	0.00	0.01	0.03
26/05/2021	Blank 3	0.22	0.11	0.04	0.01	0.00	0.00	0.00	0.02	0.06
26/05/2021	Blank 4	0.21	0.09	0.01	0.00	0.00	0.00	0.00	0.01	0.02
26/05/2021	Blank 5	0.21	0.08	0.01	0.01	0.00	0.00	0.00	0.01	0.03
08/06/2021	DI	0.235	0.023	0.002	0.012	0.000	0.000	0.000	0.000	0.000
14/06/2021	Blank 1-3	0.242	0.004	0.000	0.002	0.000	0.000	0.000	0.000	0.000
14/06/2021	Blank 3-5	0.238	0.001	0.000	0.002	0.000	0.000	0.000	0.000	0.000
16/06/2021	BLANK 1-3	0.226	0.015	0.000	0.003	0.000	0.000	0.000	0.000	0.000
16/06/2021	BLANK 4-5	0.220	0.010	0.000	0.002	0.000	0.000	0.000	0.000	0.000
18/06/2021	BLANK 1-3	0.24	0.00	0.00	0.001	0.000	0.000	0.001	0.00	0.00
20/06/2021	BLANK 1-3	0.24	0.01	0.00	0.000	0.000	0.000	0.000	0.00	0.00
22/06/2021	BLANK 1-3	0.23	0.01	0.00	0.000	0.000	0.000	0.001	0.00	0.00
18/06/2021	BLANK 4-5	0.25	0.01	0.00	0.000	0.000	0.000	0.001	0.00	0.00
20/06/2021	BLANK 4-5	0.25	0.01	0.00	0.000	0.000	0.000	0.000	0.00	0.00
22/06/2021	BLANK 4-5	0.22	0.01	0.00	0.000	0.000	0.000	0.001	0.00	0.00
23/06/2021	BLANK 1-3	0.218	0.003	0.000	< 0.001	< 0.001	< 0.001	< 0.001	< 0.05	0.06
23/06/2021	BLANK 4-5	0.225	0.009	0.000	< 0.001	< 0.001	< 0.001	< 0.001	< 0.05	0.06


UNIVERSITAS OSLOENSIS
MDCCCXI